OPEN ACCESS
IOP Publishing | Songshan Lake Materials Laboratory
MATERIALS FUTURES
Mater. Futures **3** (2024) 042102 (36pp)
https://doi.org/10.1088/2752-5724/ad7872

Topical Review

Technological achievements in the fabrication of tubular-designed protonic ceramic electrochemical cells

Maria A Gordeeva[1,2], **Artem P Tarutin**[1,2], **Nikolai A Danilov**[1,2] and **Dmitry A Medvedev**[1,2,*]

[1] Laboratory of Electrochemical Devices Based on Solid Oxide Proton Electrolytes, Institute of High-Temperature Electrochemistry, 620066 Ekaterinburg, Russia
[2] Hydrogen Energy Laboratory, Ural Federal University, 620002 Ekaterinburg, Russia

E-mail: dmitrymedv@mail.ru

Received 11 August 2024, revised 2 September 2024
Accepted for publication 8 September 2024
Published 24 September 2024

Abstract

Protonic ceramic electrochemical cells provide an excellent basis for the advancement of high-temperature solid oxide devices, offering potential solutions to a range of challenges in the hydrogen energy and carbon capture fields. The facilitated ionic transport in proton-conducting electrolytes enables these cells to operate at temperatures 100 °C–500 °C lower than those of conventional solid oxide cells with known zirconia electrolytes. As a result, promising performances have been reported for various types of proton ceramic electrochemical cells. Nevertheless, these advancements have been demonstrated only at the laboratory scale, whereas their ZrO_2-based counterparts have already been commercialized. This review presents an overview of the fundamental and applied aspects related to the fabrication of tubular protonic ceramic electrochemical cells and their subsequent characterization as hydrogen permeation membranes, hydrogen pumps, hydrogen sensors, fuel cells, electrolysis cells, and electrochemical reactors. A specific focus is placed on the technological aspects of the tube preparations derived from the original powder sources as well as the dimensional characteristics of the tubes, which serve as an indicator of scaling. Therefore, this review serves as a starting point for the development and scaling of protonic ceramic electrochemical cells, with the potential for large-scale production.

Keywords: electrochemistry, energy conversion, hydrogen, proton transport, perovskite, solid oxide cells, scaling

---

[*] Author to whom any correspondence should be addressed.

2752-5724/24/042102+36$33.00

Contents

1. Introduction

Proton-conducting oxides have great potential for designing low- and intermediate-temperature electrochemical devices for various purposes, including efficient electricity generation protonic ceramic fuel cells, (PCFCs), pure hydrogen production protonic ceramic electrolysis cells, (PCECs), electrochemical hydrogenation/dehydrogenation conversion protonic ceramic membrane reactors, hydrogen compression, and hydrogen electroanalysis [1–6]. The central component of many of these examples is a proton-conducting electrolyte [7–10], whose ionic conductivity at reduced temperatures exceeds (by up to 1–2 orders of magnitude) those of most conventional oxygen-ionic electrolytes. This allows for rather high performance and energy efficiency at 400 °C–700 °C while maintaining a low degree of degradation in long-term operation focus.

For more than 40 years, many complex oxide systems have been analyzed and characterized in terms of their hydration capability along with ability to display high proton concentration, mobility, and conductivity [1]. However, those belonging to the barium cerate-zirconate family ($BaCeO_3$–$BaZrO_3$ or $Ba(Ce,Zr)O_3$) are widely recognized as the most promising proton-conducting electrolytes for electrochemical applications [7, 9, 11, 12]. This approach relies on an optimized balance between different functional properties of doped $Ba(Ce,Zr)O_3$, which include not only electrical properties but also densification features, thermal and chemical expansion behaviors, mechanical properties, chemical interaction inertness, etc [13, 14]. All these individual properties play crucial roles in the development of high-performance and robust protonic ceramic electrochemical cells.

In addition to the design of novel or modernized electrolyte systems, extensive research has been conducted over the past two decades to identify suitable oxygen and fuel electrodes for PCFC and PCEC applications. During this period, many promising materials have been proposed as efficient electrocatalysts for oxidation, reduction, and evolution reactions (known as ORR, OER, HOR, and HER), with excellent operability over low- and intermediate-temperature ranges. The most recent developments in electrode engineering, including trends, activities, and progress, can be found in several recent review articles [15–20], which disclose intricate relationships between the composition, structure, and electrochemical activity towards electrode processes.

The development of electrochemical cells relies not only on material aspects (chemistry, design, engineering) but also on the corresponding technologies that enable a complex of functional materials to be assembled into working units or single cells. In this regard, the group of main functional materials (electrodes and electrolytes) is extended by construction materials, such as glass sealants, interlayers, interconnects, current collectors, gaskets, and frames [21–24]. These materials should also be optimized to perform their specific functions efficiently at working temperatures. In addition, the fabrication of each functional material requires a thorough solution to technological problems to enable transfer from laboratory-scale single cells to a group of such cells (known as stacks or modules). A literature review revealed that both fundamental and technological issues have been adequately addressed for conventional zirconia-based solid oxide fuel cells (SOFCs), solid oxide electrolysis cells (SOECs), and reversible SOFCs. As a result, the latter are currently stacked up to several kW [25–30] and tested for several tens of thousands of hours [31–37]. However, PCFCs and PCECs have not yet achieved similar results. Specifically, the operation of the latter (in the form of lab-scale cells) is usually limited to 500–3000 h [38–42].

The aforementioned findings prompted our aim to prepare the current review article devoted to the development and fabrication technologies of protonic ceramic electrochemical cells; the main emphasis was on the tubular design of such cells, which has been identified as one of the most promising in terms of weight-dimensional characteristics. Notably, the tubular types of SOFCs and SOECs have been recently reviewed in several articles [43–48]. However, these reviews address conventional oxygen-ionic cells, with a limited focus on protonic ceramic cells. Therefore, the present review aims to address this gap by providing a detailed R&D analysis of tubular-type protonic ceramic electrochemical cells for various applied purposes.

2. Classification of solid oxide electrochemical cells

There are several general classifications of solid oxide cells, which include the type of electrolyte used, the type of supporting materials, and the geometric design.

In consideration of the conducting nature of an electrolyte, two principal classes may be identified: oxygen-ionic and proton-conducting materials. The former class includes stabilized or doped oxide systems based on zirconia (ZrO_2), ceria (CeO_2), bismuth oxide (Bi_2O_3), lanthanum gallate ($LaGaO_3$), and other less studied compositions [49–53]. The notable oxygen-ionic conductivity of these materials is attributed to acceptor doping, which results in the formation of oxygen vacancies. These vacancies can migrate along the crystal lattice, allowing oxygen ions to jump from one anionic position to the vacant position. This movement is an energy-consuming process; as a result, desirable oxygen-ionic conductivity values can be achieved at elevated temperatures, while they rapidly decrease with cooling. In contrast, proton-conducting electrolytes are distinguished by a reduced activation energy for proton transport. This can be attributed to the distinctive characteristics of proton defects, including their lower mass and size than those of oxygen ions. The activation energy of proton transport (mobility, diffusion, conductivity) is often lower, enabling the attainment of acceptable proton conductivity values between 400 and 700 °C. The most well-known examples of proton-conducting electrolytes are cerates and zirconates of alkaline-earth elements (ABO_3, where $A = Ca$, Sr, Ba; $B = Ce$, Zr), which are briefly discussed in the next section. Moreover, proton transport is a characteristic property of some other perovskites [54–57] and perovskite-related oxides [58–60]. In addition to oxygen-ionic and proton-conducting electrolytes, hybrid ionic (or dual ionic) systems are also known [61–63]. It is postulated that the simultaneous transport of oxygen ions and protons in hybrid systems offers advantageous functions in terms of PCFC and PCEC efficiency: in fuel cell mode, water molecules are formed at both the anode and cathode spaces, facilitating proton transport of the electrolyte; in electrolysis mode, water vapor is decomposed to a greater extent at both electrode spaces, enhancing the electrolysis efficiency.

The classification of supporting materials encompasses three principal categories: electrolyte-, electrode-, and metal-supported configurations of electrochemical cells. Historically, the first SOFC modules were based on supported zirconia electrolytes [64, 65], which were considered the most technologically straightforward option at the time. However, there has been a subsequent shift in focus towards electrode-supporting designs for SOFCs and SOECs, with the aim of enhancing their performance. Such an improvement is achieved by reducing the thickness of the electrolyte and, consequently, the associated ohmic resistance components. Nevertheless, if the ohmic resistance does not affect the performance of electrochemical cells (for example, potentiometric sensors), the electrolyte configuration can be used in terms of simplicity and cost-effectiveness. In the case of other electrochemical cell types, a Ni-cermet-supported configuration is the most frequently employed configuration in both laboratory and commercial contexts [66–68]. Metal-supported solid oxide electrochemical cells have recently garnered increasing attention from technologicals [69–73]. More precisely, the replacement of ceramic (or cermet) supporting electrodes for metal supports has the potential to address several issues associated with insufficient mechanical strength, low redox stability, and poor thermal shock resistance of ceramic materials. The aforementioned properties of metals are of superior quality accompanied by relatively low production costs at the same time.

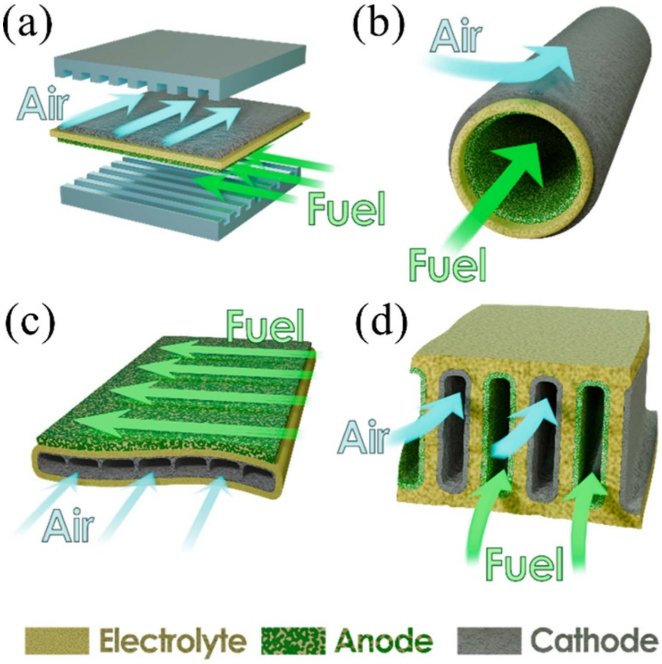

Figure 1. Simplified schemes of SOFC and SOEC designs: (a) planar, (b) tubular, (c) flat-tube, and (d) monolithic.

By discussing the last (geometric-related) classification, multilayered electrochemical cells can be separated into four well-known configurations, as shown in figure 1.

It is widely acknowledged that the planar SOFC/SOEC design (figure 1(a)) is the simplest in terms of cell fabrication and assembly into stacks. Furthermore, in comparison with alternative designs, the planar configuration is associated with relatively low costs, high volumetric power density, and the straightforward possibility of increasing the required power by stacking. The following aspects can be identified as the most significant disadvantages: (i) while sealing a single cell is relatively easy at the laboratory scale, achieving a hermetically sealed stack presents significant technical challenges; (ii) the spatial features of planar cells result in an uneven distribution of heat, electrons, and mass transfer fields, necessitating optimization to attain uniform distributions of these fields and to prevent high energy loss and mechanical/thermal instability.

The tubular design (figure 1(b)) represents a rational alternative to planar cells owing to the simplicity of sealing, the higher mechanical strength and the superior mechanical resistance associated with the symmetric circular geometry of the tubes. However, these cells also have several limitations. First, the tubular-type cells exhibit a lower volumetric power density because of less dense packing and larger losses related to long paths of connecting cells in a stack. Second, it is evident that the manufacturing costs of tube fabrication are higher than those of planar cells. Nevertheless, these issues are currently well addressed in both fundamental and applied research.

A flat-tube design (figure 1(c)) is proposed as a means of combining the advantages of both planar and tubular configurations previously mentioned. Although several technological issues have been resolved, the fabrication of such a hybrid design remains quite challenging and expensive. The primary disadvantages of monocytic cells (figure 1(d)) are associated with the electrolyte supports, which contribute to the total cell performance owing to a high ohmic resistance, as well as the difficulty in sealing and organizing current collectors. However, this configuration offers advantages in terms of high volumetric power density and excellent thermomechanical (TM) strength. Additionally, there are other derivatives of this design, including honeycomb-type and cone-tube configurations. More details regarding these types of solid oxide cells can be found elsewhere [74–76].

3. A brief comparative analysis of oxygen-ionic and proton-conducting electrolytes

A Scopus analysis indicates that the topic of tubular SOFCs and SOECs has been the subject of extensive research, with over 1600 papers published up to date. This analysis also indicates that the period between 2007 and 2011 represented a peak in publication activity, with more than 100 papers published annually. The number of publications subsequently decreases to 50–90 papers per year. Upon removing all papers containing the ‘proton’, ‘proton ceramic’, and ‘protonic ceramic’ keywords from all fields, the number of publications decreased to approximately 1400 items. This suggests that ∼200 papers address or provide specific information about protonic ceramic electrochemical cells. As previously stated in the Introduction, tubular SOFCs based primarily on conventional oxygen-ionic electrolytes have been recently reviewed in several publications [43–48]. Consequently, a critical analysis of tubular PCFCs/PCECs is of significant interest.

The distinct differences between the oxygen-ionic and proton-conducting electrolytes must be clarified. These differences can be attributed to the unique ability of proton-conducting oxides to reversibly absorb and desorb water molecules in a process that involves the participation of oxygen vacancies

$$H_2O + V_O^{\bullet\bullet} + O_O^{\times} \rightleftarrows 2OH_O^{\bullet}. \quad (1)$$

The resulting protons affect a number of functional properties of origin phases, including their phase structure and mechanical and transport properties (figure 2).

The phase transition features associated with the hydration of oxide phases might be observed in perovskites exhibiting one or more phase transitions from room temperature to ∼1000 °C. For example, doped $BaCeO_3$ exhibits a series of phase transitions until the formation of a stable cubic perovskite structure at elevated temperatures [76]. At lower temperatures, the formation of monoclinic, orthorhombic, or rhombohedral crystal structures may occur. Notably, more distorted perovskites are formed upon hydration. For example, if the cubic structure of an unhydrated $BaCe_{0.8}Y_{0.2}O_{3-\delta}$ (BCY) compound is formed at 500 °C and above, such a cubic structure is stable only at 650 °C and above for the hydrated BCY phase [77]. Another study [78] indicated that the cubic structure of BCY is stable for a range of 800 °C–1000 °C in dry oxygen. However, when oxygen was humidified with D_2O, a lower-symmetry perovskite (rhombohedral) was observed in the same temperature range.

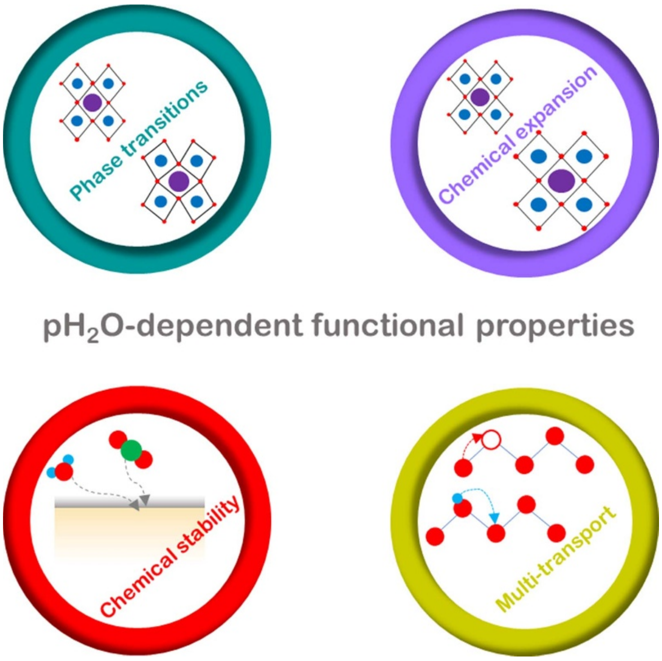

Figure 2. Some functional properties of proton-conducting oxide electrolytes depending on water vapor partial pressure variation.

The dimensional variation of such perovskites can be explained by local structural distortions related to the appearance or interaction of new and already existing defects [79–82]. As shown in equation (1), a parent phase (composed of cations with stable oxidation states) must contain oxygen vacancies to provide protonic transfer. The oxygen vacancies represent unoccupied positions in the anionic sublattice of perovskites. When water molecules interact with these vacancies, the oxygen from water fills the anionic site, forming a regular oxygen-ionic position in the crystal. At the same time, the protons of the water molecules become localized on the oxygen ions. In other words, the oxide crystal accumulates a water substance with a size of ∼2.8 Å; as a result, such a crystal expands and changes its origin structure.

In addition to the crystal structure transformations, the proton-conducting oxides display a pronounced H_2O-induced chemical strain (expansion upon hydration and shrinkage upon dehydration). Chemical expansion effects have been widely discussed for classical ABO_3 perovskites, depending on their composition, basic structure, acceptor dopant contents, and measured conditions [83–90]. These effects, along with conventional thermal expansion, result in a nonlinear temperature-dependent change in dimensional characteristics (e.g. sample length and lattice parameters), representing a significant challenge in the mechanical compatibility of proton-conducting electrolytes with electrode systems.

In detail, the electrode phases can also be hydrated, but their hydration degree is typically less than 10% of the theoretical amount of oxygen vacancies [91, 92]. Therefore, despite potential water uptake, the electrode materials do not exhibit visible chemical expansion effects under actual operating conditions. Chemical expansion issues represent the most significant challenge in the fabrication of PCFC or PCEC stacks with an extended working area. This is because the chemical expansion behavior, as the intrinsic property of proton-conducting electrolytes, cannot be eliminated or even minimized: more conductive electrolytes exhibit more pronounced chemical strain effects during heating/cooling, and vice versa.

Another crucial aspect of proton-conducting materials is their chemical stability. One of the most conductive electrolytes is the Ba-based family, which includes $BaCeO_3$, $BaZrO_3$, and $BaHfO_3$. Despite the formation of proton defects during dissociative water adsorption at elevated temperatures, some compounds have been observed to exhibit instability in the presence of water at lower temperatures. For example, doped $BaCeO_3$ interacts with steam at temperatures below 400 °C [93], whereas the perovskite structure is stable at higher temperatures and gas humidity. The thermodynamic stability of $BaCeO_3$ in the presence of CO_2 is inadequate under all experimental conditions, precluding the electrochemical conversion of C-based compounds [76]. To enhance chemical stability, cerium in $BaCeO_3$ is partially or fully replaced with other stabilized elements to form a mixed $Ba(Ce,M)O_3$ system or another $BaMO_3$ family (where $M = Zr$, Hf, Sn, Th, Ti, Ta, or Nb). These compounds also exhibit proton transport coupled with enhanced chemical stability against possible interactions with gas-phase components [94–96].

While the chemical stability of proton-conducting perovskites has been extensively studied in the context of gas reactants, the chemical interactions between different functional materials of PCFCs and PCECs represent a crucial aspect in achieving robust interface regions that are responsible for both low ohmic and low polarization resistances. Considering the classic ZrO_2 and CeO_2 compounds, it is well known that pure or stabilized zirconia materials have very low chemical stability with respect to many oxygen electrodes based on lanthanum or alkaline earth elements. Specifically, low conductive zirconate phases ($La_2Zr_2O_7$ and $MZrO_3$, where $M = Ca$, Sr, Ba) can be formed even at rational sintering temperatures. To address this issue, highly stable CeO_2 is often introduced as a protective layer between the zirconia electrolyte and the oxygen electrode [24, 97, 98]. A comparable trend is predicted when the chemical stabilities of the $BaCeO_3$ and $BaZrO_3$ compounds are compared: the chemical stability of the former is greater than that of the latter. In addition, Ce-enriched compounds are preferred over Zr-containing analogs. In the case of La-containing electrodes, the PCFC/PCEC interface can be enriched by $La_2Ce_2O_7$ or $La_2Zr_2O_7$ phases, but the ionic conductivity of $La_2Ce_2O_7$ is much greater than that of $La_2Zr_2O_7$ [99]. In the case of Sr-containing electrodes, $SrCeO_3$ and $SrZrO_3$ can also be formed at the interface; again, $SrCeO_3$ has a higher ionic conductivity than $SrZrO_3$ [100].

Achieving the chemical stability of proton-conducting perovskites with Ni-based fuel (hydrogen) cermet electrodes is another important challenge. These Ni-cermets are composed of NiO (or Ni under reducing conditions) and an electrolyte component, which is utilized for the same thin-film electrolyte layer. In principle, two-component cermets are relatively stable even when high sintering temperatures (up to 1500 °C) are used. However, a challenge emerges when a 'Ni-cermet/electrolyte' half-cell is prepared. Under high co-sintering temperatures, Ni ions diffuse from the cermet into the grain boundaries of an electrolyte body (nickel has very low solubility in the cerate or zirconate phases). A low-ionic phase of BaY_2NiO_5 then tends to accumulate at the grain boundaries of Y-doped cerates/zirconates, hindering proton transport and leading to mechanical weakening of the grain contacts [14, 101]. This impurity can be inhibited by replacing the most commonly used dopant (yttrium) with other elements. In detail, no formation of impurity phase(s) is detected for Yb-doped compounds. Although a $BaYb_2NiO_5$ derivative is known to exist [102], its chemical stability appears to be significantly lower than that of BaY_2NiO_5. Consequently, no proton-blocking $BaYb_2NiO_5$ phase is formed when the Ni-based cermets and Yb-doped perovskite electrolytes are co-sintered. As a result, Yb-doped/Yb-containing proton-conducting perovskites belong to mainstream current activities in materials science aspects related to PCFC and PCEC developments [103–107].

Most proton-conducting electrolytes are generally triple-conducting materials capable of simultaneously exhibiting electronic, oxygen-ionic, and protonic conductivities, whose values depend on the temperature, oxygen partial pressure, and water vapor partial pressure [108, 109]. Numerous studies have shown that the p-type electronic conductivity reaches rather high values (and contributes to the total conductivity) under oxidizing conditions, even at reduced temperatures as low as 600 °C. Therefore, the electronic transport of such electrolytes cannot be completely excluded and must be taken into account in the real operating modes of electrochemical cells with unseparated gas spaces (symmetric cells) and separated gas spaces (PCFCs, PCECs). In contrast, some other electrolyte classes, including stabilized zirconia and doped lanthanum gallates, exhibit unipolar oxygen−ionic transport without meaningful biases in electronic transport [110].

These are the main features of proton-conducting materials in comparison with conventional oxygen-ionic electrolytes. Other features related to synthesis, densification, and enhancement of ionic conductivity are specific to each individual system; readers are encouraged to pursue this information independently.

4. Technological aspects of fabricating tubular protonic ceramic cells

This section reviews possible approaches to the fabrication of tubular protonic ceramic electrochemical cells. Since these cells represent a series of ceramic or cermet layers with different compositions, microstructures and functions, two main

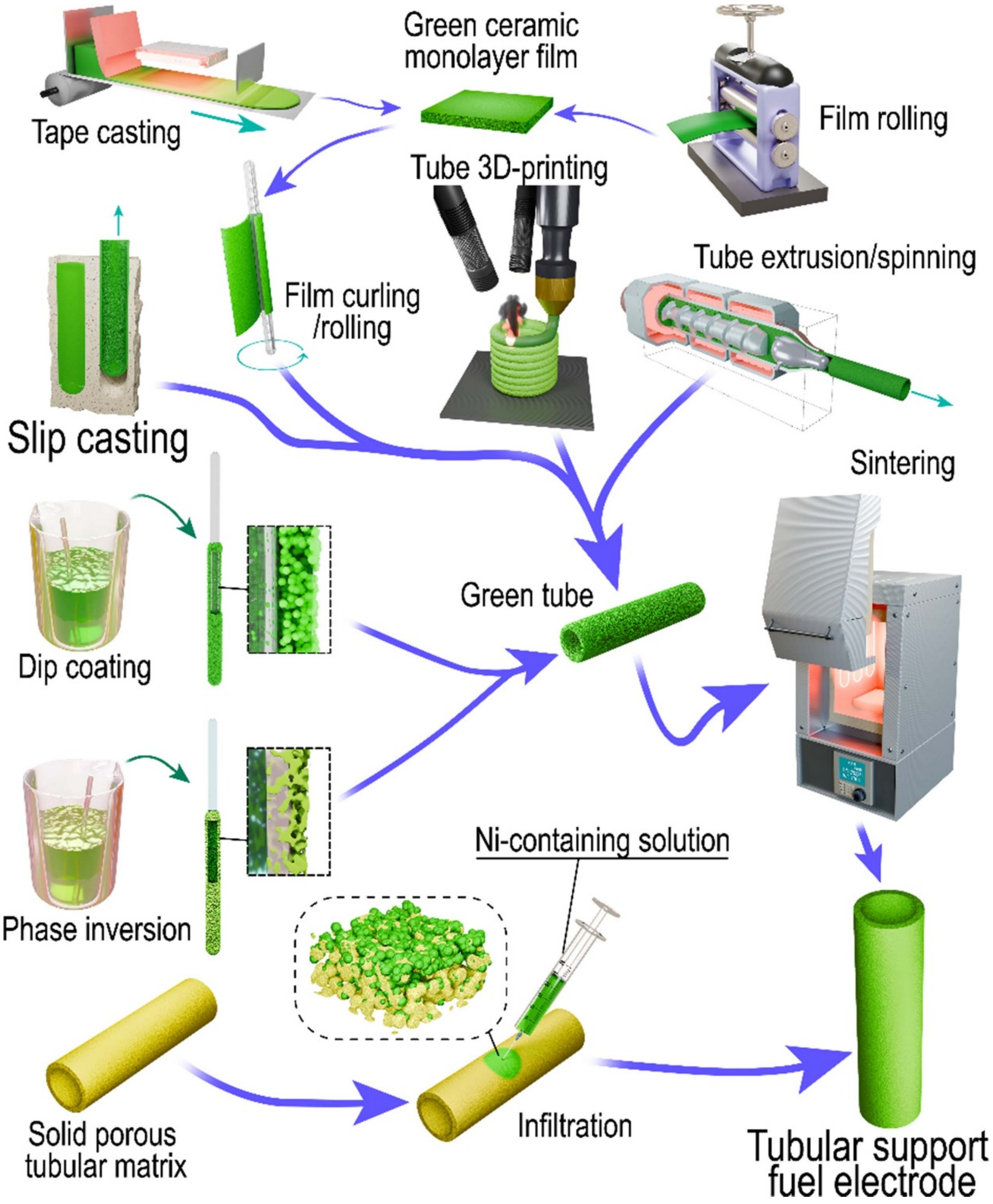

Figure 3. Various approaches to prepare protonic ceramic electrochemical support tubes.

stages can be identified. The first is based on the preparation of the tubular supports (figure 3), whereas the second is based on the further organization of the electrolyte (figure 4) and counter electrode layers. These stages are closely related to each other for each individual report; therefore, they are jointly analyzed below. Notably, the following discussion is presented in a temporal context (spanning the period from ∼2010 to the present) to illustrate the advancements made in the fabrication of tubular protonic ceramic electrochemical cells. Additionally, particular attention has been given to the organic components utilized for substrate preparation.

One of the first studies devoted to the preparation and characterization of a proton ceramic tube was reported by Yoon *et al* in 2009 [111, 112]. The authors used tape-casting to prepare a green tape. More precisely, a mixture of $SrCeO_3$ (SC) prepared via the solid-state synthesis method and NiO was ball milled for 24 h, using an ethanol/toluene solvent and a number of other components: fish oil (dispersant), polyvinyl butyral (PVB), polyethylene glycol (PEG) (binder), and di-n-butyl phthalate (plasticizer). The as-obtained slurry was tape cast. After the green tapes were formed, they were rolled onto a steel core rod and end-closed via a cap of the same material. To form an electrolyte layer, $SrCe_{0.9}Eu_{0.1}O_{3-\delta}$ (SCE) was synthesized via a citrate−nitrate synthesis method. To preserve the membrane integrity related to the different shrinkage behaviors of NiO–SC and SCE during sintering, the green support was partially sintered at 1100 °C–1200 °C, and then, the inner side of the tube was coated with an SCE slurry (its organic composition was not specified). The final co-sintering process was performed between 1350 °C and 1450 °C, which

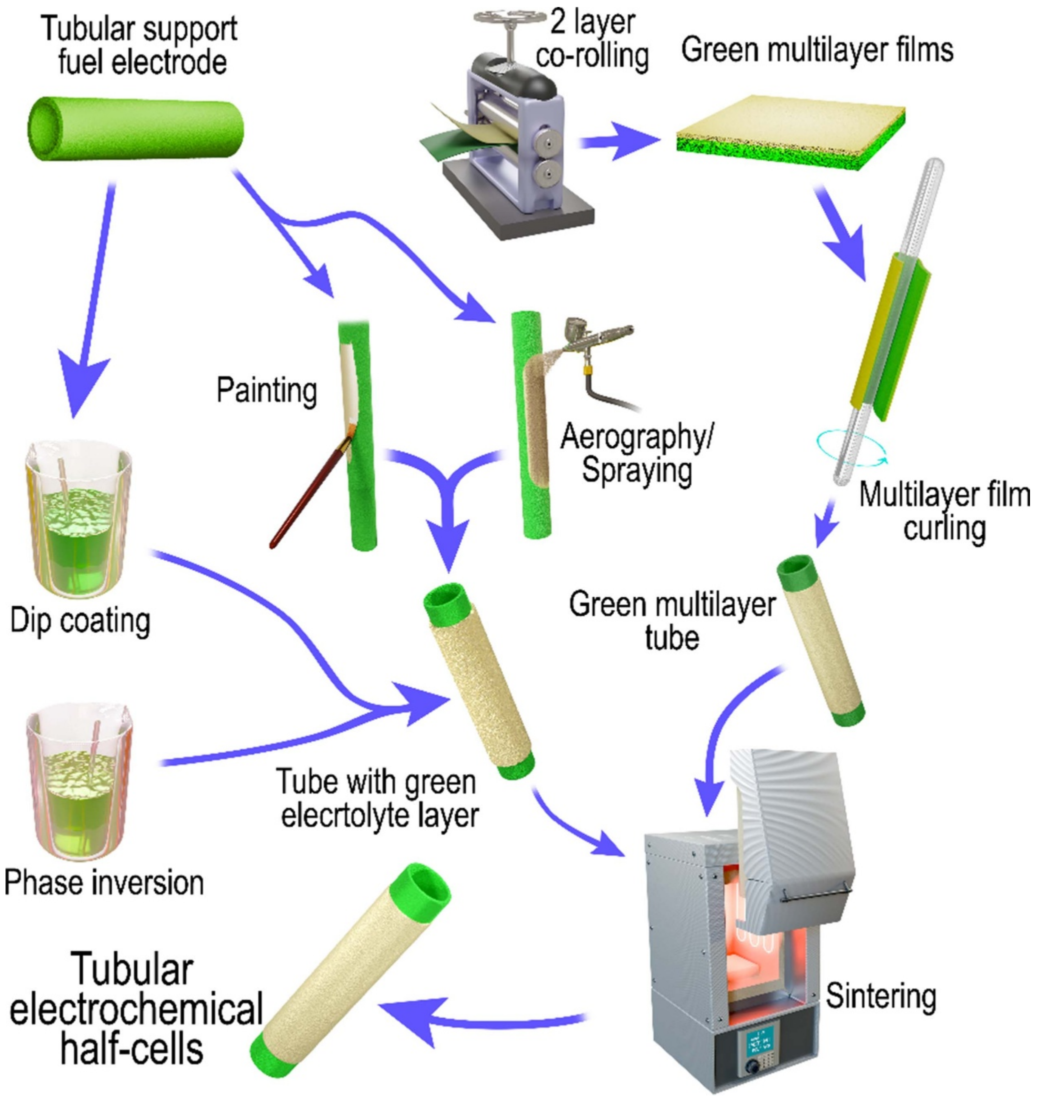

Figure 4. Various approaches to prepare protonic ceramic electrochemical half-cells.

allowed a 30 μm thin layer to form. This bilayer tube was used as a hydrogen permeation membrane. The same approach was also employed to prepare membranes based on other electrolyte types composed of $SrCe_{0.7}Zr_{0.2}Eu_{0.1}O_{3-\delta}$ [113].

While tape casting is a prevalent technique for fabricating anode substrates, it is particularly well suited to the planar configuration of solid oxide electrochemical cells. The application of this method for tubular cells is constrained by the necessity of a rolling stage, which, in any case, creates a junction between the lower and upper (covering) layers. This junction represents a source of mechanical strain during the subsequent high-temperature sintering of the tubes. Accordingly, monolayer tubes devoid of any junctions are preferable in terms of mechanical stability. There are numerous alternative technological approaches that facilitate the fabrication of high-quality tube substrates. Among these techniques, phase inversion with a combination of extrusion, spinning, slip casting, or dip coating has become a widely employed method [114, 115]. In particular, phase inversion entails the mixing of the corresponding oxide powders with an organic solvent (to create a slurry) and the subsequent introduction of a nonsolvent phase as a slurry destabilization agent. During the coagulation process, the substrate undergoes hierarchical restructuring, forming a dense layer (in the polymer-depleted region) connected with sponge-like or finger-like void layers (in the polymer-rich region). This method enables the fabrication of tubes from single materials (by extrusion, spinning) or two distinct materials (by co-extrusion, co-spinning).

Zhao *et al* [116] employed the phase inversion method to fabricate a microtubular PCFC based on a $BaCe_{0.7}Zr_{0.1}Y_{0.1}Yb_{0.1}O_{3-\delta}$ (BCZYYb) electrolyte. This electrolyte was synthesized via the citrate−nitrate synthesis method and subsequently ball milled with NiO and graphite in an ethanol medium. Polythersulfone (PESf) and N-methyl-2-pyrrolidone (NMP) were then added to form a viscous slurry. A custom-designed spinneret with an orifice dimension/inner diameter of 3.0/2.0 mm was used to obtain a microtubular substrate. The latter was immersed in a water bath to obtain a porous green tube. The green body was washed to remove any solvents, dried at 400 °C to burn off the organic components, and then pre-sintered at 1200 °C for 2 h. A dip-coating method was employed to form the BCZYYb electrolyte layer on the outer surface of the pre-sintered tube. An ethanol-based slurry containing 10 wt% BCZYYb was used for this purpose. The co-sintering of the half-cell with a 25 μm thick electrolyte was performed at 1400 °C for 5 h. Finally, an LSCF–BCZYYb cathode composition (where LSCF = $La_{0.6}Sr_{0.4}Co_{0.2}Fe_{0.8}O_{3-\delta}$) was formed on the electrolyte surface, followed by sintering at 1100 °C for 2 h. The single PCFC had an outer diameter of 1.6 mm and an effective electrode area of 0.65 cm^2.

Concurrent with these developments, a group of Zhao *et al* [117] employed a similar phase inversion methodology to fabricate microtubular PCFCs with graded anodes. In detail, the suspension for the anode supports was composed of NiO and BCZYYb powders in a NMP solvent with the addition of PESf and polyvinylpyrrolidone as the binder and dispersant, respectively. The suspension was then stirred for 24 h, degassed, and extruded through a tube-in-orifice spinneret with orifice diameters and inner diameters of 2.5 and 1.0 mm, respectively. The hollow fibers were then placed in a water bath for 24 h and pre-sintered at different temperatures from 1300 to 1400 °C for 5 h. The BCZYYb electrolyte was deposited on the outside side of the pre-sintered tubes by the dip-coating method and then co-sintered at 1300, 1350, and 1400 °C for 5 h. Finally, an SSC–BCZYYb cathode (SSC = $Sm_{0.5}Sr_{0.5}CoO_{3-\delta}$) was screen printed and sintered at 950 °C for 3 h. The cross-sectional microstructure analysis revealed that the pre-sintered tubes exhibited a graded structure, whereby a sponge-like porous layer formed on the outer side integrated with a finger-like porous layer on the inner tube sides. This asymmetric structure was likely caused by different precipitation rates during the spinning process. This fabrication technique, with some modifications, was subsequently confirmed to be effective for other electrolyte/electrode combinations [118–131].

Chen *et al* [132] fabricated a tubular BCZYYb-based PCFC via a combination of dip coating and co-firing processes. Dip coating is regarded as a relatively straightforward process, particularly in comparison to spinning or extrusion techniques. This does not necessitate the use of specialized tube production equipment, although the dimensions of the resulting tubes are somewhat constrained. For the research, the dip coating slurry was prepared in the following manner. First, the NiO, BCZYYb, and graphite components were ball milled in ethanol for 24 h (the weight ratio of the liquid and solid phases was set as 1:1). Then, triethanolamine was added as a dispersant, dibutyl phthalate and PEG-6000 were added as plasticizers, and PVB was added as a polymer binder. The resulting mixture was ball milled for another 24 h to obtain a uniform and stable slurry, which was finally degassed under vacuum. A glass rod was then dipped in the slurry and removed, followed by drying in air. The dip coating process was repeated 6 times to obtain a 200 μm thick anode substrate with an outside diameter of 6 mm. This substrate was demounted from the glass rod after drying in air for 12 h and in an oven at 80 °C for 30 min. A thin layer of the BCZYYB electrolyte (∼12 μm) was deposited onto the outside of the anode substrate via a similar dip coating method in which an ethanol slurry (10 wt% BCZYYb) containing small amounts of binder and dispersant was used. The as-prepared bilayer cell was co-sintered at 1400 °C for 5 cycles. A composite LSCF–BCZYYb cathode was subsequently applied to the electrolyte surface via brush painting, followed by sintering at 1000 °C for 2 h. The resulting single PCFC had a length of 2 cm, an outside diameter of 5 mm, an inside diameter of 4.5 mm, and an effective cathode area of 1.0 cm^2. In subsequent works, the same approaches were used to fabricate other PCFCs [133–141].

Robinson *et al* [142] utilized an extrusion method to prepare a Ni-cermet PCFC tube. First, initial $BaSO_4$, CeO_2, ZrO_2, Y_2O_3 and NiO reagents were used at a ratio corresponding to a nominal composition of 35 wt% $BaZr_{0.7}Ce_{0.2}Y_{0.1}O_{3-\delta}$ (BZCY) and 65 wt% NiO. No preliminary synthesis of the electrolyte component was used since this phase was self-formed during sintering. These components were ball milled for 16 h and then added to water-soluble acrylic or cellulosic plasticizer to prepare the extrusion batch. Green tubes (with an outer diameter of 13.8 mm and a wall thickness of 1.8 mm) were extruded from the prepared mass via a 40 ton extrusion press through an encapsulated die set and then dried in air for several days. A slurry of $BaSO_4$, CeO_2, ZrO_2 and Y_2O_3 in an unspecified solvent was spray coated onto the outer surface of the green extruded tubes, followed by co-sintering at 1600 °C for 6 h. After this sintering, the half-cells had an outer diameter of ∼10 mm, a wall thickness of 1.25 mm, and an electrolyte thickness of approximately 20 μm. Finally, a LSCF cathode was deposited via brush painting and sintered at 1000 °C for 30 min. This approach was used to prepare protonic ceramic electrochemical tubes (fabricated by CoorsTek Inc., Golden, Colorado, USA) for different purposes [143–151].

In the work of Min *et al* [152], a PCFC based on a $BaCe_{0.7}Zr_{0.1}Y_{0.2}O_{3-\delta}$ (BCZY) electrolyte was fabricated through a combination of extrusion and coating processes. The anode substrate was prepared from BCZY, NiO, and activated carbon powders, which were ball milled and mixed with an organic binder (the specific composition of which is not provided) and distilled water. The prepared paste was extruded and pre-sintered at 1100 °C for 3 h. Then, three layers were coated with subsequent sintering: an anode functional layer was dip-coated and sintered at 1200 °C for 3 h, the BCZY electrolyte was coated by a vacuum slurry coating method and sintered at 1450 °C for 5 h, and a LSCF–BCZY composite cathode was dip-coated and sintered at 1100 °C for 3 h. The resulting PCFC exhibited an active electrode area of approximately 2.1 cm^2. The same approaches were used for the fabrication of a PCFC tube with an outer diameter of 5 mm, an inner diameter of 4 mm, an overall length of 50 mm, a cathode length of 30.5 mm, and an electrolyte thickness of 10 μm [153, 154].

Zhu *et al* employed a highly scalable extrusion process to prepare green anode supports with a tubular design [155]. Specifically, 20 wt% corn starch (pore former) and 3 wt% methyl cellulose (water-soluble binder) were added to an initial powder mixture corresponding to BCZYYb and NiO at a weight ratio of 65:35. The resulting mixture was then ball milled for 15 h and subsequently mixed with water, followed by preextrusion. The ceramic clay was then packed into bricks, sealed, and aged for 16 h prior to tube extrusion. Following the aging process, the clay was introduced into the pressing chamber, subjected to slight vacuum conditions, and then extruded at a gradual rate. The extruded tubes were subsequently subjected to a gradual drying process at 30 °C for 3 h and at 80 °C for 5 h, which proved instrumental in achieving their optimal mechanical strength. The tubes subsequently underwent a two-hour pre-sintering process at 1200 °C. Thereafter, the BCZYYb electrolyte slurry was deposited onto the outer tube surface through brush painting, followed by a further sintering process at 1450 °C for 10 h. Finally, several cathode slurries were prepared from the $Ba_{0.5}Sr_{0.5}Co_{0.8}Fe_{0.2}O_{3-\delta}$ (BSCF), $BaCo_{0.4}Fe_{0.4}Zr_{0.1}Y_{0.1}O_{3-\delta}$, and $PrBa_{0.5}Sr_{0.5}Co_{1.5}Fe_{0.5}O_{6-\delta}$ (PBSCF) powders; each of these slurries was painted and fired at 900 °C for 5 h. This procedure enabled the fabrication of PCFC tubes with an outer diameter of 0.82 cm, a cathode length of 0.5 cm, an active cathode area of 1.3 cm^2, and an electrolyte thickness of 15 μm. A similar extrusion technique was further used in another work [156].

A slip casting technique was first used by Hanifi *et al* [157] to prepare a BCZYYb-based PCFC. The initial precursor powders ($BaCO_3$, ZrO_2, CeO_2, Y_2O_3, and Yb_2O_3), taken in the stoichiometric amounts required for BCZYYb, were mixed with NiO in deionized water and ball-milled for 24 h. Water was added to adjust the solid phase in the obtained slurry to 30 wt%, and then 20 vol% graphite was added as a pore former to obtain a final suspension. The latter was cast into a plaster mold for 30 s and dried at room temperature for 1 h. Upon drying, the green tubes shrank, which allowed their removal from the mold. These tubes were dried at 100 °C, heated at 700 °C to remove graphite, and pre-sintered at 1000 °C for 3 h. An electrolyte slurry (BCZYYb, ethyl cellulose, terpineol) in ethanol was formed on the outer surface of the pre-sintered tubes via the dip-coating method (twice), followed by co-sintering at 1450 °C for 3 h. Finally, a LSCF–BCZYYb cathode was also dip-coated and sintered at 1000 °C for 3 h. The electrolyte thickness of a single PCFC was about 25 μm. The next work of this group also reports the success of the proposed method [158–161].

The slip casting method in combination with dip coating was also employed for the preparation of tubular half-cells based on Zr-enriched cerate-zirconate materials, specifically $BaZr_{0.8}Ce_{0.1}Y_{0.1}O_{3-\delta}$ (BZCY1) and $BaZr_{0.7}Ce_{0.2}Y_{0.1}O_{3-\delta}$ (BZCY2) [162]. In detail, the initial powders of $BaCO_3$, ZrO_3, CeO_2, Y_2O_3, and NiO were taken in certain amounts required for either NiO/BZCY1 or NiO/BZCY2, with a weight NiO ratio of 65%. The ball-milled powders were dried and mixed with polyvinyl alcohol as a binder and Darvan 821A as a deflocculant in deionized water. The resulting slurries were then cast in a mold. This mold was inverted, and the excess slurry was poured out. The anode substrate tubes were subsequently removed from the mold and subjected to a dip coating process, thereby forming an electrolyte layer. The as-obtained green tubes (1.25 cm in diameter and 6 cm in length) were finally sintered with a maximum sintering temperature of 1550 °C (for 5 h); the shrinkage rate was approximately 22%. This slip casting/dip coating method allowed the fabrication of closed-end tubes with an electrolyte thickness of 20 μm. Although no counter electrode was applied, the proposed scheme can be regarded as a straightforward and cost- and time-effective approach for the preparation of short protonic ceramic tubes.

The slip casting method is a versatile technique that can be employed not only for the preparation of fuel electrodes but also for the preparation of electrolytes. For example, Kuzmin *et al* [163] fabricated 300 μm electrolyte tubes made of $La_{0.9}Sr_{0.1}ScO_{3-\delta}$ (LSS) by hot slip-casting under pressure. The corresponding slurry was prepared by mixing LSS with 10–20 wt% of a thermoplastic component consisting of paraffin wax and oleic acid at a weight ratio of 85:15. The cast tubes were subsequently subjected to sintering at 1650 °C for 5 h, after which the fuel and oxygen electrodes were arranged.

Medvedev *et al* [165] investigated the feasibility of a tape-calendaring method for the fabrication of a 5-layer PCEC. In detail, three different oxide/organic films were separately prepared, comprising an electrolyte film, a cathode functional film (NiO:BCZD ratio of 55:45) and a cathode supporting film (NiO:BCZD:strach ratio of 65:35:20) with varying weight ratios of the components. The three films were then rolled together in a specific manner, maintaining a thickness for the electrolyte of approximately 30 μm. The three-layered film was subsequently twisted into a tube, slowly heated in static air up to 900 °C, and then co-sintered at 1400 °C in static air with a soaking time of 3 h. Subsequently, an oxygen $Pr_{1.95}Ba_{0.05}NiO_{4+\delta}$ electrode was sprayed onto the electrolyte surface, followed by its final sintering at 1000 °C for 2 h. The detailed compositions of the films were presented in a previous study conducted by the same research group [166]: each powder was homogenized in an agate mortar in acetone media. Then, a 4 wt% solution of nitrile butadiene rubber (solved in gasoline and acetone at a 3:2 volume ratio) was added to 1.2 ml of solution per 1 g of dry powder. The resulting slurries were poured onto Teflon substrates and air-dried to evaporate the solvent. Although the tube produced by the proposed method was successfully tested as a single PCEC, the same disadvantages inherent to the tape casting technique remain. These include the necessity of rolling the obtained tapes, which creates junctions.

Isostatic pressing combined with the dip-coating technique was reported by Chen *et al* [167, 168]. First, the hydrogen electrode support was prepared by isostatic pressing at 150 MPa with the mixed materials (60 wt% NiO, 40 wt% $BaCe_{0.5}Zr_{0.4}In_{0.1}O_{3-\delta}$ (BCZI) and 30 wt% carbon pore formers), followed by calcination at 1100 °C. Subsequently, the anode functional NiO–BCZI and BCZI electrolyte layers, with a thickness of ~15 μm, were dip-coated and co-sintered at 1450 °C for 3 h. Finally, an oxygen electrode of LSC–BCZI (where LSC = $La_{0.6}S_{0.4}CoO_{3-\delta}$) was fabricated.

Recently, Zou *et al* [169, 170] described the fabrication of highly scalable single tubular PCFCs with an overall area of 15.7 cm^2 (a working electrode area of 12.5 cm^2) via a novel 3D printing technique. The success of this approach was contingent upon the integration of digital microextrusion- and digital spray-coating-based additive manufacturing with

CO_2-laser drying (the details of the equipment are provided in [169]). A mixture of BZCY and NiO was employed as a solid phase. These powders were subsequently mixed with dispersant (1.5 wt% Darven 821), deionized water (13.2 wt%), and binder (∼0.3 wt% hydroxypropyl methylcellulose), followed by vacuum centrifugal mixing for approximately 30 min. The paste was then pushed by compressed air to the microextruder, which was equipped with a needle-type nozzle with an inner diameter of 0.5 mm. The speed, dispensing, and trajectory were regulated. CO_2-laser scanning of the layer surface was subsequently employed to accelerate the drying process of the printed wet layer and enhance geometric retention. The green cap-closed tubes have inner and outer diameters of 5 and 7 mm, respectively. The electrolyte and cathode layers were subsequently spray-coated with the corresponding sintering at 1500 °C for 12 h and 900 °C for 5 h, respectively.

The majority of the proposed techniques require the meticulous preparation of oxide−organic mixtures, which are utilized as slurries, pastes, clays, or tape masses. These masses need to be stable in terms of homogeneity and exhibit certain physicochemical properties, including viscosity, absence of bubbles, improved particle separation, etc. Consequently, various components (binders, surfactants, dispersants, and plasticizers) may be added to adjust the requisite functions. Table 1 offers insight into the preparation of oxide−organic mixtures for a range of manufacturing approaches, whereas figure 5 presents a selection of pertinent images.

5. Application of tubular protonic ceramic cells

This section highlights a variety of protonic ceramic electrochemical tubes for applied purposes [5, 171–173]: possible applications include not only energy/electricity conversion realized in PCFCs or PCECs but also hydrogen permeation, hydrogen sensing, and hydrogen pumping. Let us begin our discussion with the latter applications, while the characterization of conventional PCFCs and PCECs will be presented later.

5.1. Hydrogen permeation membranes

In most high-temperature solid oxide devices, an electrolyte material serves as a central gas-tight layer of multilayered cells. The electrolyte facilitates ion conduction through its own body and simultaneously separates different gas spaces, thereby preventing nonelectrochemical gas mixing. To achieve a high level of efficiency in electrochemical conversion, ionic transport must dominate over electronic transport. This is the reason why the design of highly conductive ionic electrolytes is highly important. It is evident that a wide range of compounds demonstrate both electronic and ionic conductivity. This feature enables their utilization as electrode materials in the mentioned electrochemical systems. Nevertheless, the mixed ionic−electronic transport nature is advantageous for the design of permeating membranes, whose driving force is regulated by ambipolar conductivity and partial pressure differences [174–178]. In the case of such membranes, the use of electrodes is not necessary, as the electronic and ionic currents flow through the membrane materials and are not separated into different pathways (electrolytes and external circuits), as takes place for anode|electrolyte|cathode cells. In other words, electrochemical reactions, which involve ionic and electronic charge carriers, occur at gas/solid interfaces.

The reviews cited above have focused primarily on oxygen-permeable membranes, which are composed of oxygen-ionic and electronic conductors (MIECs). When such materials exhibit pronounced proton transport instead of oxygen transport, hydrogen-permeable membranes can be developed in the same manner. Importantly, hydrogen-permeable membranes can be made of either single-phase materials or composite materials (when one component provides high electronic conductivity while another component provides high proton conductivity). In both cases, however, the central layer of the membranes must be completely dense and gas-tight.

The hydrogen permeation flux (J_{H_2}, mol min^{-1} cm^{-2} or ml min^{-1} cm^{-2}) is one of the main functional properties of the membranes; it is governed by internal and external parameters. A simple relationship between these factors can be derived from the Wagner equation if proton diffusion is a rate-limiting step in overall membrane transport:

$$J_{H_2} = \frac{RT}{2^2F^2L}\int_{p'H_2}^{p''H_2}\frac{\sigma_{el}\cdot\sigma_{H^+}}{\sigma_{el}+\sigma_{H^+}}\,\mathrm{d}\ln pH_2. \tag{2}$$

Here, R is the universal gas constant, T is the absolute temperature, F is the Faraday constant, L is the membrane thickness, $p'H_2$ and $p''H_2$ are the hydrogen partial pressures at the opposite membrane sides, and σ_{el} and σ_{H+} are the electronic and protonic conductivities of the membrane material.

As shown in equation (2), the J_{H_2} values increase with increasing ambipolar conductivity, decreasing membrane thickness (internal parameters of the material used), increasing temperature, and increasing hydrogen partial pressure gradient (external parameters of the experimental conditions). Therefore, to obtain high hydrogen fluxes, it is reasonable to use thin-layer MIEC membranes at elevated temperatures and high potential-determined gradients. From a technological viewpoint, the fabrication techniques described in section 4 are convenient for preparing single-layer or asymmetrical double-layer membranes with highly effective working areas.

Table 2 lists the experimental results related to the characterization of the hydrogen permeation membranes. The majority of these membranes were produced through phase inversion-assisted methodologies, which demonstrated their considerable potential in the field of membrane technology. These membranes have the potential to achieve hydrogen flux values of 1 ml min^{-1} cm^{-2} at 750 °C and 3 ml min^{-1} cm^{-2} at 900 °C. However, notably, fluxes can vary significantly, up to two orders of magnitude. This highlights the fact that the target properties of the membranes are dependent on a variety of factors. Some details of the best performance examples are briefly discussed below.

Table 1. The technological details related to the preparation of green tapes of protonic ceramic electrochemical tubes.

Method	Powder sources	Solvents	Organic additives	References
Tape-casting	SC and NiO	Ethanol/toluene	Fish oil (dispersant), polyvinyl butyral, polyethylene glycol, di-n-butyl phthalate.	[111]
Phase inversion	$BaCe_{0.7}Zr_{0.1}Y_{0.1}Yb_{0.1}O_{3-\delta}$ (BCZYYb), NiO, graphite	Ethanol	Polythersulfone (PESf), N-methyl-2-pyrrolidone (NMP), the weight ratio of BCZYYb and PESf + NMP was 1:1.	[116]
Phase inversion	BCZYYb, NiO, graphite	NMP	PESf (binder), polyvinylpyrrolidone (dispersant); the weigh ratios of NiO, BCZYYb, PESf, NMP and PVP were 36.0, 24.0, 6.4, 32.0, and 1.6%, respectively.	[117]
Phase inversion	BCZYYb, NiO	NMP	Ethyl cellulose (EC), polyvinylidene fluoride (PVDF), polyetherimide (PEI). The weight ratio of the polymer binder, solvent and ceramic powder was set to 1:7:10.	[122]
Phase inversion	BCZYYb, NiO, graphite	Ethanol	Triethanolamine (TEA), polyvinyl butyral (PVB), polyethylene glycol (PEG); the weight ratio of Ni–BCZYYb, ethanol, TEA, PVB, PEG and graphite was set to 5.5:4.5:10:0.6:2:1:1, respectively.	[126]
Dip coating of a glass rod + phase inversion	BCZYYb, NiO, graphite	Ethanol	Triethanolamine (TEA, dispersant), dibutyl phthalate (DBP, plasticizer), PEG-6000 (plasticizer), and PVB (polymer binder); TEA:DBP:PEG:PVB:slurry = 0.6:1:1:2:20 g, where the slurry is a mixture of solvent and solid phases in 1:1 weight ratio.	[132]
Dip coating	$BaCe_{0.7}Zr_{0.1}Y_{0.2}O_{3-\delta}$ (BCZY), NiO, corn starch	Ethanol	The as-prepared BCZY7 powder, NiO powder, and corn starch in a weight ratio of 40:60:10 were mixed with 4.8 wt% PVB, 1.7 wt% TEA, 2.9 wt% dioctyl phthalate (DOP) and 2.9 wt% PEG-600 in 50.7 wt% ethanol.	[135]
Extrusion	$BaSO_4$, CeO_2, ZrO_2, Y_2O_3 corresponding to a nominal $BaZr_{0.7}Ce_{0.2}Y_{0.1}O_{3-\delta}$ (BZCY) composition and NiO	Water	Acrylic and cellulosic ether plasticizer	[142]
Slip-casting	BCZYYb, NiO, graphite	Water	—	[157]
Hot slip-casting	$La_{0.9}Sr_{0.1}ScO_{3-\delta}$ (LSS)	—	LSS with 10–20 wt% of a thermoplastic component consisting of paraffin wax and oleic acid, taken in a weight ratio of 85:15	[164]
Tape-calendaring	Anode or electrolyte powders	Acetone/gasoline	The powder with a 4 wt% solution of nitrile butadiene rubber (solved in gasoline and acetone in a 3:2 volume ratio). A ratio of 1.2 ml of solution per 1 g of dry powder.	[165]
3D printing	BZCY and NiO	Water	Powders with 1.5 wt% of Darven 821 as a dispersant, 0.3 wt% of hydroxypropyl methylcellulose as a binder.	[169]

Chen *et al* [121] prepared LWM-based hollow-fiber membranes (LWM = $La_{5.5}W_{0.6}Mo_{0.4}O_{11.25-\delta}$) via the wet-spinning phase-inversion method, as shown in figure 6(a). The resulting U-shaped tubes were subsequently subjected to sintering at 1500 °C, which facilitated the effective densification of the central region of the membranes while maintaining a slightly porous structure on their inner surface. These membranes were tested at different temperatures (from 700 to 975 °C), and gas was supplied to the feed and sweep sides. The lowest hydrogen fluxes were observed for the dry gases used for the feed (20%He/H_2) and sweep (Ar) sides. The fluxes were slightly greater when the feed side was humidified because of the hydration of the membrane material (equation (1)). However, when the sweep gas flow was humidified instead of the feed gas flow, a notable increase in the hydrogen flux was observed (by ~3 times), reaching approximately 1 ml min^{-1} cm^{-2} at 900 °C. The authors attributed this improvement to the enhanced proton conductivity within the LWM material, and an additional water splitting process occurred at the sweep gas/solid interface. In the fourth case, when both sides were humidified, the hydrogen flux slightly decreased in comparison with the best result, potentially due

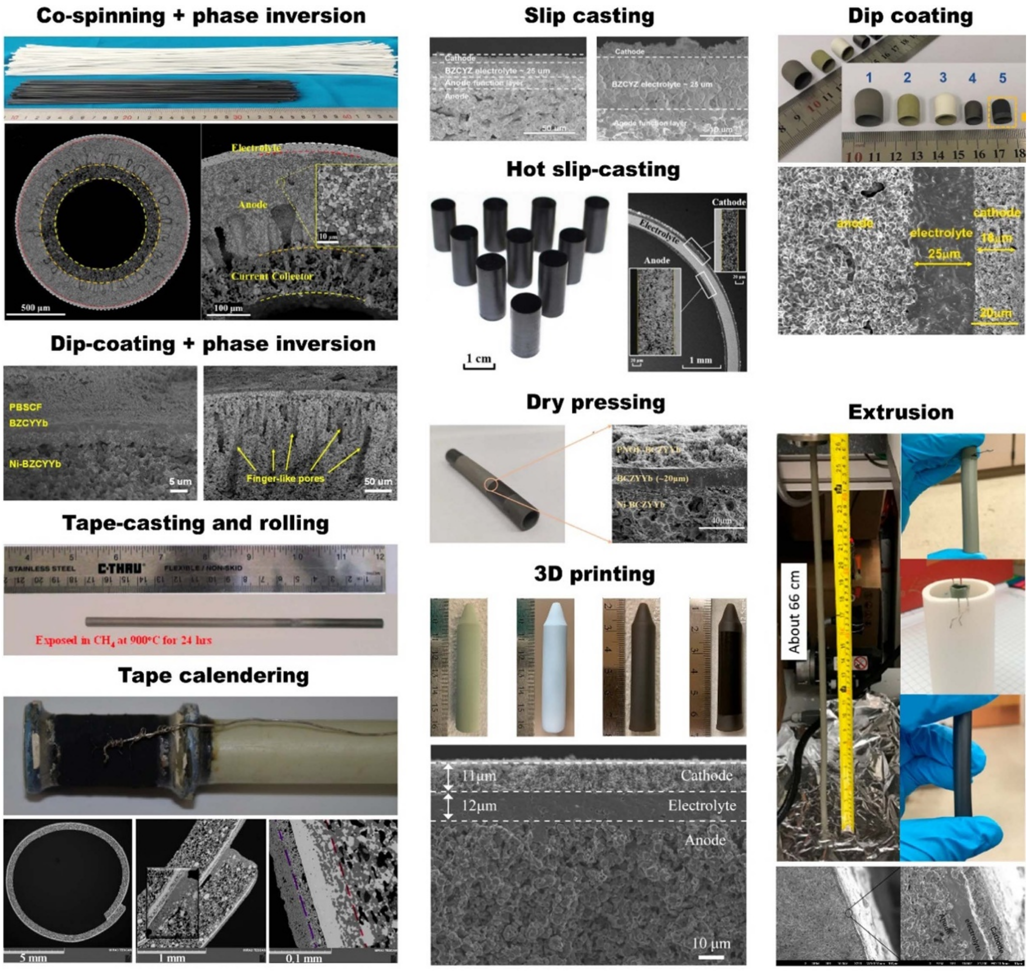

Figure 5. Images and microphotographs of the fabricated protonic ceramic electrochemical cell tubes. The presented panels were reproduced from different sources: Co-spinning and phase inversion. Reprinted from [131], © 2023 Elsevier B.V. All rights reserved. Reproduced from [161]. CC BY 4.0. Reprinted from [164], © 2019 Science Press and Dalian Institute of Chemical Physics, Chinese Academy of Sciences. Published by Elsevier B.V. and Science Press. All rights reserved. Reproduced from [135]. CC BY 4.0. Reprinted from [140], © 2023 Elsevier Ltd All rights reserved. Reproduced from [113]. © 2010 ECS—The Electrochemical Society. All rights reserved. Reprinted from [154], © 2021 Elsevier B.V. All rights reserved. Reprinted from [155], © 2021 Hydrogen Energy Publications LLC. Published by Elsevier Ltd All rights reserved. Reprinted from [165], © 2016 Elsevier Ltd All rights reserved. Reprinted from [170], © 2017 Elsevier B.V. All rights reserved.

to a decrease in the hydrogen partial pressure gradient. These findings offer valuable insights into the potential optimization of permeation processes through the manipulation of external gas conditions.

Tan *et al* [182] prepared a double-layer Ni–SCZ|SCZE membrane by rolling the green tape cast into the tube (SCZ = $SrCe_{0.8}Zr_{0.2}O_{3-\delta}$, SCZE = $SrCe_{0.7}Zr_{0.2}Eu_{0.1}O_{3-\delta}$). The green cermet substrate was prepared by rolling a tape-cast substrate and pre-sintering it at 1300 °C. The SCZE-containing slurry was then coated on the outer surface of the tube and sintered at 1520 °C in air, as shown in figure 6(b). They also studied the hydrogen permeation behavior of the developed membrane under different gas compositions at the feed side (the sweep side was fed with pure He). The experimental results revealed that the hydrogen flux decreases with increasing humidity, from dry H_2 to 30% H2O/H_2. On the one hand, more protons appear due to deeper hydration of the SCZE material; this should improve the hydrogen flux due to a higher proton conductivity (equation (2)). On the other hand, the presence of water in H_2 increases the oxygen partial pressure, making this atmosphere less reduced. As a result, the ambipolar conductivity decreases owing to the n-type electronic conductivity, resulting in a decrease in the hydrogen flux. Furthermore, the hydrogen partial pressure difference, which acts as a driving force, also decreases. Consequently, both the protonic and electronic conductivities must be optimized to achieve optimal membrane performance. This study reveals a crucial finding: a trade-off invariably exists between the intrinsic transport properties of the membranes and the gradient differences. Typically, the enhancement of one parameter is accompanied by the degradation of another parameter.

In general, the hydrogen fluxes of MIEC membranes are not particularly high (table 2), as their permeation performance is primarily determined by the driving force, which includes partial pressure differences and the intrinsic level of ambipolar conductivity, as illustrated by equation (2). To achieve

Table 2. The hydrogen permeation flux ($\boldsymbol{J}_{\mathbf{H_2}}$) of mixed protonic and electronic conducting (MPEC) membranes depending on their manufacturing methods: h is the membrane thickness, s is the effective working area, and pH_2O is the partial pressure of water vapor. Abbreviations: TC—tape casting, R—rolling, SC—slurry coating, PI—phase inversion, E—extrusion, S—spinning, DC—dip-coating, CC—colloidal coating.

Membrane[a]	h (μm)	Support[b]	s (cm^2)	Manufacturing methods	$\boldsymbol{J}_{\mathbf{H_2}}$ (ml min^{-1} cm^{-2})					Gas composition: feed side/sweep side	References
					700 °C	750 °C	800 °C	850 °C	900 °C		
SCE	30	NiO–SC	12	TC, R/SC	0.09	—	0.24	0.39	0.56	wet (H_2 + Ar) [$pH_2O = 0.03$ atm]/He	[112]
SCZE	—	NiO–SCZ	12	TC, R/SC	—	—	—	—	0.01	wet (5 vol.% CO + Ar) [$pH_2O = 0.03$ atm]/-	[113]
NiO–BCZY	150	—	—	PI, E	—	—	—	—	0.71	20% H_2 + N_2/Ar	[119]
LWM	200	—	1.44	PI, S	0.24	0.37	0.57	0.76	1.05	80% H_2 + He/wet Ar [$pH_2O = 0.04$ atm]	[121]
LWM	200	—	1.44	PI, S	0.13	0.20	0.27	0.33	0.40	dry (80% H_2 + He)$^{(c)}$/dry Ar$^{(c)}$	[121]
BCTb	15	NiO–BCTb	—	PI, S/DC	0.27	0.35	0.46	0.54	—	50 vol.% H_2 + He/He	[123]
NWM	170	—	0.66	PI, S	—	0.15	0.23	0.34	0.47	dry (50% H_2 + He)$^{(c)}$/dry Ar$^{(c)}$	[124]
NWM	170	—	0.66	PI, S	—	0.19	0.26	0.42	0.63	50% H_2 + He/wet Ar [$pH_2O = 0.04$ atm]	[124]
Ti_4O_7-doped SCY	—	—	—	PI, E	0.05	0.08	0.10	0.13	0.17	50 vol.% H_2 + He/N_2	[125]
Ti_4O_7-doped SCY	—	—	—	PI, E	0.01	0.09	0.17	0.32	0.57	50 vol.% H_2 + He/N_2 + CO_2	[125]
BCY–YDC	17	NiO–BCY	—	PI, co-E	0.76	0.94	0.97	1.14	1.45	50% H_2 + He/wet N_2 [$pH_2O = 0.03$ atm]	[147]
BCY–YDC	17	NiO–BCY	—	PI, co-E	0.15	0.29	0.70	1.95	3.00	50% H_2 + He/20% CO_2 + N_2	[147]
SCYb	250	—	—	PI, S	—	—	0.02	0.04	0.12	35.9% H_2 + Ar/dry air$^{(c)}$	[179]
BCY	190	—	—	PI, S	—	—	0.06	0.16	0.20	H_2 + He/N_2	[180]
BCTbC	—	—	—	PI, S	0.03	—	0.07	—	0.15	50 vol.% H_2 + He/N_2	[181]
SCZE	33	NiO–SCZ	12	TC, R/CC	0.70	1.08	1.62	2.18	2.55	wet H_2 [$pH_2O = 0.03$ atm]/He	[182]
SCZE	33	NiO–SCZ	12	TC, R/CC	0.88	1.35	1.78	2.44	2.77	dry $H_2^{(c)}$/He	[182]
BCTb	300	—	—	PI, S	0.03	0.04	0.11	0.21	0.34	50% H_2 + He/N_2	[183]
BCY–YDC	17	NiO–BCY	—	co-E	0.25	0.31	0.38	0.47	0.60	50% H_2 + He/N_2	[184]
BCTbZ	14	NiO–BCTbZ	—	PI, co-S	—	0.26	0.30	0.36	0.41	50 vol.% H_2 + He/N_2	[185]
BCTbZ	14	NiO–BCTbZ	—	PI, co-S	—	0.27	0.31	0.38	0.45	50 vol.% H_2 + He/12 vol.% CO_2 + N_2	[185]
SCZE	17	NiO–SCZ	12	TC, R/SC	—	—	0.17	0.29	0.50	wet H_2 [$pH_2O = 0.03$ atm]/He	[186]

[a] SCE = $SrCe_{0.9}Eu_{0.1}O_{3-\delta}$, SCZE = $SrCe_{0.7}Zr_{0.2}Eu_{0.1}O_{3-\delta}$, BCZY = $BaCe_{0.7}Zr_{0.1}Y_{0.2}O_{3-\delta}$, LWM = $La_{5.5}W_{0.6}Mo_{0.4}O_{11.25-\delta}$, BCTb = $BaCe_{0.95}Tb_{0.05}O_{3-\delta}$, NWM = $Nd_{5.5}W_{0.5}Mo_{0.5}O_{11.25-\delta}$, SCY = $SrCe_{0.9}Y_{0.1}O_{3-\delta}$, BCY = $BaCe_{0.8}Y_{0.2}O_{3-\delta}$, YDC = $Ce_{0.8}Y_{0.2}O_{2-\delta}$, SCYb = $SrCe_{0.95}Y_{0.05}O_{3-\alpha}$, BCTbC = $BaCe_{0.85}Tb_{0.05}Co_{0.1}O_{3-\delta}$, BCTbZ = $Ba_{0.95}Ce_{0.85}Tb_{0.05}Zr_{0.1}O_{3-\delta}$.

[b] SC = $SrCeO_3$, SCZ = $SrCe_{0.8}Zr_{0.2}O_{3-\delta}$.

[c] pH_2O is not specified.

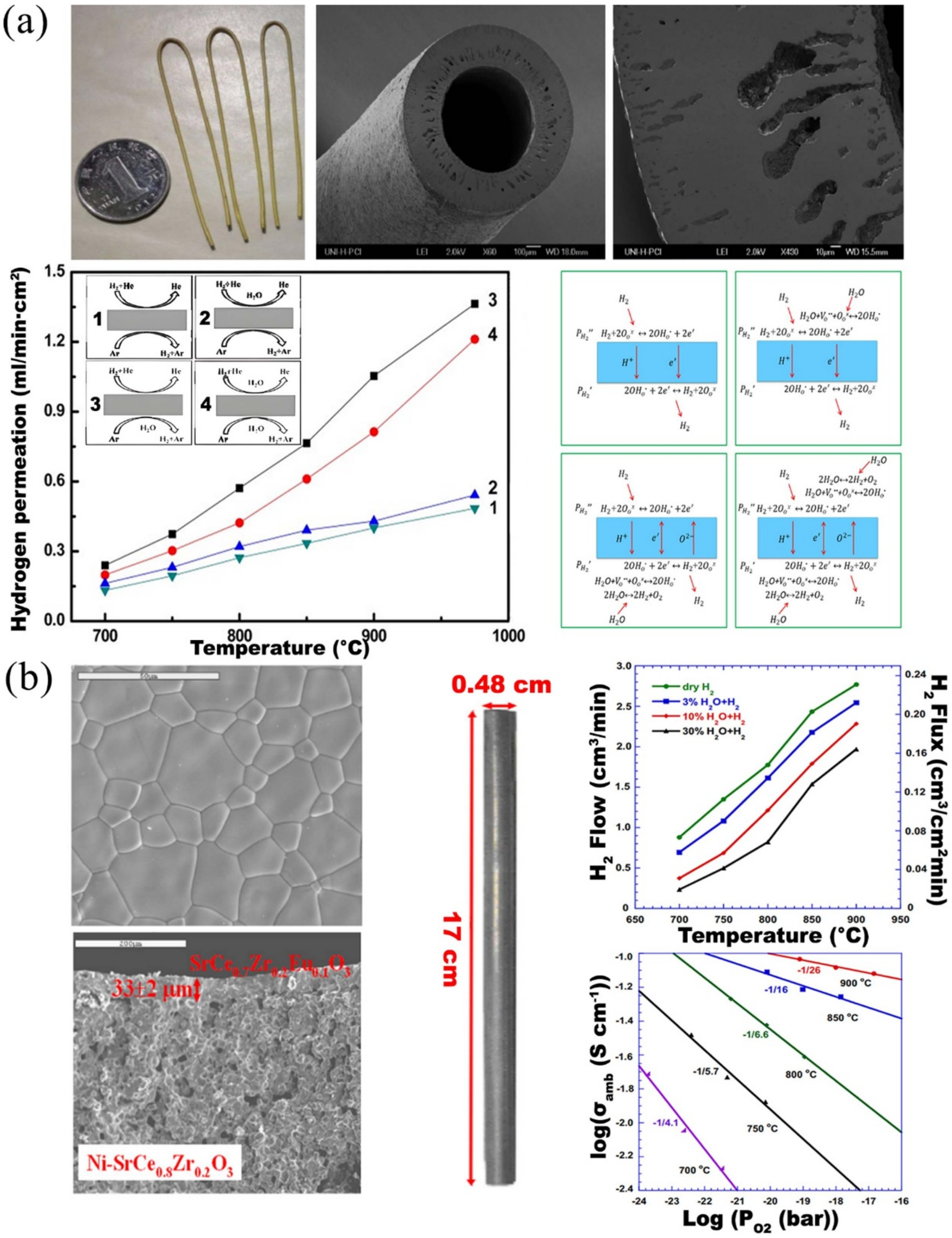

Figure 6. Selected results of tubular-type protonic ceramic hydrogen-permeable membranes: (a) Image and microphotograph of the U-shaped LWM-based hollow-fiber membranes and their performance under different experimental conditions. Copyright 2011, Elsevier B.V [121]. John Wiley & Sons. © 2015 American Institute of Chemical Engineers. (b) Image and microphotography of the SCZE-based membrane along with its hydrogen permeation fluxes and ambipolar conductivity at different feed gas compositions. Reprinted from [182], Copyright © 2012 Elsevier Ltd All rights reserved.

higher hydrogen flux values, an external current source can be employed to facilitate proton flow from the H_2-rich side to the counter side. However, this represents a fundamental shift in the conceptualization of electrochemical devices. To separate the ionic and electronic flow currents along distinct pathways, the classical electrode|electrolyte|electrode system must be employed, wherein the ionic current flows through the electrolyte, whereas the electronic current flows through the external circuit coupled with a direct current source. In other words, MIEC membranes should be replaced with electrolyte membranes. These electrochemical systems are discussed below.

5.2. Hydrogen pumps

Protonic ceramic hydrogen pumps are a type of electrochemical device that uses an external current to facilitate the pumping of protons from hydrogen-containing atmospheres (equations (3) and (4)); these protons then permeate to the opposite side of an electrolytic layer, where they produce molecular hydrogen (equation (5)) or reduce oxidized substances (equations (6)–(9)). In this regard, the PCEC (which will be discussed in detail in section 5.5) represents a particular case of hydrogen pumps, in which two specific reactions (equations (3) and (5)) occur simultaneously at the anode and cathode sides, respectively.

$$2H_2O_{(gas)} \rightarrow 2H^+_{(electrolyte)} + O_{2(gas)} + 2e'_{(electrode)} \tag{3}$$

$$H_{2(gas)} \rightarrow 2H^+_{(electrolyte)} + 2e'_{(electrode)} \tag{4}$$

$$2H^+_{(electrolyte)} + 2e'_{(electrode)} \rightarrow H_{2(gas)} \tag{5}$$

$$2H^+_{(electrolyte)} + 2e'_{(electrode)} + CO_{2_{(gas)}} \rightarrow H_2O_{(gas)} + CO_{(gas)} \tag{6}$$

$$6H^+_{(electrolyte)} + 6e'_{(electrode)} + CO_{(gas)} \rightarrow H_2O_{(gas)} + CH_{4(gas)} \tag{7}$$

$$2H^+_{(electrolyte)} + 2e'_{(electrode)} + NO_{(gas)} \rightarrow H_2O_{(gas)} + N_{2(gas)} \tag{8}$$

$$3H^+_{(electrolyte)} + 3e'_{(electrode)} + N_{2(gas)} \rightarrow NH_{3(gas)}. \tag{9}$$

Tanaka and Ohshima [187] were the first to propose the use of a tubular cell as a hydrogen pump. The tube, with an outer diameter of 15 mm, an inner diameter of 12 mm, and a length of 200 mm (figure 7(a)), was constructed from a proton-conducting $BaZr_{0.955}Y_{0.03}Co_{0.015}O_{3-\delta}$ (BZYC) material, followed by the symmetrical organization of Pt electrodes with an active area of 47 cm^2. Unfortunately, this study does not offer any insights into the fabrication process of the tube. The primary objective of this study was to assess the transport behavior of the BZYC electrolyte in diverse operational scenarios. For example, in water electrolysis mode, BZYC demonstrated a mixed character of transport, wherein protonic and electronic conductivities coexisted within a temperature range of 350 °C–600 °C. Conversely, in hydrogen pumping mode, BZYC was found to be a triple-conducting material, enabling the simultaneous transport of oxygen ions, protons, and electrons within the same temperature range. In another study, the same authors tested similar sensors but again without providing any details regarding the fabrication of the tubes [188].

A little later, a BZCY galvanic pump was fabricated and tested by Robinson *et al* [143]. To prepare a membrane reactor of Ni–BZCY|BZCY|LSCF with an active area of 22 cm^2, slip-casting, spray-coating, and brush painting approaches were used for the preparation of the Ni–BZCY support, thin electrolyte, and oxygen electrode layers, respectively (figure 7(b)). The tubular-type reactor was affixed with a supporting tube, and a test stand was constructed to perform hydrogen pumping experiments. Once the NiO–BZCY had been sealed and reduced to the corresponding cermet, the inner space of the tube reactor was supplied with a gas composition of 50:50 H_2/He humidified with 5 vol.% water vapors, whereas the external space was supplied with 10% H_2O/Ar. The experimental data indicated that the hydrogen flux increased with increasing cell voltage (in absolute values) and temperature (from 650 °C to 775 °C). This resulted in a maximal level of 6.0 ml min^{-1} cm^{-2} at 775 °C with a current density of 800 mA cm^{-2}. In addition to the experimental hydrogen flux, which was measured by a mass spectrometer, the theoretical (Faradaic) hydrogen flux was also calculated. Specifically, the Faradaic efficiency, defined as the ratio of the measured and theoretical fluxes, exceeded 95% for temperatures between 750 °C and 775 °C and current densities between 600 and 800 mA cm^{-2}. These conditions correspond to the optimal range for the BZCY membrane, which has high electrical conductivity and low electronic conductivity, thereby ensuring effective transport properties.

In a recent study, Li *et al* [127] developed a dual-layer hollow-fiber Ni–BCZY|BCZY membrane through a multistep process involving co-spinning and co-sintering techniques, followed by the organization of a Ag counter electrode. The tube had a working length of 5 cm^2 and a working electrode area of 1.9 cm^2 (figure 7(c)). The membrane was subjected to testing under various experimental conditions to measure the hydrogen flux and hydrogen recovery values. The experimental results indicated that a temperature range of 500 °C–550 °C was optimal for galvanic hydrogen pumping, as it exhibited relatively high hydrogen fluxes and a high Faradaic efficiency. At more elevated temperatures, the measured hydrogen content decreased due to the potential emergence of n-type electronic conductivity in the BCZY electrolyte. However, the presence of a high hydrogen concentration in the feed gas or wet feed gas could mitigate the adverse impact of electronic conductivity in the electrolyte. Furthermore, high-purity hydrogen can be recovered from a diluted hydrogen stream (8%H_2/He or 13%H_2/He) with a recovery rate of 81%–89%.

Patki *et al* [145] focused on the optimization of bimetallic electrodes (Ru/Cu, Pd/Cu, and Cu/Cu) for tubular galvanic hydrogen pumps fabricated by CoorsTek Inc. (figure 7(d)). The hydrogen flux was measured via a stoichiometric titration experiment, with the highest flux (3.1 ml cm^{-2} min^{-1}) obtained with the Ru/Cu electrode at 400 mA cm^{-2}. In addition, hydrogen was pumped from a methane-containing gas (10%H_2/CH_4). Although both the hydrogen flux and Faradaic efficiency values were satisfactory, coke formation was observed over the electrolyte surface and was not detected for the Ru/Cu electrode. Coking was attributed to the presence of Ni ions in the electrolyte, which was preliminarily obtained by the use of NiO as a sintering additive. In detail, Ni ions reduce and act as nucleation sites for coke formation at the electrode/electrolyte interface and may affect electrode performance.

A comprehensive electrochemical characterization of a hydrogen separation Ni–BZCY|BZCY|Ni–BZCY tubular-type membrane was conducted by Yuste-Tirados *et al* [151], who employed electrochemical impedance spectroscopy (EIS), distribution of relaxation time (DRT) analysis, voltammetry in conjunction with EIS, and gas chromatographic analysis. The researchers identified three distinct regions depending on the current applied to the cell. At low current densities, hydrogen pumping from a wet H_2-containing atmosphere is characterized by a high Faradaic efficiency, which can be attributed to the almost proton transport nature of the electrolyte. As the current density increases,

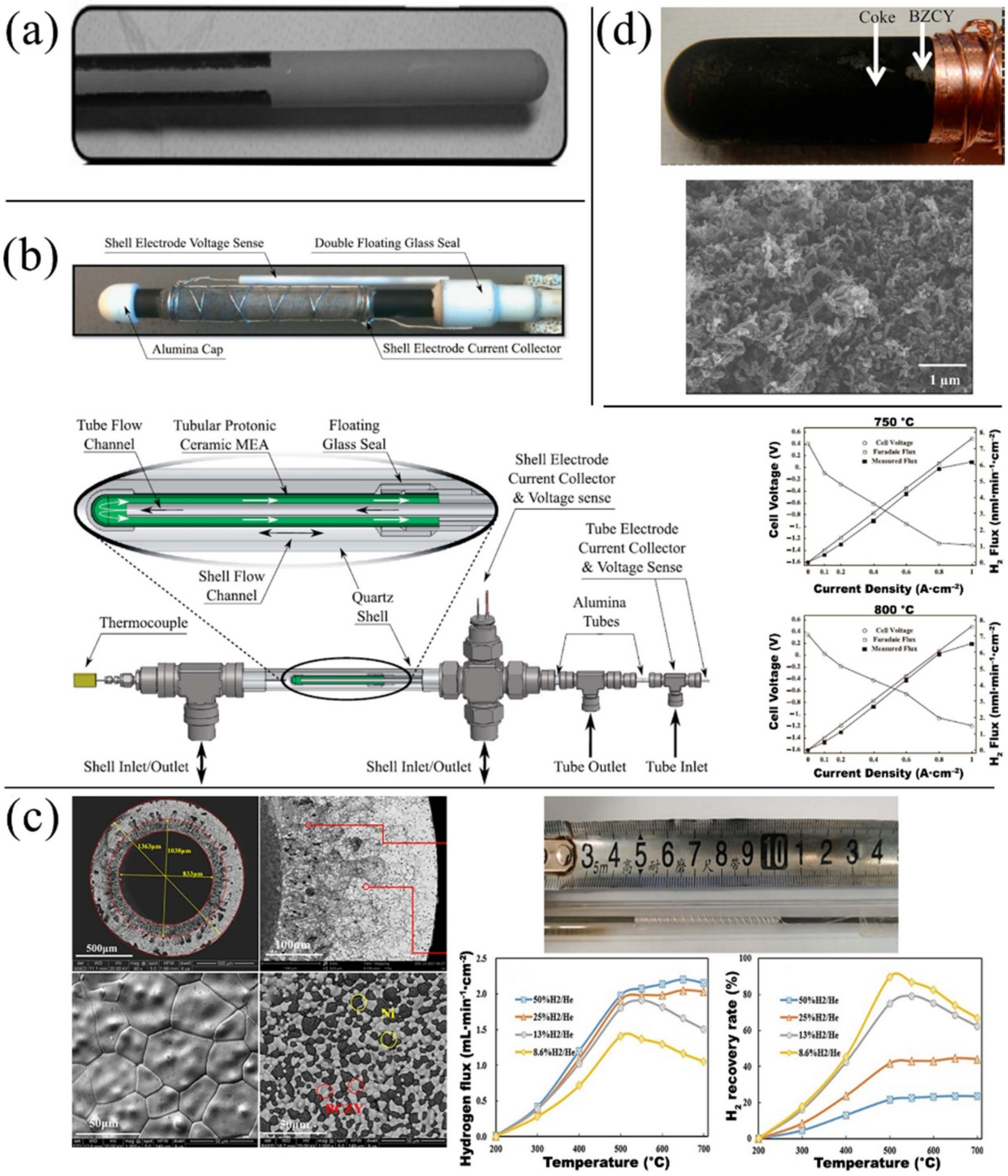

Figure 7. Selected results of tubular-type protonic ceramic electrochemical pumps: (a) A general view of the BZYC tubular pump. Reprinted from [187], Copyright © 2009 Elsevier B.V. All rights reserved; (b) posttesting image of the hydrogen pump, testing scheme, and voltampere and faradaic dependences at two temperatures. Reprinted from [143], Copyright © 2013 Elsevier B.V. All rights reserved. (c) Image of the hollow-fiber electrochemical cell, its microstructural features and electrochemical performance. Reprinted from [127], © 2022 Elsevier B.V. All rights reserved. (d) Image and electrolyte surface micrograph of the membrane pump operated in 10%H_2/CH_4 at 700 °C. Reprinted from [145], © 2018 Elsevier B.V. All rights reserved.

the diffusion limitations of the gas phase become more pronounced, leading to hydrogen pumping from water instead of molecular H_2. As the water content decreases, the proton conductivity of BCZY also decreases, resulting in an increase in the nonionic (electronic) conductivity. At very high current densities, the feed side is nearly devoid of water, resulting in a diminished hydrogen production rate and a reduction in Faradaic efficiency.

5.3. Hydrogen sensors

Hydrogen sensors based on proton-conducting oxides offer a diverse range of analytical possibilities, including high-temperature analysis of not only hydrogen- or water-containing gas mixtures but also those containing O_2, CO, CO_2, and NO_x [189–191]. In the majority of cases, such sensors are constructed in a plate-type (planar) configuration owing to the simplicity and diminutiveness of this design. However, several studies have reported the application of tubular protonic ceramic sensors as well.

Hassen *et al* [192] tested the fabrication and characterization of tubular sensors made of either $SrCe_{0.95}Yb_{0.05}O_{3-\delta}$ (SCY) or $SrCe_{0.95}Nd_{0.05}O_{3-\delta}$ (SCN) electrolytes. These materials were obtained via the standard solid-state synthesis technique with final sintering at 1300 °C for 17 h to reach their single-phase state. The materials were subsequently crushed

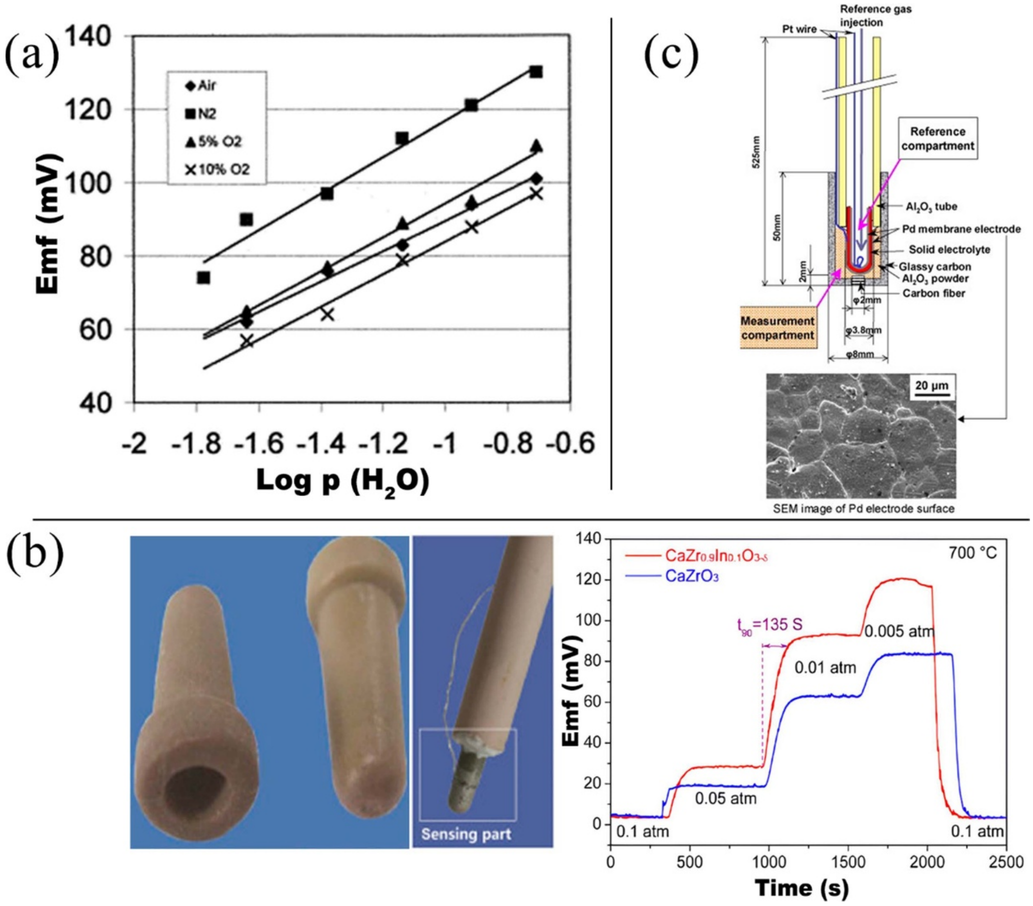

Figure 8. Selected results of the tubular-type protonic ceramic electrochemical sensors: (a) emf response of the SCY sensor depending on the humidity level in different gases at 300 °C. Reprinted from [192]. Copyright © 2016 Elsevier B.V. All rights reserved; (b) image and emf performance of the CZI sensor depending on the hydrogen partial pressure in Ar at 700 °C. Reprinted from [193]. Copyright © 2010 Elsevier B.V. All rights reserved. (c) Schematic view of the CZI hydrogen sensor for the analysis of FLINAK. [194]. John Wiley & Sons. © 2017 The American Ceramic Society.

and milled into powders, which were then utilized for the tube formation process. The thin-shaped tubes were prepared through a hydrostatic pressing technique, followed by sintering at 1500 °C for 10 h. Finally, various electrodes were applied to the opposite surfaces of the tubes to complete the sensor cells, Au-Pd|SCY(SCN)|Pt. These sensors were used to analyze different water-containing gas mixtures at reduced temperatures (200 °C–400 °C). The two sensors demonstrated comparable behavior with slight discrepancies in operating temperatures (figure 8(a)), enabling precise analysis in moist air streams or in a combustion rig under conditions of excess air. Additionally, the tubular configuration of the sensor was found to exhibit superior performance compared with the planar design.

Ohshima *et al* [193] proposed $CaZr_{0.9}In_{0.1}O_{3-\delta}$ (CZI) as an electrolyte basis for a potentiometric Pt|CZI|Pt sensor. The U-tubes (closed at one end, 17 mm in length, and 0.8 mm in wall thickness) were produced by a ceramic hot pressure-casting machine. For this purpose, the synthesized CZI powder was mixed with paraffin wax, beeswax, and oleic acid under continuous stirring. After wax removal at a slow heating rate below 500 °C and pre-sintering at 1100 °C for 2 h, the CZI tubes were sintered at 1550 °C for 20 h in air to achieve a relative density of approximately 97% from the theoretical density (figure 8(b)). The fabricated CZI sensor demonstrated an excellent capacity to detect the hydrogen concentration in $H_2 + Ar$ gas mixtures. The performance was observed to be in close proximity to the Nernstian potential for an ideal protonic conductor. In addition, the sensor exhibited a rapid response time, with a duration of approximately 2 min following the stepwise change in the hydrogen partial pressure in the analyzed gas stream. The same electrolyte material was used as a sensor for analyzing the hydrogen concentration in FLINAK (LiF–NaF–KF molten salts, figure 8(c) [194]), but no details on tube fabrication were provided.

5.4. PCFCs

PCFCs are high-temperature fuel cells that efficiently convert energy into electricity. In conventional PCFCs fed by hydrogen, the hydrogen oxidation reaction occurs at the anode side (equation (4)), protons are electrochemically permeated through the dense electrolyte body, and the oxygen reduction reaction (a reverse reaction in equation (3)) takes place at the cathode side. To date, many PCFC-related reviews have been published; see [1], which discussed research activities from

2020–2024. While a significant proportion of these reviews address the chemical design aspects and functional properties of PCFC materials, the geometric design of these materials remains an understudied area.

An intensive investigation of tubular PCFCs was initiated in 2011, when a number of single cells were fabricated and characterized by different research groups [116–118, 132]. Although the power densities obtained at that time were relatively low (not exceeding 300 mW cm^{-2} at 600 °C for electrolytes of 20–25 μm in thickness), the experiments yielded some valuable insights into the manufacturing of the tubes. For example, Zhao *et al* [117] prepared NiO–BCZYYb anode supports by spinning and phase inversion methods, resulting in their sintering at different temperatures (1300, 1350, and 1400 °C). This variation was conducted to ascertain which temperature was the best in terms of the strength and porosity of the supports. The porosity of the NiO–BCZYYb hollow fiber tubes decreased from 45% to 33% with increasing sintering temperature. In contrast, the porosity of the reduced Ni–BCZYYb tubes was considerably greater, reaching 60% at 1300 °C and 51% at 1400 °C. Concurrently, the bending strength increased for both oxidized tubes (from 80 MPa at 1300 °C to 175 MPa at 1400 °C) and reduced tubes (from 50 MPa to 110 MPa). This suggests that a compromise between different microstructural and mechanical attributes is an inherent aspect of the material. Subsequently, several PCFCs were prepared using the same sintering temperatures to produce bilayer structures comprising a cermet and an electrolyte. Microstructural observations revealed that the electrolyte layer for PCFC co-sintered at 1300 °C was porous, thereby precluding electrochemical analysis of the cell. A comparison of the remaining two cells revealed that the highest power densities were achieved for the PCFC co-sintered at 1350 °C. The performance of the PCFC co-sintered at 1400 °C was significantly lower because of the higher ohmic resistance associated with relatively dense Ni-cermet conditions. The significance of cermet porosity was also noted by Min *et al* [152] when an alternative PCFC tube preparation method (extrusion) was employed.

Tong *et al* [168] investigated the impact of varying technological parameters on the functional and electrochemical characteristics of PCFCs fabricated by co-spinningco-spinning and co-sintering techniques. Specifically, the spinning flow rate and cermet powder content in the spinning suspension were adjusted to produce microstructurally qualitative multilayered cells. The optimal 20 μm-thick BCZY-based PCFC exhibited a power density of 550 mW cm^{-2} at 700 °C (figure 9(a)), which was 1.8 times greater than that of a cell with an unoptimized gas structure of hollow fiber supports. These findings indicate that the performance of PCFC is regulated not only by the ionic conductivity of the electrolyte layer and the electrochemical activity of the oxygen electrode but also by the microstructural features of the cermet supports, which should be highly porous and mechanically robust.

A further advance in the fabrication of PCFC tubes can be revealed upon a comparison of the same compositional system, Ni–BCZYYb|BCZYYb|LSCF–BCZYYb, which was widely studied between 2011 and 2021 [116, 122, 132, 135, 152, 157, 160]. The anode support tube membranes were prepared via a variety of techniques, including spinning with phase inversion [116], tape-casting with phase inversion [122], dip-coating [132, 135], extrusion [152], and slip-casting [157, 160]. The electrolyte layer was subsequently applied via the dip-coating technique and sintered (on a pre-sintered substrate) or co-sintered (with a green substrate) to yield the requisite half-cells. A composite comprising LSCF–BCZYYb as a counter electrode was subsequently deposited onto the electrolyte surface. This was achieved through the utilization of different techniques, including screen printing, brush painting, and dip coating. The maximal power densities of the fabricated PCFCs ranged from 100 to 530 mW cm^{-2} at 600 °C. These findings demonstrate that the optimal performance of a PCFC is contingent upon a multitude of technological variables. The highest electrode working area (2.3 cm^2) was achieved by Cao *et al* [135], enabling the generation of a total power output of 1.06 W for the Ni–BCZYYb|BCZYYb|LSCF–BCZYYb cell.

The LSCF–BCZYYb cathode is a classic composite consisting of a mixed ionic-electronic phase (LSCF) mixed with an electrolyte component (BCZYYb). However, other cathode compositions can also be used successfully. Zhu *et al* [155] performed a comparative analysis of three well-studied cathode compositions: $Ba_{0.5}Sr_{0.5}Co_{0.8}Fe_{0.2}O_{3-\delta}$ (BSCF [195]), $PrBa_{0.5}Sr_{0.5}Co_{1.5}Fe_{0.5}O_{6-\delta}$ (PBSCF [196]), and $BaCo_{0.4}Fe_{0.4}Zr_{0.1}Y_{0.1}O_{3-\delta}$ (BCFZY [197]). The corresponding tubular PCFCs with a 15 μm thick BCZYYb electrolyte and an active working area of 1.29 cm^2 were able to produce 517, 534, and 326 mW cm^{-2} at 600 °C, respectively (figure 9(b)). Interestingly, the lower ohmic resistance was associated with BSCF-based PCFC, whereas the lowest polarization resistance was found for the BCFZY-based cell; the PBSCF electrode presented the lowest electrochemical activity, resulting in the lowest PCFC performance.

Another advancement of this work [155] is based on the fact that not only single tubes but also a 2-cell tubular stack with an active working area of 8.2 cm^2 vs. 1.29 cm^2 were tested. This stack yielded a power of 2.3 W at 600 °C when dry hydrogen was used as a fuel (figure 9(c)). However, when comparing two types of PCFCs, the power densities of single cells with a smaller active working area were greater than those of cells with a larger active working area. In detail, the power density of the 2-cell tubular stack was about 280 mW cm^{-2}, which was actually lower than 517 mW cm^{-2} mentioned above. These same differences can also be found in other works. For example, Li *et al* [154] conducted a comparative analysis of two distinct PCFC designs, one with an area of 0.5 cm^2 and the other with an area of 15 cm^2 (figure 9(e)). The maximal power density of the button cell was 390 mW cm^{-2} at 600 °C, whereas the power density of the tubular cell with an extended working area was as low as 100 mW cm^{-2} at the same temperature. As illustrated by another example presented by Vourros *et al* [170], a brief PCFC tube with a surface area of 3 cm^2 yielded a power density of 375 mW cm^{-2} at 650 °C, which was two times greater than that of a tube with a surface area of 12.5 cm^2 (approximately 196 mW cm^{-2}). The aforementioned examples illustrate that cells with a highly active working

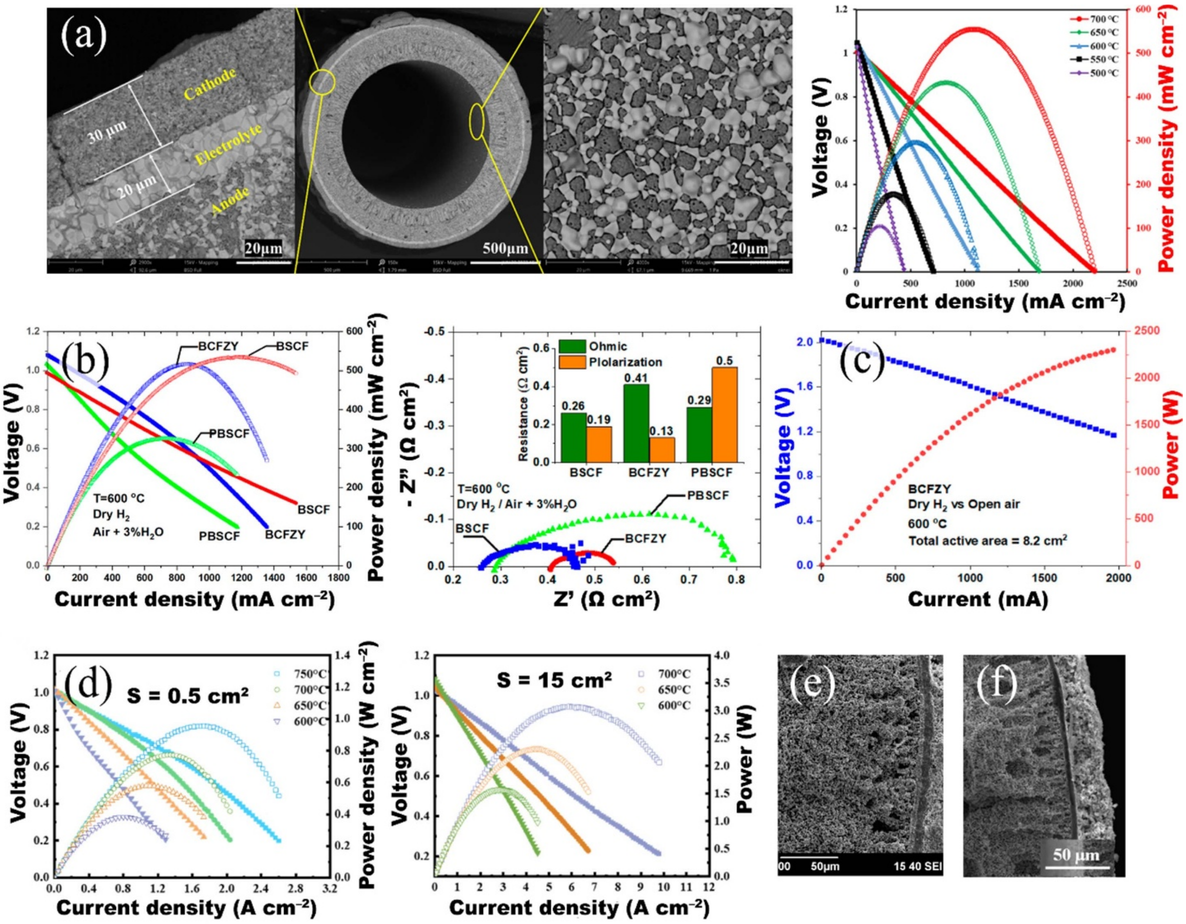

Figure 9. Selected results of tubular-type protonic ceramic fuel cells: (a) Microstructure and performance of the PCFC. Reproduced from [168]. CC BY 4.0. (b) PCFC performance with different electrode materials. Reprinted from [155], © 2021 Hydrogen Energy Publications LLC. Published by Elsevier Ltd All rights reserved. (c) IV and power characteristics of the 2-cell short tubular stack. Reprinted from [155], © 2021 Hydrogen Energy Publications LLC. Published by Elsevier Ltd All rights reserved. (d) Performance of PCFCs with small and high active working areas. Reprinted from [154], © 2021 Elsevier B.V. All rights reserved. (e) SEM image of bilayer SDC/BCZY electrolyte PCFC. Reprinted from [118], Copyright © 2011 Elsevier B.V. All rights reserved. (f) SEM image of bilayer BCZY/BZY electrolyte PCFC.[87]. John Wiley & Sons. © 2017 The American Ceramic Society.

area necessitate a meticulous organization of current collectors across the entirety of the inner and outer tube surfaces. In turn, this presents a significant technical challenge.

Importantly, not only single electrolyte layers but also bilayer electrolytes can be formed for tubular PCFCs. For example, in the work of Zhao *et al* [118], a 3 μm-thick BCZY electrolyte was employed as an electron-blocking layer between the cermet and the 10 μm-thick SDC layers (SDC = $Ce_{0.8}Sm_{0.2}O_{2-\delta}$), as shown in figure 9(e). This strategy permitted an increase in the open circuit voltage (OCV) from 0.72 V (for a BCZY-free cell) to 0.97 V at 700 °C. However, the power density of the bi-electrolyte PCFC was insufficient (below 250 mW cm^{-2} at 700 °C) because the ionic conductivity of BCZY was lower than that of SDC. This resulted in an increase in the ohmic-type resistance of the cells from 0.25 to 0.79 Ω cm^2 at the same comparison temperature. In another study, He *et al* [120] proposed the implementation of two electrolyte layers, namely, BCZY and $BaZr_{0.8}Y_{0.2}O_{3-\delta}$ (BZY), for a tubular PCFC, figure 9(f). The cell was fabricated via a spinning process followed by phase inversion techniques, while the electrolyte layers were formed through coating. The rationale behind the choice of BZY was its superior chemical stability in comparison to that of BCZY, a finding that was corroborated through experimental analysis. The output performance of the developed PCFC was also relatively low (~180 mW cm^{-2} at 700 °C), largely attributed to the presence of notable ohmic and polarization resistance values (0.70 and 0.71 Ω cm^2, respectively).

Table 3 lists the main electrochemical data obtained for a wide range of tubular PCFCs fabricated and tested in the literature. The fabrication techniques allow for a considerable degree of variability in terms of material composition, electrolyte thickness (ranging from 6 to 40 μm), and active working area (extending from 0.2 to 15 cm^2). Despite these advancements, the power densities of tubular PCFCs frequently remain lower than those of their planar-design counterparts; the latter have the potential to achieve power densities of up to 1–1.5 W cm^{-2} at 600 °C, but for small cells. As shown above,

Table 3. Output parameters of tubular PCFCs depending on their manufacturing methods: h is the electrolyte thickness, s is the effective working area, OCV is the open-circuit voltage, R_{ohm} and R_{p} are the ohmic and polarization resistances measured at the OCV, respectively, and $P_{\max}$ is the maximal power density. Abbreviations: PI—phase inversion, S—spinning, DC—dip-coating, SP—screen printing, BP—brush painting, SC—slip casting, E—extrusion, SPR—spraying, VSC—vacuum slurry coating, 3DP—3D printing, USSC—ultrasonic spray coating.

Electrolyte[a]	h (μm)	Fuel electrode substrate[b]	Air electrode[c]	Manufacturing methods	s (cm^2)	OCV (V)			R_{ohm} (Ohm cm^2)			R_{p} (Ohm cm^2)			$P_{\max}$ (W cm^{-2})			References
						500 °C	600 °C	700 °C	500 °C	600 °C	700 °C	500 °C	600 °C	700 °C	500 °C	600 °C	700 °C	
BCZYYb	25	NiO–BCZYYb	LSCF–BCZYYb	PI, S, DC, SP	0.65	1.05	1.01	—	1.08	0.71	—	0.35	6.41	—	0.08	0.26	—	[116]
BCZYYb	20	NiO–BCZYYb	SSC–BCZYYb	PI, S, DC, SP	—	—	1.04	—	—	1.21	—	—	0.51	—	—	0.15	—	[117]
BCZY–BZY	8	NiO–BCZY	LSCF–BZY	PI, DC, BP	0.3	—	1.01	0.98	—	1.31	0.70	—	0.71	2.33	—	0.07	0.18	[120]
BCZYYb	20	NiO–BCZYYb	LSCF–BCZYYb	PI, SC, DC, BP	0.33	—	1.00	—	—	0.41	—	—	0.37	—	—	0.34	—	[122]
BCTb	15	NiO–BCTb	Ag	PI, S, DC, BP	—	0.99	0.92	0.89	0.45	0.30	0.26	3.30	0.78	0.15	0.10	0.21	0.55	[123]
BCZYYb	12	NiO–BCZYYb	LSCF–SDC	PI, DC, SP	2	—	0.98	0.94	—	0.31	0.18	—	0.26	0.05	—	0.70	0.97	[126]
BCZY	10	NiO–BCZY	BCFZY–BCZY	PI, co-S, BP	—	—	—	1.01	—	—	—	—	—	—	—	—	0.31	[129]
BCZY	21	NiO–BCZY	BCFZY–BCZY	PI, co-S, BP	—	1.05	1.03	1.02	0.87	0.64	0.50	2.28	0.28	0.04	0.10	0.30	0.55	[129]
BCZY	30	NiO–BCZY	BCFZY–BCZY	PI, co-S, BP	—	—	—	1.04	—	—	—	—	—	—	—	—	0.50	[129]
BCZY	41	NiO–BCZY	BCFZY–BCZY	PI, co-S, BP	—	—	—	1.05	—	—	—	—	—	—	—	—	0.44	[129]
BCZYYb	30	NiO–BCZYYb	LSCF	PI, E, DC, SP	0.6	—	1.06	1.02	—	1.61	0.81	—	2.21	0.20	—	0.08	0.23	[130]
BCZY	20	NiO–BCZY	BCFZY–BCZY	PI, co-S, BP	0.43	1.08	1.04	1.00	3.14	0.26	0.04	1.00	0.58	0.39	0.08	0.29	0.60	[131]
BCZY	20	NiO–BCZY	BCFZY–BCZY	PI, co-S, BP	12.04	1.08	1.04	1.00	—	—	—	—	—	—	0.08	0.16	0.21	[131]
BCZYYb	12	NiO–BCZYYb	LSCF–BCZYYb	DC, BP	1	—	1.02	0.99	—	0.32	0.15	—	0.29	0.08	—	0.53	0.81	[132]
BCZYYb	12	NiO–BCZYYb	LSM–SDC	PI, DC, SP	2	—	0.95	0.93	—	0.39	0.17	—	0.21	0.04	—	0.58	0.89	[133]
BCZYYb	12	NiO–BCZYYb	LSCF	PI, DC, SP	1	—	1.00	0.97	—	0.37	0.16	—	0.34	0.06	—	0.59	0.90	[134]
BCZY	25	NiO–BCZY	LSCF	DC, BP	2.3	1.10	1.08	—	—	0.39	—	—	0.22	—	0.19	0.46	—	[135]
BCZYYb	8	Fe_2O_3/NiO–BCZYYb	PBSCF	PI, DC, BP	—	—	1.07	1.00	—	0.16	0.09	—	0.22	0.03	—	0.77	1.50	[137]
BCZYYb	8	NiO–BCZYYb	PBSCF	PI, DC, BP	—	—	1.06	0.99	—	0.20	0.11	—	0.31	0.04	—	0.65	1.43	[137]
BCZYYb	7	Fe-CeO_x/NiO–BCZYYb	PBSCF	PI, DC, BP	—	—	—	0.99	—	—	—	—	—	0.04	—	—	1.33	[138]
BCZYYb	6	NiO–BCZYYb	PBSCF	PI, DC, BP	0.24	—	1.06	1.00	—	0.13	0.08	—	0.15	0.02	—	1.07	2.33	[139]
BCZYYb	6	SFMC/NiO–BCZYYb	PBSCF	PI, DC, BP	0.24	—	1.06	1.00	—	0.14	0.07	—	0.13	0.02	—	1.19	2.43	[139]
BCZYYb	6	NiO–BCZYYb	PBSCF	PI, DC, BP	0.24	—	1.07	1.01	—	0.10	0.06	—	0.17	0.02	—	0.91	2.62	[140]
BZCY72	20	NiO–BZCY72	LSCF	E, SPR, SP	7.5	—	—	0.93	—	—	—	—	—	—	—	—	0.07	[142]
BCZY	10	NiO–BCZY	LSCF–BCZY	E, DC, VSC	2.07	—	1.07	1.01	—	0.99	0.78	—	0.05	0.03	—	0.31	0.50	[152]
BCZYYb	20	NiO–BCZYYb	PNOF–BCZYYb	E, DC, BP	15	—	1.08	1.02	—	—	—	—	—	—	—	0.10	0.20	[154]
BCZYYb	15	NiO–BCZYYb	BCFZY	E, BP	1.29	1.13	1.08	—	—	0.41	—	—	0.13	—	0.16	0.52	—	[155]
BCZYYb	15	NiO–BCZYYb	BSCF	E, BP	1.29	1.02	0.99	—	—	0.26	—	—	0.19	—	0.14	0.54	—	[155]
BCZYYb	15	NiO–BCZYYb	PBSCF	E, BP	1.29	—	1.03	—	—	0.29	—	—	0.50	—	—	0.33	—	[155]
BCZYYb	15	NiO–BCZYYb	BCFZY	E, BP	8.24	—	1.00	—	—	—	—	—	—	—	—	0.28	—	[155]

(Continued.)

Table 3. (Continued.)

BCZYYb	25	NiO–BCZYYb	LSCF–BCZYYb	SC, DC	2	—	1.06	1.04	—	0.50	0.59	—	0.10	0.35	—	0.33	0.42	[157]
BSCZGY	10	NiO–YSZ	LSCF–BSCZGY	SC, DC	1.79	—	1.14	1.12	—	0.41	0.19	—	3.47	1.81	—	0.17	0.43	[158]
BCZYYb	20	NiO	LSCF–BCZYYb	SC, DC	1.60	—	0.94	0.88	—	0.67	0.51	—	2.22	0.35	—	0.10	0.18	[159]
BCZYYb	20	NiO–YSZ	LSCF–BCZYYb	SC, DC	1.60	—	1.08	1.02	—	0.79	0.49	—	1.00	0.19	—	0.11	0.19	[159]
BCZYYb	10	NiO	LSCF–BCZYYb	SC, DC	1.60	—	0.94	0.88	—	0.66	0.50	—	2.23	0.37	—	0.10	0.18	[160]
BCZYYb	17	NiO–YSZ	LSCF–BCZYYb	SC, DC	1.60	—	1.08	1.02	—	0.79	0.50	—	1.01	0.22	—	0.11	0.18	[160]
BZCYZ	25	NiO–BZCYZ	LSCF–BZCYZ	SC, DC, BP	—	—	1.01	0.96	—	1.58	1.50	—	0.85	0.15	—	0.15	0.19	[161]
BZCY72	12	NiO–BZCY72	BCFZY	3DP	3	1.13	1.07	—	1.37	0.84	—	0.36	0.09	—	0.16	0.28	—	[170]
BCZYYb	10	NiO–YSZ	LSCF–BCZYYb	SC, DC	2	—	1.06	0.96	—	0.82	0.52	—	1.35	0.24	—	0.17	0.29	[197]
BCZYYb1	8	NiO–BCZYYb0	BCFZY–BCZYYb	E, USSC, BP	0.45	—	1.04	—	—	0.39	—	—	0.20	—	—	0.42	—	[198]
BCZYYb2	8	NiO–BCZYYb0	BCFZY–BCZYYb	E, USSC, BP	0.45	—	1.06	1.01	—	0.29	—	—	0.15	—	—	0.48	0.70	[198]
BCZYYb3	8	NiO–BCZYYb0	BCFZY–BCZYYb	E, USSC, BP	0.45	—	1.02	—	—	0.55	—	—	0.32	—	—	0.36	—	[198]

[a] BCZYYb = $BaCe_{0.7}Zr_{0.1}Y_{0.1}Yb_{0.1}O_{3-\delta}$, BCZY = $BaCe_{0.7}Zr_{0.1}Y_{0.2}O_{3-\delta}$, BZY = $BaZr_{0.8}Y_{0.2}O_{3-\delta}$, BCTb = $BaCe_{0.95}Tb_{0.05}O_{3-\delta}$, BZCY72 = $BaZr_{0.7}Ce_{0.2}Y_{0.1}O_{3-\delta}$, BSCZGY = $Ba_{0.5}Sr_{0.5}Ce_{0.6}Zr_{0.2}Gd_{0.1}Y_{0.1}O_{3-\delta}$, BZCYZ = $BaZr_{0.4}Ce_{0.4}Y_{0.15}Zn_{0.05}O_{3-\delta}$, BCZYYb1 = $Ba_{1.1}Zr_{0.4}Ce_{0.4}Y_{0.1}Yb_{0.1}O_{3-\delta}$, BCZYYb2 = $Ba_{1.2}Zr_{0.4}Ce_{0.4}Y_{0.1}Yb_{0.1}O_{3-\delta}$, BCZYYb3 = $Ba_{1.3}Zr_{0.4}Ce_{0.4}Y_{0.1}Yb_{0.1}O_{3-\delta}$.

[b] SFMC = $Sr_2Fe_{1.35}Mo_{0.45}Cu_{0.2}O_{6-\delta}$, YSZ = $Y_{0.08}Zr_{0.92}O_{2-\delta}$, BCZYYb0 = $BaZr_{0.4}Ce_{0.4}Y_{0.1}Yb_{0.1}O_{3-\delta}$.

[c] LSCF = $La_{0.6}Sr_{0.4}Co_{0.2}Fe_{0.8}O_{3-\delta}$, SSC = $Sm_{0.5}Sr_{0.5}CoO_{3-\delta}$, SDC = $Sm_{0.2}Ce_{0.8}O_{2-\delta}$, BCFZY = $BaCo_{0.4}Fe_{0.4}Zr_{0.1}Y_{0.1}O_{3-\delta}$, LSM = $La_{0.75}Sr_{0.25}MnO_{3-\delta}$, PBSCF = $PrBa_{0.5}Sr_{0.5}Co_{1.5}Fe_{0.5}O_{6-\delta}$, PNOF = $Pr_2NiO_{3.9+\delta}F_{0.1}$, BSCF = $Ba_{0.5}Sr_{0.5}Co_{0.8}Fe_{0.2}O_{3-\delta}$, LSC = $La_{0.6}Sr_{0.4}CoO_{3-\delta}$.

increasing the electrode working area results in a decrease in the SOFC power density; this regularity is associated with losses due to the extended current paths.

To evaluate the effects of different parameters on the performance of the target PCFC (power density and overall power), a series of graphs were plotted on the basis of table 3 and are presented in figure 10. A discussion of the power density of PCFCs reveals that its value increases in proportion to the thickness of the electrolyte, as illustrated in figure 10(a). This phenomenon can be explained by the well-known equation (10), which indicates that the ohmic-type resistance of PCFCs decreases as the electrolyte thickness decreases (assuming that the electrolyte conductivity of the same material remains constant). Consequently, thin-film technologies are of paramount importance for the development of high-performance PCFCs. However, the analysis of power density values depending on the thin film conductivity (figure 10(b)) indicates that the conductivity of the same (BCZYYb, BCZY) or little derived electrolytes is not constant and varies within a range of 1 order of magnitude. This variation in the transport properties of electrolytes under seemingly similar conditions was thoroughly discussed in our previous review devoted to Y- and Yb–codoped Ba(Ce,Zr)O_3 [7]. Briefly, the thin-film conductivity of electrolytes depends not only on their inherent properties (crystal structure, defect disordering, microstructure) but also on the electrode/electrolyte interface quality; the latter may cause a high ohmic-type resistance due to insufficient chemical or mechanical compatibility between functional materials.

However, the analysis of power density values in relation to thin film conductivity (figure 10(b)) indicates that the conductivity of electrolytes with the same (BCZYYb, BCZY) or similar chemical composition is not constant and varies by approximately one order of magnitude. This variation in the transport properties of electrolytes under seemingly similar conditions was thoroughly discussed in our previous review aimed at Y- and Yb- co-doped Ba(Ce,Zr)O_3 [7]. In summary, the thin-film conductivity of electrolytes is influenced not only by their intrinsic properties (crystal structure, defect disordering, microstructure) but also by the quality of the electrode/electrolyte interface. This interface can result in the appearance of a high ohmic-type resistance due to inadequate chemical or mechanical compatibility between functional materials. As a result, the apparent ohmic resistance becomes the sum of the real ohmic resistance of the electrolyte layer and the ohmic resistance of the electrode/electrolyte interface(s). This explains the high data scatter observed in figure 10(b)

$$\sigma = \frac{h}{R_{\mathrm{ohm}}}. \tag{10}$$

A comparison of the electrochemical activities of the electrolyte and electrode materials at 600 °C (figure 10(c)) revealed that there was no clear relationship between them and the power density. This means that either the ohmic resistance or the polarization resistance can affect the performance of tubular PCFCs. Moreover, an increase in power density is observed as the total PCFC resistance ($R_{\mathrm{total}} = R_{\mathrm{ohm}} + R_{\mathrm{p}}$) decreases (figure 10(d)), confirming the predicted relationship expressed by the following equation (when a maximal power density is observed at half of the OCV value):

$$P_{\max} = \frac{\mathrm{OCV}^2}{4R_{\mathrm{total}}}. \tag{11}$$

When the PCFC power density is normalized by the effective working area of the tubes ($P_{\mathrm{total}} = P_{\max}{\cdot}s$), the corresponding functional relationships can be obtained, as shown in figures 10(e)–(h). However, almost all of them show no clear regularity as a function of electrolyte thickness, electrolyte conductivity, and ohmic contribution; only a trend of $P_{\mathrm{total}} \sim (R_{\mathrm{total}})^{-1}$ is still observed. These experimental results can again be explained by the complex character of scaling when the power (or power density) is reduced for a larger working area of electrochemical cells. As a result, attaining 1 W cm^{-2} for PCFCs with active working areas of 0.2, 2, and 20 cm^2 represents a significant challenge at disparate levels.

5.5. *PCECs*

PCECs are electrochemical systems that facilitate the conversion of electrical energy applied to the cell into chemical energy through the splitting (electrolysis) of certain compounds into substances with high internal energy. In the conventional steam electrolysis process, the reactions described by equations (3) and (5) occur on the opposite side of PCECs. The field of water electrolysis in PCFCs has been extensively studied, with trends and advances presented in numerous review articles [199–204]. However, the majority of available reports pertain to planar-type PCECs, while the fabrication and characterization of tubular PCECs have been limited by several studies. These works are briefly discussed in the present subsection.

In 2019, Vøllestad *et al* [146] reported the successful fabrication and characterization of a PCEC tube with an active working area of 10 cm^2. The tube was prepared by extruding a NiO–BZCY support, followed by spray coating a BZCE electrolyte and brush painting either a BGLC or a BGLC–BZCY anode (BGLC = $BaGd_{0.8}La_{0.2}Co_2O_{6-\delta}$). The use of a composite anode instead of a single-phase anode markedly increased the Faradaic efficiency of PCFCs, whereas their volt-ampere dependences remained almost the same. The most effective cell was capable of producing up to 15 ml min^{-1} of hydrogen at 600 °C, exhibiting stable performance for over 700 h (figure 11(a)). Additionally, the fabricated tubes demonstrated mechanical flexibility, the capacity to withstand elevated pressures, enhanced process integration, and scalability for large-scale applications.

In the work of Medvedev *et al* [165], a tubular PCEC was fabricated via the tape-calendar method via a $Pr_{1.95}Ba_{0.05}NiO_{4+\delta}$ steam electrode. This fabrication technique allowed an active working area of 4.6 cm^2 to be achieved. The main focus of this work was to identify the rate-limiting steps of the steam electrolysis process at different overpotentials via electrochemical impedance analysis and relaxation time distribution, figure 11(b). The excellent

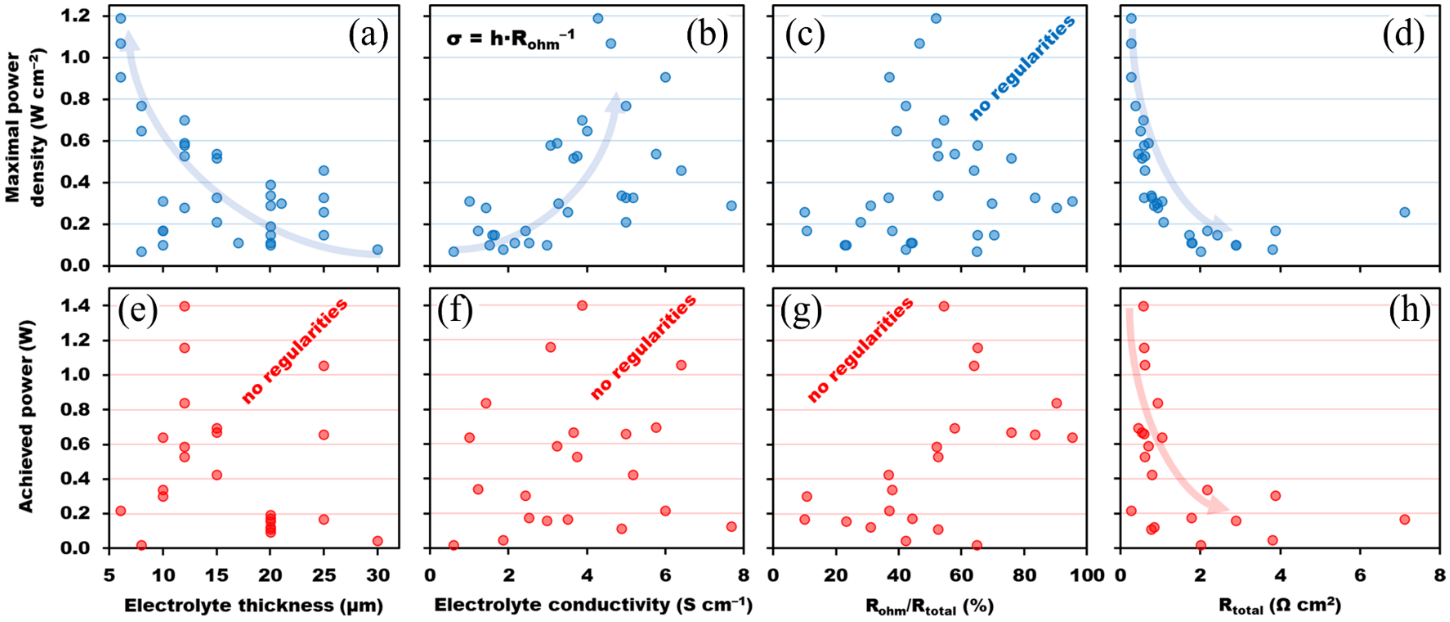

Figure 10. The maximal power density and overall power of tubular PCFCs at 600 °C depending on different parameters, including the electrolyte thickness, electrolyte conductivity, contribution of the ohmic resistance to the total resistance, and total resistance of the cells. The three last parameters were determined under the OCV mode (see table 3).

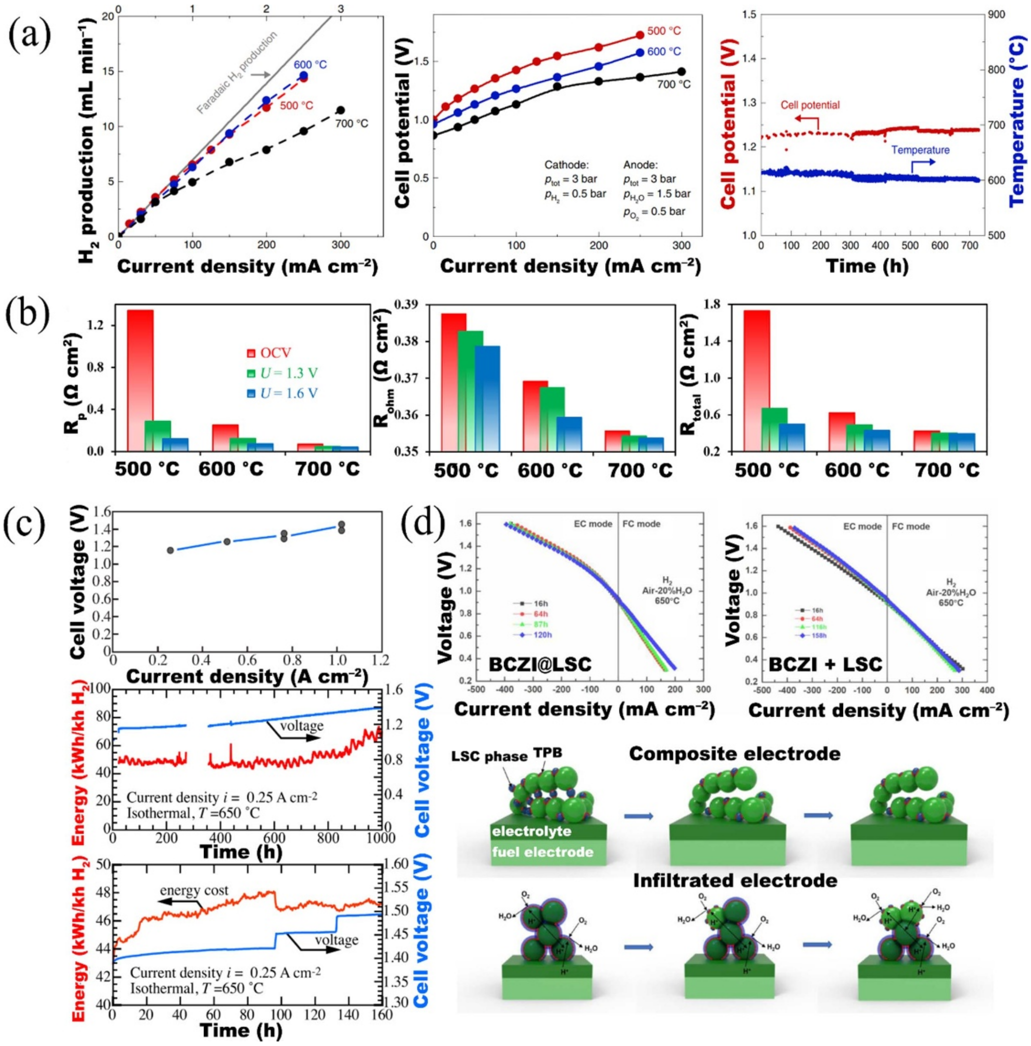

Figure 11. Selected results of tubular-type protonic ceramic electrolysis cells: (a) volt−ampere dependences of 10 cm^2 PCFCs at different temperatures and their long-term operation at 600 °C with a current density of 62.5 mA cm^{-2}. Reproduced from [146], with permission from Springer Nature. (b) polarization, ohmic, and total resistances of the PCEC depending on the operating conditions. Reprinted from [165], © 2016 Elsevier Ltd All rights reserved; (c) volt-ampere and long-term characteristics of the large-area PCFC tubes. Reproduced from [156]. © 2022 The Electrochemical Society ("ECS"). Published on behalf of ECS by IOP Publishing Limited. All rights reserved; (d) *I–V* curves of the PCFCs as a function of time in reversible FC-EC operational mode for the BCZI + LSC and BCZI@LSC electrodes along with the proposed scheme of their long-term degradation. Reproduced from [168]. CC BY 4.0.

integrity and performance of the PCEC were determined by a rational choice of the functional materials used. As a result, hydrogen flux values of 12, 19, and 25 ml min^{-1} were achieved at 500, 600, and 700 °C, respectively. A comparable oxygen (steam) electrode was proposed by Li *et al* [154], which employed pure and F-containing $Pr_2NiO_{4+\delta}$ complex oxides. The fluorination of complex oxides is a well-known chemical modification approach resulting in a notable increase in their oxygen transport properties [205]. Consequently, the PCEC based on F-containing $Pr_2NiO_{4+\delta}$ exhibited higher current densities than did the original $Pr_2NiO_{4+\delta}$ electrode, namely, 2.0 vs. 1.2 A cm^{-2} at 650 °C. These current densities were markedly higher than those reported in two previous studies. However, notably, the studied PCECs exhibited a very low active working area of only 0.5 cm^2.

In a recent study, Kee *et al* [156] fabricated and tested PCEC-extruded tubes with one of the largest active areas, reaching a surface area exceeding 30 cm^2. The tubes included a BCZY electrolyte layer with a thickness of 25 μm and the classical LSCF–BCZY anode, which was discussed in section 5.4. The electrochemical characterization of the large-area tubes demonstrated their capacity to produce ∼85 ml min^{-1} hydrogen at 600 °C and 1.33 V, with an active working area of 40.7 cm^2 (figure 11(c)). This value is equivalent to a hydrogen flux of 2.1 ml min^{-1} cm^{-2}. In addition to the aforementioned characterization, a number of issues related to thermal management, economics, energy efficiency, and stack-scale perspectives were also considered.

In a recent study, Mu *et al* [168] shed light on the long-term durability of 7.5 cm^2 PCECs with two distinct oxygen electrodes: a mechanical mixture of BCZI/LSC and a BCZI backbone infiltrated with LSC, BCZI@LSC (where BCZI = $BaCe_{0.5}Zr_{0.4}In_{0.1}O_{3-\delta}$, LSC = $La_{0.6}Sr_{0.4}CoO_{3-\delta}$). The electrolysis current densities of these cells at 650 °C were 165 and 250 mA cm^{-2}, respectively. This finding indicates that the infiltrated electrode exhibited significantly greater electrochemical activity than that of the conventionally prepared electrodes. The long-term and cycle stability of the fabricated PCECs (figure 11(d)) yielded interesting results, as a notable decline in performance was observed in the cell comprising the mechanically mixed composite electrode. A source of this degradation was proposed to be the thermal incompatibility of the functional components, resulting in electrode delamination, particularly during thermal cycles. Conversely, the electrolyte/electrode interface was robust and stable in the case of the infiltrated electrode, ensuring strong contact between the adjusted functional layers. From a microstructural perspective, the infiltrated electrode also exhibited slight degradation, but it still provided sufficient active zones for electrochemical reactions.

5.6. Protonic ceramic electrochemical reactors (PCERs)/converters

PCERs (converters) are solid oxide cells that provide various hydrogenation/dehydrogenation reactions when current is applied to such cells (figure 12(a)). The operating principle of these devices is analogous to that of hydrogen pumps or PCECs since the applied current initiates the pumping out of hydrogen from a hydrogen-containing gas (or gas mixture), initiating the dehydrogenation process (see equations (3) and (4)). On the opposite side of such reactors, the hydrogenation process takes place, allowing either hydrogen production (PCECs, see section 5.5) or partial/complete reduction of oxidized substances (some examples are given by equations (6)–(9)). The great variability of electrochemical conversions allows PCERs to be used for a variety of purposes, including the high-temperature conversion of C- and N-containing compounds [4, 5, 173, 199]. As a result, a number of studies devoted to PCERs are currently outnumbering those aimed at simple hydrogen production in PCECs. This also applies to tubular-type protonic ceramic electrochemical cells.

Kyriakou *et al* [144] proposed a Ni–BZCY|BZCY|Cu tubular membrane reactor for realizing a methane steam reforming process at 450 °C–650 °C. This tube, with a length of 20 cm, a diameter of 1 cm, an electrolyte thickness of 30 μm, and an active electrode area of 20 cm2, was prepared by CoorsTek Inc. via a combination of slip casting, dip coating, and brush painting techniques. A reactant gas (wet CH_4/N_2) was supplied to the anode side, and the concentration of products in the anode chamber exhaust stream was analyzed via the chromatographic method. Under such operational conditions, the following electrochemical reaction occurred at the anode side:

$$CH_4 + H_2O \rightarrow CO_2 + 8H^+ + 8e'. \tag{12}$$

At the same time, hydrogen formation (equation (5)) occurred at the opposite electrode. The electrochemical characterization of the fabricated reactor was conducted under a variety of conditions, including various temperatures (from 450 to 650 °C), total flow rates (from 15 to 120 ml min^{-1}), steam-to-carbon ratios (from 0.5 to 4), and cell potentials (from OCV to 2.4 V). In accordance with the best conditions, a CH_4 conversion of 80% and CO_2 selectivity of 95% were achieved, along with excellent chemical stability, durability, and coke tolerance in a 24 h short-term test.

The same combination of fabrication techniques was utilized by Xiao *et al* [161]. An electrochemical reactor was designed from the following functional materials: Ni–BZCYZ|BZCYZ|LSCF–BZCYZ (BZCYZ = $BaZr_{0.4}Ce_{0.4}Y_{0.15}Zn_{0.05}O_{3-\delta}$). However, no tube dimensions were indicated, with the exception of the electrolyte thickness (25 μm). The tube was initially evaluated as a PCFC in conventional air/H_2 mode; its corresponding performance can be found in table 3. Then, the electrolysis mode was subjected to analysis when 3% H2O/air was supplied at the oxygen electrode side, while x% CO_2/H_2 gas mixtures (with $0 \leqslant x$, vol.% $\leqslant 50$) were supplied at the fuel electrode side. Their findings indicated that an elevated CO_2 concentration at the cathode resulted in a notable reduction in current density, from 505 to 335 mA cm^{-2} at 650 °C and 1.4 V. The authors posited that this outcome was attributable to a reduced number of active sites resulting from Ni-to-NiO oxidation in CO_2-rich atmospheres. However, this explanation is arguably ambiguous, given that all the $x\%CO_2/H_2$ gas mixtures are classified as highly reducing atmospheres in terms of the equilibrium oxygen partial pressure. Conversely, the observed findings align with a well-established phenomenon related to the slower kinetics of CO_2 reduction than of hydrogen formation. To support their statement, the conversion parameters should be analyzed, including CO_2 conversion, production rate or selectivity of CO and CH_4. A similar simple analysis was performed in the work of [208] for analogous cell and experimental conditions.

A significant breakthrough was achieved by Clark *et al* [206], who fabricated a PCER stack with an active electrode area of 36 × 15 cm^2 for the production of hydrogen from ammonia, methane, and biogas. To achieve this objective, single BZCY-based tubes, which were prepared via the extrusion technique, were collected in a stack comprising 36 cells. This was done with great care in terms of the organization of the sealing and current collectors. As illustrated in figure 12(b), the individual cells and the assembled stack were evaluated under a range of operational conditions, with a particular emphasis on the ability to perform electrochemical conversion under elevated pressures, reaching 30 bars. The 36-cell PCER stack demonstrated the capacity to achieve near-complete CH_4 conversion and high H_2 recovery from both CH_4 and biogas. Additionally, it facilitated a complete equilibrium shift and a CO_2-rich effluent stream, which facilitated facile carbon capture. In addition, the single PCER cells exhibited nearly complete NH_3 conversion, resulting in an effluent stream that was virtually free of residual NH_3. The subsequent

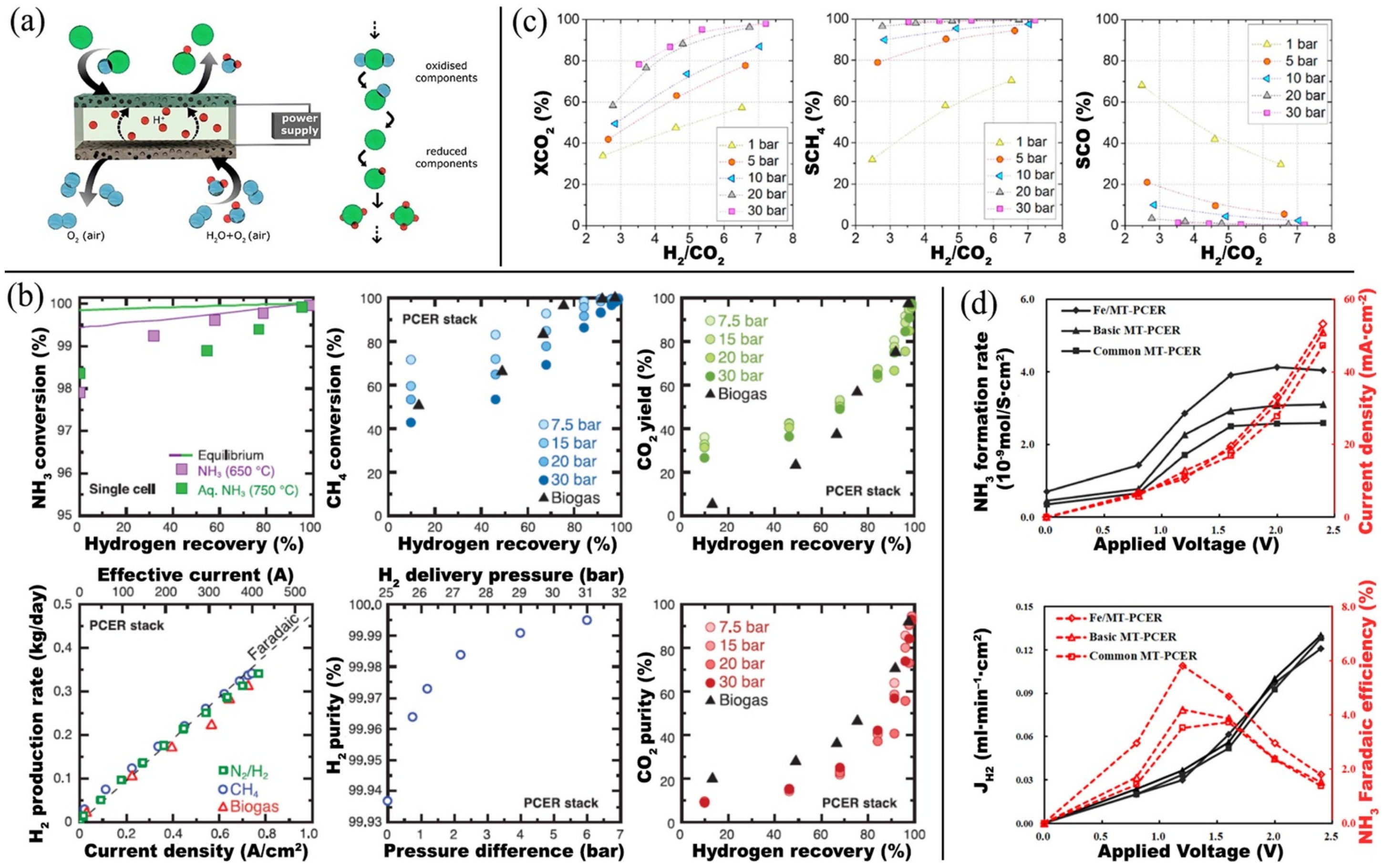

Figure 12. Selected results of tubular-type protonic ceramic electrochemical reactors: (a) Principal schema of combined electrolysis and conversion processes in PCECs. Reprinted from [199], © 2019 Hydrogen Energy Publications LLC. Published by Elsevier Ltd All rights reserved. (b) PCER single-cell and stack performances in NH_3 and $CH_4 + H_2O$ conversion. From [206]. Reprinted with permission from AAAS. (c) PCER performance in CO_2 electrochemical conversion and different experimental conditions. Reproduced with permission from [149]. © 2023 The Authors. Published by Elsevier Inc. CC BY-NC-ND 4.0; (d) parameters of ammonia synthesis in microtubular PCERs depending on the reactor design and applied voltages. Reprinted from [207], © 2024 Hydrogen Energy Publications LLC. Published by Elsevier Ltd All rights reserved.

work of the same author [149] was directed towards the direct electrocatalytic reduction of CO_2 in the PCER of a comparable design (see equation (6) and (7)). The methanation yield was significantly affected by the total pressure and the H_2/CO_2 ratio (figure 12(c)). The pressurization of the cell resulted in a notable increase in the CH_4 yield, reaching values of 80% at 20 bars at a stoichiometric H_2/CO_2 ratio of 4, which is in accordance with the thermodynamic equilibrium yield. To further increase the methanation yield, the in situ extraction of water was mimicked by feeding CO instead of CO_2; this resulted in CH_4 yield values that approached almost 100%. In addition to the catalytic parameters, the electrochemical characterization of cell operation was also conducted via a combination of EIS and DRT analyses. This approach facilitates the detailed examination of electrode processes as a function of temperature, pressure, and current density parameters. Additional details on CO_2 hydrogenation in PCERs can be found in the recent works of Ruiz *et al* [150], Li *et al* [209], and Miao *et al* [210].

Recently, Li *et al* [207] proposed a PCER for ammonia production at atmospheric pressure (see equation (9)). Although ammonia synthesis has been recently reported for button-type protonic ceramic electrochemical cells [211–214], this work addresses microtubularly designed PCERs of the Ni–BCZY|BCZY|Ag and Fe@Ni–BCZY|BCZY|Ag configurations. These tubes had an active electrode area of 2.2 cm^2 and an electrolyte thickness of 130 μm. At 580 °C and an applied voltage of 2 V, the maximum NH_3 formation rate was increased from $3.0 \cdot 10^{-9}$ mol cm^{-2} s^{-1} to $4.1 \cdot 10^{-9}$ mol cm^{-2} s^{-1} by coating the inner surface of the basic PCER with an additional Fe catalyst. However, most of the protons transferred from the anode to the cathode were found to participate in the hydrogen evolution reaction rather than ammonia synthesis, resulting in low NH_3 faradaic efficiency (figure 12(d)). The authors reported that the activity of the cathode catalyst remained a limiting factor for NH_3 synthesis. Consequently, the development of highly active electrocatalysts is essential to further enhance the PCER performance in the NH_3 synthesis process.

5.7. Other types of protonic ceramic electrochemical cells

In addition to the discussion of electrochemical cells, proton-conducting electrolytes can be utilized in a number of other types, which have recently garnered increasing attention. One such type is a family of reversible protonic ceramic electrochemical cells that permit the simultaneous conversion and storage of energy [215–219]. The reversible derivatives can be regarded as a straightforward combination of fuel cell and electrolysis cell modes. However, in many cases, both the anode and cathode gases are humidified in a strategic manner to ensure optimal performance and efficiency in both modes. Conversely, conventional PCFCs are typically operated in a wet H_2/air gradient, which is unsuitable for electrolysis applications. Another family of protonic ceramic electrochemical cells comprises those designated symmetrical (or quasisymmetrical) cells, which are composed of an anode and a cathode layer with an almost identical composition [220–223]. This approach enables a reduction in the number of functional materials and technological steps required for the fabrication of multilayer cells. However, to date, the most promising results have been achieved for gallate-based symmetrical cells, which are based on the electrolyte-supported configuration. The research and development of symmetrically designed protonic ceramic cells is in its infancy.

6. Computational research of tubular protonic ceramic electrochemical cells

The advancement of high-performance and highly efficient solid oxide electrochemical cells based on proton-conducting electrolytes is challenging to achieve without the utilization of empirical and computational models. These models offer a valuable means of predicting the output performance of electrochemical devices and determining their suitable operating conditions. Among the literature, only a few studies have addressed the modeling of tubular cells.

Thermofluid dynamics (TFD) modeling is an important stage in the design of electrochemical devices. Using TFD modeling, the effects of gas flow, gas diffusion, electrochemistry, and heat transport on various characteristics of electrochemical devices can be evaluated. Catalan-Martinez *et al* [224] developed a computational fluid dynamics model for a modular tubular PCEC. The proposed model is discussed in terms of its potential for efficient generation of pressurized dry hydrogen under different conditions. A parametric model was created to simulate the internal and external chamber pressures and inlet flow temperature under two adiabatic operation scenarios with different vapor conversion rates. The model showed that a low steam conversion ratio enables PCEC operation at a relatively high current density, whereas the thermoneutral voltage (TNV) at a fixed steam conversion ratio is highly sensitive to external parameters and operating modes. Increasing the pressure of generated hydrogen results in a reduction in the hydrogen production rate in the TNV mode. However, this can be offset by increasing the vapor pressure or decreasing the inlet gas flow temperature. Furthermore, the incorporation of a porous working medium as a current collector in the vapor chamber of the PCEC can enhance heat transfer in this chamber. The area-specific resistance of the PCEC determines the current density, necessitating the adaptation of the PCEC active area to achieve the required hydrogen production and energy efficiency.

TM modeling is an integral part of electrochemical device design. When a device is subjected to elevated temperatures, mechanical stresses emerge, which can potentially result in destruction of the cell. This phenomenon is attributed to the disparity in the thermal expansion coefficients of the functional materials. In addition to thermal expansion, chemical expansion also plays a role, as observed in proton-conducting materials within humid atmospheres. TM modeling offers a valuable tool for identifying the conditions that guarantee device reliability under cyclic temperature fluctuations. Li *et al* [225] carried out a TM analysis for a 2D tubular PCEC. The impact of structural and operational parameters on the mechanical behavior of the cell was investigated. In addition, a predictive model for parameters such as the mechanical stress, Faraday efficiency, and operating stress was established on the basis of the obtained data. The results demonstrate that chemical expansion is predominantly influenced by the cathode porosity and electrolyte thickness, whereas the overall mechanical stress level is affected primarily by the cathode porosity, current density, and operating temperature. Overall, this work underscores the necessity of incorporating chemical expansion information into the mechanical analysis of PCECs and proposes a systematic approach for numerical studies.

Modeling is also a crucial tool for predicting the electrochemical performance of electrolyte membranes. This finding offers a potential explanation for the seemingly contradictory behavior observed in the experimental data. Furthermore, such modeling can be utilized to predict the electrochemical performance of diverse electrochemical cells. Taghikhani *et al* [226] developed an electrochemo-mechanical computational model based on an extended Nernst–Planck equation system. This model predicts transient and steady-state charged defect concentrations (protons, oxygen vacancies, and small polarons), fluxes, and voltages within a dense proton-conducting $BaZr_{0.8}Y_{0.2}O_{3-\delta}$ (10 μm) membrane that is supported on a porous Ni–$BaZr_{0.8}Y_{0.2}O_{3-\delta}$ composite electrode. The model considers the one-dimensional radial behavior in a long tubular cell. The model predicts membrane performance in fuel cell and electrolysis cell modes.

The operation of electrochemical devices is associated with a multitude of complex electrochemical, chemical, and transport processes, including heat, mass, and charge. These processes are highly coupled and difficult to unravel and explain experimentally. Thermoelectrochemical (TE) modeling can be used to obtain a comprehensive understanding of these complex multiphysics phenomena. Li *et al* [227] developed a 2D numerical TE model for a tubular ethane-fueled PCFC based on a thin-film $BaCe_{0.7}Zr_{0.1}Y_{0.2}O_{3-\delta}$ electrolyte (20 μm). The model simulates complex physical, chemical and electrochemical processes occurring in ethane-fueled PCFCs. The effects of the operating voltage, inlet fuel flow rate, and inlet temperature on the electrochemical performance of the indicated PCFC were thoroughly studied. In particular, the relationship between the operating voltage and ethylene yield is revealed. The inlet fuel flow rate at which a high current density is achieved was determined. The importance of increasing the inlet temperature was noted. Furthermore, the effects of the inlet temperature, operating voltage and inlet fuel flow rate on the uniformity of the temperature field within the PCFC and the efficiency of heat removal were evaluated. The most interesting result of the modeling is that H_2 depletion suppressed the local electrochemical performance.

The integration of multiple electrochemical processes (e.g. electrolysis coupled with chemical conversion) has demonstrated the substantial potential of this concept. Such an integration can markedly enhance the functionality of the combined system, increasing its performance and efficiency. However, this necessitates the identification of optimal operating conditions, which can be predicted through computational techniques. Schwabe *et al* [228] presented a scheme and results of energy evaluation of a multifunctional installation in which water vapor electrolysis and methanol synthesis take place. The design is based on a tubular PCEC that can operate at a temperature of 700 °C, a pressure of 10 MPa, and a current (through the electrolyzer) of up to 100 A. The energy evaluation (modeling) results revealed that the proposed scheme has significant potential, but only if the heat of the exothermic synthesis reaction is used to meet the heat demand of electrolysis. Fogel *et al* [229] developed a transient and real-time model of the energy-to-methanol conversion system. The model is based on tubular high-temperature PCECs. Real-time systems that respond to input voltage fluctuations were integrated into the model. The methanol production model from electrolysis includes several feedback control loops or controllers to monitor all subprocesses in the case of fluctuations in power consumption. The modeling results show favorable operating conditions and system efficiency depending on the selected methanol production scheme and electrolyzer thermal design.

In conclusion, it should be noted that the presented works are devoted to modeling the processes occurring in tubular electrochemical devices on the basis of proton-conducting electrolytes, as well as to predicting their characteristics under various parameters. These and similar works are necessary because they contribute to the development of highly efficient and high-performance electrochemical devices, including those related to power generation and the synthesis of environmentally friendly fuels or substances.

7. Conclusions

As demonstrated in this review, proton-conducting oxide electrolytes represent a promising foundation for the advancement of electrochemical cell devices for diverse energy conversion applications at elevated temperatures (typically above 300 °C). These include effective hydrogen separation from H_2-containing gas mixtures, hydrogen production through the electrochemical water splitting process (electrolysis), hydrogen utilization to generate electricity, electroanalytical hydrogen analysis, and a range of hydrogenation and dehydrogenation conversion reactions. These distinctive processes have been thoroughly characterized at the laboratory scale, where highly promising performance outcomes have been attained concurrently. Therefore, this represents a fundamental prerequisite for the scaling-up of such processes through the utilization of protonic ceramic electrochemical cells in the form of prototypes and stacks. Despite the prevalent use of planar-type cells to increase cell power/performance, tube-designed cells are perceived to offer enhanced convenience in terms of the integration of unit cells into stacks and their sealing ability.

This review offers significant insights into the manufacturing and electrochemical characterization of tubular protonic ceramic electrochemical cells. The technological details outlined in section 4 encompass all stages of tube preparation, commencing with the original powder sources utilized and concluding with multistep sintering processes. To elucidate the prehistory of supporting tubular cells, particular attention was devoted to the inorganic/organic components of suspensions, tapes, and slurries.

Section 5 presents the findings for different types of protonic ceramic electrochemical tubes. While many of these processes exhibit good efficiency and performance (for example, up to 100% H_2 recovery and excellent hydrogen analysis), the performance density of the cells with an extended active surface area is significantly lower than that of the cells with a small active surface area. This discrepancy can be attributed to the inadequate current pathways across the entire active surface area of the extended tubes, necessitating the development of new strategies for performance optimization. Such an optimization can be implemented through the consideration of computational results (section 6), which reveal intricate relationships between external variable parameters and output characteristics.

Ultimately, to achieve successful scaling of the protonic ceramic electrochemical tubes in the future, identifying and addressing the current issues and challenges is essential. These, along with potential solutions (outlined in section 6), can facilitate the modernization of the technological scheme, thereby revealing suitable vectors for fabricating the corresponding stacks and modules.

In conclusion, this review provides an overview of the fundamental principles and recent advancements in the development and utilization of tube-designed protonic ceramic electrochemical cells. This information may prove beneficial for researchers, scientists, and technologists specializing in the fields of solid-state electrochemistry, solid-state ionics, electrochemistry, and energy conversion.

8. Future perspective

The previous sections provide insights into the successful fabrication and characterization of tube-shaped protonic ceramic electrochemical cells for various applications. Despite the many promising results achieved, a number of issues should be addressed in more detail to enable rational scaling of the tube technology. These issues can be categorized into chemical and technological classes.

The chemical features of proton-conducting materials are contingent upon their hydration ability and functional properties for specific compositional systems. Some of these properties were previously mentioned in section 3. In addition to the already discussed chemical expansion behavior and chemical stability, proton-conducting electrolytes also demonstrate an inadequate densification capacity, particularly in the case of Zr-enriched compounds. This is attributed to the refractory nature of B-site cations. To achieve the desired sinterability and gas-tight state of electrolyte materials at rational sintering temperatures, a variety of sintering additives have been employed [230–232]. These include NiO, ZnO, CuO, and CoO_x. The introduction of these substances in small amounts (0.1–2 wt.%) results in rapid densification of the electrolytes at 1350 °C–1500 °C, which is technologically suitable for the preparation of Ni-cermet-based half-cells. However, higher sintering temperatures (1550 °C and higher) are required to sinter the electrolyte layer without sintering aids; however, these temperatures are not appropriate for coarsening and reducing the porosity of electrodes. When introduced to proton-conducting electrolytes, the sintering additive facilitates the formation of a liquid phase upon sintering, which in turn results in rapid grain growth of ceramic materials. Owing to capillary forces, the low-melting phase should be concentrated at the grain boundaries upon cooling. However, it should be noted that some portions of the sintering additives may also dissolve into the original electrolyte structure. Since sintering additives (for example, NiO or CuO) or their more complex derivatives (for example, BaY_2NiO_5 or $BaCuO_2$) lack ionic conductivity, their localization at grain boundaries impedes proton transfer. This phenomenon has been widely confirmed for numerous combinations of proton-conducting electrolytes and sintering additives. Unfortunately, the effect of sintering additives cannot be completely excluded, as remarkable nickel ion diffusion from a Ni-based ceramet into an electrolyte was observed during co-sintering of a half-cell [233–235]. Nevertheless, this unwanted diffusion pathway can be effectively mitigated by reducing the sintering temperature or chemically modifying the electrolyte. The latter approach involves the partial or complete replacement of yttrium in Y-doped $Ba(Ce,Zr)O_3$ with other lanthanides (Yb^{3+}, Dy^{3+}, Gd^{3+}) to avoid the formation of the proton-blocking BaY_2NiO_5 phase.

In addition to chemical issues, some technological issues can also be mentioned. After the tubular green anode or half-cell substrates are manufactured, they should be subjected to a careful sintering regime to achieve several goals: the densification of the electrolyte, attaining the requisite mechanical strength, and preserving the selected tube configuration. However, the sintering of prolonged tubes can result in the formation of defects due to TM and shrinkage differences between functional materials or edge defects/strains of individual layers. Potential solutions to this issue include the sintering of the tubes in either a vertically suspended state or a horizontal state via a powder bed. Unfortunately, these sintering details are not widely discussed or even present in the literature.

As previously stated, the larger active electrode surface (working surface area) is consistently associated with reduced power densities compared with those observed in small PCFC or PCEC cells. The underlying cause of these high internal losses is thought to be inadequate current collection at both the inner and outer tube surfaces. Consequently, novel approaches are needed to ensure optimal electrical contact for single prolonged tube cells.

Acknowledgments

This work was prepared within the framework of the budgetary plans of the Hydrogen Energy Laboratory (Ural Federal University) and Institute of High-Temperature Electrochemistry.

Conflict of interest

The authors declare no conflict of interest.

ORCID iDs

Maria A Gordeeva https://orcid.org/0000-0002-1151-247X
Artem P Tarutin https://orcid.org/0000-0001-5636-6499
Nikolai A Danilov https://orcid.org/0000-0003-2983-2110
Dmitry A Medvedev https://orcid.org/0000-0003-1660-6712

References

[1] Baratov S, Filonova E, Ivanova A, Hanif M B, Irshad M, Khan M Z, Motola M, Rauf S and Medvedev D 2024 Current and further trajectories in designing functional materials for solid oxide electrochemical cells: a review of other reviews *J. Energy Chem.* **94** 302–31

[2] Vieri H M, Kim M C, Badakhsh A and Choi S H 2024 Electrochemical synthesis of ammonia via nitrogen reduction and oxygen evolution reactions—a comprehensive review on electrolyte-supported cells *Energies* **17** 441

[3] Buonomenna M G 2023 Proton-conducting ceramic membranes for the production of hydrogen via decarbonized heat: overview and prospects *Hydrogen* **4** 807–30

[4] Wang Y, Ling Y, Wang B, Zhai G, Yang G, Shao Z, Xiao R and Li T 2023 A review of progress in proton ceramic electrochemical cells: material and structural design, coupled with value-added chemical production *Energy Environ. Sci.* **16** 5721–70

[5] Liu F, Ding D and Duan C 2023 Protonic ceramic electrochemical cells for synthesizing sustainable chemicals and fuels *Adv. Sci.* **10** 2206478

[6] Shahid M 2022 Recent advances in protonconducting electrolytes for solid oxide fuel cells *Ionics* **28** 3583–601

[7] Danilov N A, Starostina I A, Starostin G N, Kasyanova A V, Medvedev D A and Shao Z 2023 Fundamental understanding and applications of protonic Y- and Yb-coped Ba(Ce,Zr)O_3 perovskites: state-of-the-art and perspectives *Adv. Energy Mater.* **13** 2302175

[8] Nayak A K and Sasmal A 2023 Recent advance on fundamental properties and synthesis of barium zirconate for proton conducting ceramic fuel cell *J. Clean. Prod.* **386** 135827

[9] Nur Syafkeena M A, Zainor M L, Hassan O H, Baharuddin N A, Othman M H D, Tseng C J and Osman N 2022 Review on the preparation of electrolyte thin films based on cerate-zirconate oxides for electrochemical analysis of anode-supported proton ceramic fuel cells *J. Alloys Compd.* **918** 165434

[10] Song J, Birdja Y Y, Pant D, Chen Z and Vaes J 2022 Recent progress in the structure optimization and development of proton-conducting electrolyte materials for low-temperature solid oxide cells *Int. J. Miner. Metall. Mater.* **29** 848–69

[11] Hanif M B, Rauf S, Abadeen Z, Khan K, Tayyab Z, Qayyum S, Mosiałek M, Shao Z, Li C X and Motola M 2023 Proton-conducting solid oxide electrolysis cells: relationship of composition-structure-property, their challenges, and prospects *Matter* **6** 1782–830

[12] Winiarz P, Covarrubias M S C, Sriubas M, Bockute K, Miruszewski T, Skubida W, Jaworski D, Laukaitis G and Gazda M 2021 Properties of barium cerate-zirconate thin films *Crystals* **11** 1005

[13] Su H and Hu Y H 2022 Degradation issues and stabilization strategies of protonic ceramic electrolysis cells for steam electrolysis *Energy Sci. Eng.* **10** 1706–25

[14] Kasyanova A V, Zvonareva I A, Tarasova N A, Bi L, Medvedev D A and Shao Z 2022 Electrolyte materials for protonic ceramic electrochemical cells: main limitations and potential solutions *Mater. Rep.: Energy* **2** 100158

[15] Yuan B, Wang N, Tang C, Meng L, Du L, Su Q, Aoki Y and Ye S 2024 Advances and challenges in high-performance cathodes for protonic solid oxide fuel cells and machine learning-guided perspectives *Nano Energy* **122** 109306

[16] Oh S, Kim H, Jeong I, Kim D, Yu H and Lee K T 2024 Recent progress in oxygen electrodes for protonic ceramic electrochemical cells *J. Korean Ceram. Soc.* **61** 224–49

[17] Wang N, Tang C, Du L, Zhu R, Xing L, Song Z, Yuan B, Zhao L, Aoki Y and Ye S 2022 Advanced cathode materials for protonic ceramic fuel cells: recent progress and future perspectives *Adv. Energy Mater.* **12** 2201882

[18] Wang M, Su C, Zhu Z, Wang H and Ge L 2022 Composite cathodes for protonic ceramic fuel cells: rationales and materials *Composites* B **238** 109881

[19] Tahir N N M, Baharuddin N A, Samat A A, Osman N and Somalu M R 2022 A review on cathode materials for conventional and proton-conducting solid oxide fuel cells *J. Alloys Compd.* **894** 162458

[20] Mather G C, Muñoz-Gil D, Zamudio-García J, Porras-Vázquez J M, Marrero-López D and Pérez-Coll D 2021 Perspectives on cathodes for protonic ceramic fuel cells *Appl. Sci.* **11** 5363

[21] Bianco M and Ouweltjes J P and Van Herle J 2019 Degradation analysis of commercial interconnect materials for solid oxide fuel cells in stacks operated up to 18000 hours *Int. J. Hydrog. Energy* **44** 31406–22

[22] Hong J, Grimes J, Cox D and Barnett S A 2024 Life testing of 10 cm × 10 cm fuel-electrode-supported solid oxide cells in reversible operation *Appl. Energy* **355** 122275

[23] Bernadet L, Segura-Ruiz J, Yedra L, Estrade S, Peiró F, Montinaro D, Torrell M, Morata A and Tarancón A 2023 Enhanced diffusion barrier layers for avoiding degradation in SOFCs aged for 14000 h during 2 years *J. Power Sources* **555** 232400

[24] Erpalov M V, Tarutin A P, Danilov N A, Osinkin D A and Medvedev D A 2023 Chemistry and electrochemistry of CeO_2-based interlayers: prolonging the lifetime of solid oxide fuel and electrolysis cells *Russ. Chem. Rev.* **92** RCR5097

[25] Amaya Dueñas D M, Ullmer D, Riedel M, Ventura S S, Metten M, Tomberg M, Heddrich M P and Ansar S A 2024 Performance assessment of a 25 kW solid oxide cell module for hydrogen production and power generation *Int. J. Hydrog. Energy* **59** 570–81

[26] Hu Y, Han C, Li W, Hu Q, Wu H and Luo Z 2023 Experimental evaluation of methanol steam reforming reactor heated by catalyst combustion for kW-class SOFC *Int. J. Hydrog. Energy* **48** 4649–64

[27] Peters R, Tiedemann W, Hoven I, Deja R, Kruse N, Fang Q, Schäfer D, Kunz F, Blum L and Peters R Eichel R A 2023 experimental results of a 10/40 kW-class reversible solid oxide cell demonstration system at forschungszentrum Jülich *J. Electrochem. Soc.* **170** 044509

[28] Wencong L, Siyuan L, Zhe Z, Shuzhan B, Guoxiang L, Kongrong M and Yao Q 2023 Performance analysis of a natural gas-fueled 1 kW solid oxide fuel cell-combined heat and power system with off-gas recirculation of anode and cathode *Fuel Cells* **23** 106–18

[29] Choi Y, Byun S, Seo D W, Hwang H J, Kim T W and Kim S D 2022 New design and performance evaluation of 1 kW-class reversible solid oxide electrolysis-fuel cell stack using flat-tubular cells *J. Power Sources* **542** 231744

[30] Königshofer B, Boškoski P, Nusev G, Koroschetz M, Hochfellner M, Schwaiger M, Juričić Đ, Hochenauer C and Subotić V 2021 Performance assessment and evaluation of SOC stacks designed for application in a reversible operated 150 kW rSOC power plant *Appl. Energy* **283** 116372

[31] Blum L, De haart L G J, Malzbender J, Margaritis N and Menzler N H 2016 Anode-supported solid oxide fuel cell achieves 70 000 hours of continuous operation *Energy Technol.* **4** 939–42

[32] Fang Q, de Haart U, Schäfer D, Thaler F, Rangel-Hernandez V, Peters R and Blum L 2020 Degradation analysis of an SOFC short stack subject to 10,000 h of operation *J. Electrochem. Soc.* **167** 144508

[33] Schefold J, Brisse A, Surrey A and Walter C 2020 80,000 current on/off cycles in a one year long steam electrolysis test with a solid oxide cell *Int. J. Hydrog. Energy* **45** 5143–54

[34] Fang Q, Blum L and Stolten D 2019 Electrochemical performance and degradation analysis of an SOFC short stack following operation of more than 100,000 hours *J. Electrochem. Soc.* **166** F1320–5

[35] Fang Q, Blum L and Stolten D 2019 Electrochemical performance and degradation analysis of an SOFC short stack for operation of more than 100,000 hours *ECS Trans.* **91** 687–96

[36] Menzler N H, Sebold D and Guillon O 2018 Post-test characterization of a solid oxide fuel cell stack operated for more than 30,000 hours: the cell *J. Power Sources* **374** 69–76

[37] Schefold J, Brisse A and Poepke H 2017 23,000 h steam electrolysis with an electrolyte supported solid oxide cell *Int. J. Hydrog. Energy* **42** 13415–26

[38] Dailly J, Ancelin M and Marrony M 2017 Long term testing of BCZY-based protonic ceramic fuel cell PCFC: micro-generation profile and reversible production of hydrogen and electricity *Solid State Ion* **306** 69–75

[39] Duan C, Tong J, Shang M, Nikodemski S, Sanders M, Ricote S and Almansoori A and O'Hayre R 2015 Readily processed protonic ceramic fuel cells with high performance at low temperatures *Science* **349** 1321–6

[40] Duan C *et al* 2018 Highly durable, coking and sulfur tolerant, fuel-flexible protonic ceramic fuel cells *Nature* **557** 217–22

[41] Liu Z *et al* 2023 Sintering-induced cation displacement in protonic ceramics and way for its suppression *Nat. Commun.* **14** 7984

[42] Cui J *et al* 2024 Key roles of initial calcination temperature in accelerating the performance in proton ceramic fuel cells via regulating 3D microstructure and electronic structure *Small Struct.* **5** 2300439

[43] Tonekabonimoghaddam M and Shamiri A 2021 Simulation and sensitivity analysis for various geometries and optimization of solid oxide fuel cells: a review *Eng* **2** 386–15

[44] Jamil S, Ahmad S, Ab Rahman M, Othman M H D, Rahman A M, Jaafar J and Ismail A 2019 Structure formation in anode and its effect on the performance of micro-tubular SOFC: a brief review *J. Membr. Sci. Res.* **5** 197–204

[45] Hodjati-Pugh O, Dhir A and Steinberger-Wilckens R 2021 The development of current collection in micro-tubular solid oxide fuel cells—a review *Appl. Sci.* **11** 1077

[46] Zhang X, Jin Y, Li D and Xiong Y 2021 A review on recent advances in micro-tubular solid oxide fuel cells *J. Power Sources* **506** 230135

[47] Han S, Wei T, Wang S, Zhu Y, Guo X, He L, Li X, Huang Q and Chen D 2024 Recent progresses in the development of tubular segmented-in-series solid oxide fuel cells: experimental and numerical study *Int. J. Miner. Metall. Mater.* **31** 427–42

[48] Chen R, Gao Y, Gao J, Zhang H, Motola M, Hanif M B and Li C X 2024 From concept to commercialization: a review of tubular solid oxide fuel cell technology *J. Energy Chem.* **97** 79–109

[49] Mathur L, Namgung Y, Kim H and Song S J 2023 Recent progress in electrolyte-supported solid oxide fuel cells: a review *J. Korean Ceram. Soc.* **60** 614–36

[50] Maiti T K, Majhi J, Maiti S K, Singh J, Dixit P, Rohilla T, Ghosh S, Bhushan S and Chattopadhyay S 2022 Zirconia- and ceria-based electrolytes for fuel cell applications: critical advancements toward sustainable and clean energy production *Environ. Sci. Pollut. Res.* **29** 64489–512

[51] Filonova E and Medvedev D 2022 Recent progress in the design, characterisation and application of LaAlO3- and $LaGaO_3$-based solid oxide fuel cell electrolytes *Nanomaterials* **12** 1991

[52] Zhigachev A O, Rodaev V V, Zhigacheva D V, Lyskov N V and Shchukina M A 2021 Doping of scandia-stabilized zirconia electrolytes for intermediate-temperature solid oxide fuel cell: a review *Ceram. Int.* **47** 32490–504

[53] Shi H, Su C, Ran R, Cao J and Shao Z 2020 Electrolyte materials for intermediate-temperature solid oxide fuel cells *Prog. Nat. Sci.* **30** 764–74

[54] Kasyanova A V, Rudenko A O, Lyagaeva Y G and Medvedev D A 2021 Lanthanum-containing proton-conducting electrolytes with perovskite structures *Membr. Membr. Technol.* **3** 73–97

[55] Zvonareva I A and Medvedev D A 2023 Proton-conducting barium stannate for high-temperature purposes: a brief review *J. Eur. Ceram. Soc.* **43** 198–207

[56] Dunyushkina L A, Belyakov S A and Filatov N M 2023 Proton-conducting alkaline earth hafnates: a review of manufacturing technologies, physicochemical properties and electrochemical performance *J. Eur. Ceram. Soc.* **43** 6681–98

[57] Antonova E P 2023 Proton-conducting oxides based on $LaScO_3$: structure, properties and electrochemical applications. A focus review *Electrochem. Mater. Technol* **2** 20232021

[58] Fop S 2021 Solid oxide proton conductors beyond perovskites *J. Mater. Chem.* A **9** 18836–56

[59] Yang X, Fernández–Carrión A J, Geng X and Kuang X 2024 B-site deficient hexagonal perovskites: structural stability, ionic order-disorder and electrical properties *Prog. Solid State Chem.* **74** 100459

[60] Tarasova N A, Animitsa I E, Galisheva A O and Medvedev D A 2022 Layered and hexagonal perovskites as novel classes of proton-conducting solid electrolytes. A focus review *Electrochem. Mater. Technol.* **1** 20221004

[61] Kim J, Jun A, Gwon O, Yoo S, Liu M, Shin J, Lim T H and Kim G 2018 Hybrid-solid oxide electrolysis cell: a new strategy for efficient hydrogen production *Nano Energy* **44** 121–6

[62] Zhou C, Sunarso J, Song Y, Dai J, Zhang J, Gu B, Zhou W and Shao Z 2019 New reduced-temperature ceramic fuel cells with dual-ion conducting electrolyte and triple-conducting double perovskite cathode *J. Mater. Chem.* A **7** 13265–74

[63] He F, Teng Z, Yang G, Zhou C, Guan D, Chen S, Ran R, Wang W, Zhou W and Shao Z 2020 Manipulating cation nonstoichiometry towards developing better electrolyte for self-humidified dual-ion solid oxide fuel cells *J. Power Sources* **460** 228105

[64] Qasem N A A and Abdulrahman G A Q 2024 A recent comprehensive review of fuel cells: history, types, and applications *Int. J. Energy Res.* accepted (https://doi.org/10.1155/2024/7271748)

[65] Perry M L and Fuller T F 2002 A historical perspective of fuel cell technology in the 20th century *J. Electrochem. Soc.* **149** S59

[66] Liu Y, Shao Z, Mori T and Jiang S P 2021 Development of nickel based cermet anode materials in solid oxide fuel cells—now and future *Mater. Rep.: Energy* **1** 100003

[67] Choolaei M, Vostakola M F and Horri B A 2023 Recent advances and challenges in thin-film fabrication techniques for Low-temperature Solid oxide Fuel Cells *Crystals* **13** 1008

[68] Liang F *et al* 2022 A review of thin film electrolytes fabricated by physical vapor deposition for solid oxide fuel cells *Int. J. Hydrog. Energy* **47** 36926–52

[69] Xu H, Han Y, Zhu J, Ni M and Yao Z 2024 Status and progress of metal-supported solid oxide fuel cell: towards large-scale manufactory and practical applications *Energy Rev.* **3** 100051

[70] Mao J, Wang E, Wang H, Ouyang M, Chen Y, Hu H, Lu L, Ren D and Liu Y 2023 Progress in metal corrosion mechanism and protective coating technology for interconnect and metal support of solid oxide cells *Renew. Sustain. Energy Rev.* **185** 113597

[71] Opakhai S and Kuterbekov K 2023 Metal-supported Solid oxide Fuel Cells: a review of recent Developments and Problems *Energies* **16** 4700

[72] Tucker M C 2020 Progress in metal-supported solid oxide electrolysis cells: a review *Int. J. Hydrog. Energy* **45** 24203–18

[73] Du P, Wu J, Li Z, Wang X and Jia L 2023 Failure mechanism and optimization of metal-supported solid oxide fuel cells *Materials* **16** 3978

[74] Wang Y, Shi J, Gu X, Deutschmann O, Shi Y and Cai N 2024 Toward mobility of solid oxide fuel cells *Prog. Energy Combust. Sci.* **102** 101141

[75] Kuterbekov K A, Nikonov A V, Bekmyrza K Z, Pavzderin N B, Kabyshev A M, Kubenova M M, Kabdrakhimova G D and Aidarbekov N 2022 Classification of solid oxide fuel cells *Nanomaterials* **12** 1059

[76] Medvedev D, Murashkina A, Pikalova E, Demin A, Podias A and Tsiakaras P 2014 $BaCeO_3$: materials development, properties and application *Prog. Mater. Sci.* **60** 72–129

[77] Han D, Majima M and Uda T 2013 Structure analysis of $BaCe_{0.8}Y_{0.2}O_{3-\delta}$ in dry and wet atmospheres by high-temperature x-ray diffraction measurement *J. Solid State Chem.* **205** 122–8

[78] Eriksson Andersson A K, Selbach S M, Grande T and Knee C S 2015 Thermal evolution of the crystal structure of proton conducting $BaCe_{0.8}Y_{0.2}O_{3-\delta}$ from high-resolution neutron diffraction in dry and humid atmosphere *Dalton. Trans.* **44** 10834–46

[79] Wu J, Li L P, Espinosa W T P and Haile S M 2004 Defect chemistry and transport properties of $Ba_xCe_{0.85}M_{0.15}O_{3-\delta}$ *J. Mater. Res.* **19** 2366–76

[80] Islam M S, Slater P R, Tolchard J R and Dinges T 2004 Doping and defect association in $AZrO_3$ (A = Ca, Ba) and $LaMO_3$ (M = Sc, Ga) perovskite-type ionic conductors *Dalton. Trans.* **19** 3061–6

[81] Stokes S J and Islam M S 2010 Defect chemistry and proton-dopant association in $BaZrO_3$ and $BaPrO_3$ *J. Mater. Chem.* **20** 6258

[82] Bonanos N 2001 Oxide-based protonic conductors: point defects and transport properties *Solid State Ion* **145** 265–74

[83] Hiraiwa C, Han D, Kuramitsu A, Kuwabara A, Takeuchi H, Majima M and Uda T 2013 Chemical expansion and change in lattice constant of Y-doped $BaZrO_3$ by hydration/dehydration reaction and final heat-treating temperature *J. Am. Ceram. Soc.* **96** 879–84

[84] Andersson A K E, Selbach S M, Knee C S and Grande T 2014 Chemical expansion due to hydration of proton-conducting perovskite oxide ceramics *J. Am. Ceram. Soc.* **97** 2654–61

[85] Jedvik E, Lindman A, Benediktsson M and Wahnström G 2015 Size and shape of oxygen vacancies and protons in acceptor-doped barium zirconate *Solid State Ion* **275** 2–8

[86] Løken A, Haugsrud R and Bjørheim T S 2016 Unravelling the fundamentals of thermal and chemical expansion of $BaCeO_3$ from first principles phonon calculations *Phys. Chem. Chem. Phys.* **18** 31296–303

[87] Hudish G, Manerbino A, Coors W G and Ricote S 2018 Chemical expansion in $BaZr_{0.9-x}Ce_xY_{0.1}O_{3-\delta}$ (x= 0 and 0.2) upon hydration determined by high-temperature X-ray diffraction *J. Am. Ceram. Soc.* **101** 1298–309

[88] Løken A, Ricote S and Wachowski S 2018 Thermal and chemical expansion in proton ceramic electrolytes and compatible electrodes *Crystals* **8** 365

[89] Hoshino K, Hyodo J and Yamazaki Y 2021 Non-linear behavior for chemical expansion in yttrium-doped barium zirconate upon hydration *Chem. Lett.* **50** 899–902

[90] Starostin G N, Tsvetkov D S, Starostina I A, Sereda V V, Akopian M T, Malyshkin D A, Ivanov I L, Murashkina A A, Zuev A Y and Medvedev D A 2024 Fundamental and technological aspects of thermochemical expansion of proton-conducting oxides: a case study of $BaSn_{1-x}Sc_xO_{3-\delta}$ *J. Mater. Chem.* A **12** 14022–34

[91] Zohourian R, Merkle R, Raimondi G and Maier J 2018 Mixed-conducting perovskites as cathode materials for protonic ceramic fuel cells: understanding the trends in proton uptake *Adv. Funct. Mater.* **28** 1801241

[92] Merkle R, Hoedl M F, Raimondi G, Zohourian R and Maier J 2021 Oxides with mixed protonic and electronic conductivity *Annu. Rev. Mater. Res.* **51** 461–93

[93] Loureiro F J A, Shakel Z, Graça V C D and Fagg D P 2021 Effect of humidification on the grain boundary conductivity and space-charge effects in yttrium-doped barium cerate *Int. J. Hydrog. Energy* **46** 23828–38

[94] Luo Z, Hu X, Zhou Y, Ding Y, Zhang W, Li T and Liu M 2024 Harnessing high-throughput computational methods to accelerate the discovery of optimal proton conductors for high-performance and durable protonic ceramic electrochemical cells *Adv. Mater.* **36** 2311159

[95] Luo Z, Zhou Y, Hu X, Kane N, Li T, Zhang W, Liu Z, Ding Y, Liu Y and Liu M 2022 Critical role of acceptor dopants in designing highly stable and compatible proton-conducting electrolytes for reversible solid oxide cells *Energy Environ. Sci.* **15** 2992–3003

[96] Luo Z, Zhou Y, Hu X, Kane N, Zhang W, Li T, Ding Y, Liu Y and Liu M 2022 Highly conductive and durable Nb(Ta)-doped proton conductors for reversible solid oxide cells *ACS Energy Lett.* **7** 2970–8

[97] He S and Jiang S P 2021 Electrode/electrolyte interface and interface reactions of solid oxide cells: recent development and advances *Prog. Nat. Sci.* **31** 341–72

[98] Khan M Z, Song R H, Mehran M T, Lee S B and Lim T H 2021 Controlling cation migration and inter-diffusion across cathode/interlayer/electrolyte interfaces of solid oxide fuel cells: a review *Ceram. Int.* **47** 5839–69

[99] Choudhary B, Besra L, Anwar S and Anwar S 2023 $La_2Ce_2O_7$ based materials for next generation proton conducting solid oxide cells: progress, opportunity and future prospects *Int. J. Hydrog. Energy* **48** 28460–501

[100] Kochetova N, Animitsa I, Medvedev D, Demin A and Tsiakaras P 2016 Recent activity in the development of proton-conducting oxides for high-temperature applications *RSC Adv.* **6** 73222–68

[101] Medvedev D A 2021 Current drawbacks of proton-conducting ceramic materials: how to overcome

them for real electrochemical purposes *Curr. Opin. Green Sustain. Chem.* **32** 100549

[102] Shin Y and Rondinelli J M 2022 Magnetic structure of oxygen-deficient perovskite nickelates with ordered vacancies *Phys. Rev. Res.* **4** L022069

[103] Mikami Y, Goto T, Asano H, Kasuga K, Yamauchi K, Kuroha T and Okuyama Y 2024 Performance of protonic ceramic fuel cells with Ba(Zr,Yb,Co)$O_{3\text{-}\delta}$ cathodes and the impact of co contained in cathode on durability *J. Power Sources* **613** 234832

[104] Shimada H *et al* 2024 Improved durability of protonic ceramic fuel cells with BaZr0.8Yb0.2O3—electrolyte by introducing porous $BaZr_{0.1}Ce_{0.7}Y_{0.1}Yb_{0.1}O_{3\text{–}\delta}$ buffer interlayer *Ceram. Int.* **50** 3895–901

[105] Mikami Y, Sekitani Y, Yamauchi K, Kuroha T and Okuyama Y 2024 Effect of transition Element dissolution on Ytterbium-doped Barium-Zirconate-based Protonic ceramic Fuel Cells *ACS Appl. Energy Mater.* **7** 1136–48

[106] Segami T, Sato R, Budiman R A, Yamaguchi M, Yashiro K and Kawada T 2024 Evaluation of the effect of oxygen incorporation on the thermo–chemical–mechanical properties of the proton-conducting oxide $BaZr_{0.8}Yb_{0.2}O_{3\text{-}\delta}$ *Acta Mater.* **273** 119978

[107] Niwa E, Kluczny M, Kim H Y, Song J T, Watanabe M, Takagaki A and Ishihara T 2023 Proton conductivity in Yb-doped $BaZrO_3$-based thin film prepared by pulsed laser deposition *Solid State Ion* **396** 116240

[108] Zvonareva I, Fu X Z, Medvedev D and Shao Z 2021 Electrochemistry and energy conversion features of protonic ceramic cells with mixed ionic-electronic electrolytes *Energy Environ. Sci.* **15** 439–65

[109] Huang Y, Qiu R, Lian W, Lei L, Liu T, Zhang J, Wang Y, Liu J, Huang J and Chen F 2022 Review: measurement of partial electrical conductivities and transport numbers of mixed ionic-electronic conducting oxides *J. Power Sources* **528** 231201

[110] Matkin D E, Starostina I A, Hanif M B and Medvedev D A 2024 Revisiting the ionic conductivity of solid oxide electrolytes: a technical review *J. Mater. Chem.* A (https://doi.org/10.1039/D4TA03852E)

[111] Yoon H, Song S J, Oh T, Li J, Duncan K L and Wachsman E D 2009 Fabrication of thin-film $SrCe_{0.9}Eu_{0.1}O_{3-\delta}$ hydrogen separation membranes on Ni–$SrCeO_3$ porous tubular supports *J. Am. Ceram. Soc.* **92** 1849–52

[112] Yoon H, Oh T, Li J, Duncan K L and Wachsman E D 2009 Permeation through $SrCe_{0.9}Eu_{0.1}O_{3-\delta}$/Ni–$SrCeO_3$ tubular hydrogen separation membranes *J. Electrochem. Soc.* **156** B791

[113] Li J, Yoon H, Oh T and Wachsman E D 2010 Stability of $SrCe_{1-x}Zr_xO_{3-\delta}$ under water gas shift reaction conditions *J. Electrochem. Soc.* **157** B383

[114] Jamil S M, Othman M H D, Rahman M A, Jaafar J, Ismail A F and Li K 2015 Recent fabrication techniques for micro-tubular solid oxide fuel cell support: a review *J. Eur. Ceram. Soc.* **35** 1–22

[115] Meng X, Yang N, Yin Y, Tan X and Ma Z 2011 Fabrication techniques and stack assembling methods for micro tubular solid oxide fuel cells *CIESC J.* **62** 2977–86

[116] Zhao F, Jin C, Yang C, Wang S and Chen F 2011 Fabrication and characterization of anode-supported micro-tubular solid oxide fuel cell based on $BaZr_{0.1}Ce_{0.7}Y_{0.1}Yb_{0.1}O_{3-\delta}$ electrolyte *J. Power Sources* **196** 688–91

[117] Zhao L, Zhang X, He B, Liu B and Xia C 2011 Micro-tubular solid oxide fuel cells with graded anodes fabricated with a phase inversion method *J. Power Sources* **196** 962–7

[118] Zhao L, He B, Shen J, Chen F and Xia C 2011 $BaZr_{0.1}Ce_{0.7}Y_{0.2}O_{3-\delta}$ as an electronic blocking material for microtubular solid oxide fuel cells based on doped ceria electrolyte *Electrochem. Commun.* **13** 450–3

[119] Yang C, Xu Q, Zhu Z and Liu W 2012 Hydrogen permeation performance of Ni-$BaZr_{0.1}Ce_{0.7}Y_{0.2}O_{3-\delta}$ metal-ceramic hollow fiber membrane *Chin. J. Chem. Phys.* **25** 125–8

[120] He B, Ding D, Ling Y, Zhao L and Cheng J 2014 Fabrication and evaluation of stable micro tubular solid oxide fuel cells with BZCY-BZY bi-layer proton conducting electrolytes *Int. J. Hydrog. Energy* **39** 19087–92

[121] Chen Y, Liao Q, Li Z, Wang H, Wei Y, Feldhoff A and Caro J 2015 ACO_2-stable hollow-fiber membrane with high hydrogen permeation flux *AIChE J.* **61** 1997–2007

[122] Ren C, Wang S, Liu T, Lin Y and Chen F 2015 Fabrication of micro-tubular solid oxide fuel cells using sulfur-free polymer binder via a phase inversion method *J. Power Sources* **290** 1–7

[123] Meng X, Shang Y, Meng B, Yang N, Tan X, Sunarso J and Liu S 2016 Bi-functional performances of $BaCe_{0.95}Tb_{0.05}O_{3-\delta}$-based hollow fiber membranes for power generation and hydrogen permeation *J. Eur. Ceram. Soc.* **36** 4123–9

[124] Liu H, Chen Y, Wei Y and Wang H 2017 CO_2-tolerant U-shaped hollow fiber membranes for hydrogen separation *Int. J. Hydrog. Energy* **42** 4208–15

[125] Wang T, Wang H, Meng X, Meng B, Tan X, Sunarso J and Liu S 2017 Enhanced hydrogen permeability and reverse water–gas shift reaction activity via magneli Ti_4O_7 doping into $SrCe_{0.9}Y_{0.1}O_{3-\delta}$ hollow fiber membrane *Int. J. Hydrog. Energy* **42** 12301–9

[126] Chen C, Dong Y, Li L, Wang Z, Liu M, Rainwater B H and Bai Y 2019 Electrochemical properties of micro-tubular intermediate temperature solid oxide fuel cell with novel asymmetric structure based on $BaZr_{0.1}Ce_{0.7}Y_{0.1}Yb_{0.1}O_{3-\delta}$ proton conducting electrolyte *Int. J. Hydrog. Energy* **44** 16887–97

[127] Li F, Duan G, Wang Z, Liu D, Cui Y, Kawi S, Liu S and Tan X 2022 Highly efficient recovery of hydrogen from dilute H2-streams using $BaCe_{0.7}Zr_{0.1}Y_{0.2}O_{3\text{-}\delta}$/Ni-$BaCe_{0.7}Zr_{0.1}Y_{0.2}O_{3\text{-}\delta}$ dual-layer hollow fiber membrane *Sep. Purif. Technol.* **287** 120602

[128] Tong G, Li F, Li Y, Wang Z and Tan X 2024 Structural tailoring of the current collector/anode dual-layer hollow fibers to enhance the performance of micro-tubular protonic ceramic fuel cells *Int. J. Hydrog. Energy* **63** 274–83

[129] Tong G, Li F, Wang M, Wang Z and Tan X 2023 Microstructure tailoring of the $BaCe_{0.7}Zr_{0.1}Y_{0.2}O_{3\text{-}\delta}$ (BCZY)/Ni-BCZY dual-layer hollow fibers by co-spinning/co-sintering for high performance micro-tubular protonic ceramic fuel cells (MT-PCFCs) *J. Eur. Ceram. Soc.* **43** 3404–13

[130] Hong T, Li C, Pan X, Lu Y, Liu T, Zhang G and Cheng J 2024 Novel bio-inspired micro-tubular protonic ceramic fuel cells with unique four-channel hollow structure *Ceram. Int.* **130** 40570–8

[131] Tong G, Li Y, Wang Z and Tan X 2023 Batch fabrication of micro-tubular protonic ceramic fuel cells via a phase inversion-based co-spinning/co-sintering technique *J. Power Sources* **585** 233605

[132] Chen C, Liu M, Bai Y, Yang L, Xie E and Liu M 2011 Anode-supported tubular SOFCs based on $BaZr_{0.1}Ce_{0.7}Y_{0.1}Yb_{0.1}O_{3-\delta}$ electrolyte fabricated by dip coating *Electrochem. Commun.* **13** 615–8

[133] Chen C, Dong Y, Li L, Wang Z, Liu M, Rainwater B H and Bai Y 2019 High performance of anode supported $BaZr_{0.1}Ce_{0.7}Y_{0.1}Yb_{0.1}O_{3-\delta}$ proton-conducting electrolyte micro-tubular cells with asymmetric structure for IT-SOFCs *J. Electroanal. Chem.* **844** 49–57

[134] Dong Y, Chen C, Liu M, Rainwater B H and Bai Y 2020 Enhancement of electrochemical properties, impedance and resistances of micro-tubular IT-SOFCs with novel asymmetric structure based on $BaZr_{0.1}Ce_{0.7}Y_{0.1}Yb_{0.1}O_{3-\delta}$ proton conducting electrolyte *Fuel Cells* **20** 70–79

[135] Cao D, Zhou M, Yan X, Liu Z and Liu J 2021 High performance low-temperature tubular protonic ceramic fuel cells based on barium cerate-zirconate electrolyte *Electrochem. Commun.* **125** 106986

[136] Beyribey B, Bayne J and Persky J 2022 The effect of dip-coating parameters on the thickness and uniformity of BCZYZ electrolyte layer on porous NiO-BCZYZ tubular supports *Ceram. Int.* **48** 6046–51

[137] Pan Y, Zhang H, Xu K, Zhou Y, Zhao B, Yuan W, Sasaki K, Choi Y M, Chen Y and Liu M 2022 A high-performance and durable direct NH_3 tubular protonic ceramic fuel cell integrated with an internal catalyst layer *Appl. Catal.* B **306** 121071

[138] Hou M, Pan Y and Chen Y 2022 Enhanced electrochemical activity and durability of a direct ammonia protonic ceramic fuel cell enabled by an internal catalyst layer *Sep. Purif. Technol.* **297** 121483

[139] He F, Hou M, Du Z, Zhu F, Cao X, Ding Y, Zhou Y, Liu M and Chen Y 2023 Self-construction of efficient interfaces ensures high-performance direct ammonia protonic ceramic fuel cells *Adv. Mater.* **35** 2304957

[140] Hou M, Zhu F, Liu Y and Chen Y 2023 A high-performance fuel electrode-supported tubular protonic ceramic electrochemical cell *J. Eur. Ceram. Soc.* **43** 6200–7

[141] Nowicki K M, Carins G, Bayne J, Tupberg C, Irvine G J and Irvine J T S 2022 Characterisation of direct ammonia proton conducting tubular ceramic fuel cells for maritime applications *J. Mater. Chem.* A **11** 352–63

[142] Robinson S, Manerbino A, Grover Coors W and Sullivan N P 2013 Fabrication and performance of tubular, electrode-supported $BaCe_{0.2}Zr_{0.7}Y_{0.1}O_{3-\delta}$ fuel cells *Fuel Cells* **13** 584–91

[143] Robinson S, Manerbino A and Grover Coors W 2013 Galvanic hydrogen pumping in the protonic ceramic perovskite *J. Membr. Sci.* **446** 99–105

[144] Kyriakou V, Garagounis I, Vourros A, Vasileiou E, Manerbino A, Coors W G and Stoukides M 2016 Methane steam reforming at low temperatures in a $BaZr_{0.7}Ce_{0.2}Y_{0.1}O_{2.9}$ proton conducting membrane reactor *Appl. Catal.* B **186** 1–9

[145] Patki N S, Manerbino A, Way J D and Ricote S 2018 Galvanic hydrogen pumping performance of copper electrodes fabricated by electroless plating on a $BaZr_{0.9\text{-}x}Ce_xY_{0.1}O_{3\text{-}\delta}$ proton-conducting ceramic membrane *Solid State Ion* **317** 256–62

[146] Vøllestad E, Strandbakke R, Tarach M, Catalán-Martínez D, Fontaine M L, Beeaff D, Clark D R, Serra J M and Norby T 2019 Mixed proton and electron conducting double perovskite anodes for stable and efficient tubular proton ceramic electrolysers *Nat. Mater.* **18** 752–9

[147] Cheng H, Meng B, Wang X, Meng X and Liu S 2020 CO_2 and Steam-assisted H_2 separation through $BaCe_{0.8}Y_{0.2}O_{3-\delta}$–$Ce_{0.8}Y_{0.2}O_{2-\delta}$ hollow Fiber Membranes *Energy Fuels* **34** 683–9

[148] Yuste-Tirados I, Liu X, Kjølseth C and Norby T 2023 Impedance of a tubular electrochemical cell with BZCY electrolyte and Ni-BZCY cermet electrodes for proton ceramic membrane reactors *Int. J. Hydrog. Energy* **48** 30027–38

[149] Quina I, Almar L, Catalán-Martínez D, Dayaghi A M, Martínez A, Norby T, Escolástico S and Serra J M 2023 Direct electrocatalytic CO_2 reduction in a pressurized tubular protonic membrane reactor *Chem. Catal.* **3** 100766

[150] Ruiz E, Aldecoa J, Morales Á, Farchado M and Sánchez J M 2024 Methanation of CO_2 on cu in a tubular co-ionic SOEC *Int. J. Hydrog. Energy* **52** 1338–59

[151] Yuste-Tirados I, Liu X, Kjølseth C and Norby T 2024 Boundaries of DC operation of a tubular proton ceramic electrochemical reactor with BZCY electrolyte and Ni-BZCY cermet electrodes *J. Power Sources* **596** 234097

[152] Min S H, Song R H, Lee J G, Park M G, Ryu K H, Jeon Y K and Shul Y 2014 Fabrication of anode-supported tubular $Ba(Zr_{0.1}Ce_{0.7}Y_{0.2})O_{3-\delta}$ cell for intermediate temperature solid oxide fuel cells *Ceram. Int.* **40** 1513–8

[153] Kuroha T, Yamauchi K, Mikami Y, Tsuji Y, Niina Y, Shudo M, Sakai G and Matsunaga N, Okuyama Y 2020 Effect of added Ni on defect structure and proton transport properties of indium-doped barium zirconate *Int. J. Hydrog. Energy* **45** 3123–31

[154] Li G, Gou Y, Ren R, Xu C, Qiao J, Sun W, Wang Z and Sun K 2021 Fluorinated $Pr_2NiO_{4+\delta}$ as high-performance air electrode for tubular reversible protonic ceramic cells *J. Power Sources* **508** 230343

[155] Zhu L, O'Hayre R and Sullivan N P 2021 High performance tubular protonic ceramic fuel cells via highly-scalable extrusion process *Int. J. Hydrog. Energy* **46** 27784–92

[156] Kee R J, Ricote S, Zhu H, Braun R J, Carins G and Persky J E 2022 Perspectives on technical challenges and scaling considerations for tubular protonic-ceramic electrolysis cells and stacks *J. Electrochem. Soc.* **169** 054525

[157] Hanifi A R, Sandhu N K, Etsell T H, Luo J L and Sarkar P 2017 Fabrication and characterization of a tubular ceramic fuel cell based on $BaZr_{0.1}Ce_{0.7}Y_{0.1}Yb_{0.1}O_{3\text{-}\delta}$ proton conducting electrolyte *J. Power Sources* **341** 264–9

[158] Amiri T, Singh K, Sandhu N K, Hanifi A R, Etsell T H, Luo J L, Thangadurai V and Sarkar P 2018 High performance tubular solid oxide fuel cell based on $Ba_{0.5}Sr_{0.5}Ce_{0.6}Zr_{0.2}Gd_{0.1}Y_{0.1}O_{3\text{-}\delta}$ proton conducting electrolyte *J. Electrochem. Soc.* **165** F764–9

[159] Vafaeenezhad S, Sandhu N K, Hanifi A R, Etsell T H and Sarkar P 2019 Ni-YSZ a new support for proton conducting fuel cells *ECS Trans.* **91** 1085–94

[160] Vafaeenezhad S, Sandhu N K, Hanifi A R, Etsell T H and Sarkar P 2019 Development of proton conducting fuel cells using nickel metal support *J. Power Sources* **435** 226763

[161] Xiao Y, Wang M, Bao D, Wang Z, Jin F, Wang Y and He T 2023 Performance of fuel electrode-supported tubular protonic ceramic cells prepared through slip casting and dip-coating methods *Catalysts* **13** 182

[162] Ricote S, Kee R and Coors W 2022 Slip casting and solid-state reactive sintering of $BCZY(BaCe_xZr_{0.9-x}Y_{0.1}O_{3-\delta})$-NiO/BCZY half-cells *Membranes* **12** 242

[163] Kuzmin A V *et al* 2020 $LaScO_3$-based electrolyte for protonic ceramic fuel cells: influence of sintering additives on the transport properties and electrochemical performance *J. Power Sources* **466** 228255

[164] Tarutin A, Kasyanova A, Lyagaeva J, Vdovin G and Medvedev D 2020 Towards high-performance tubular-type protonic ceramic electrolysis cells with all-Ni-based functional electrodes *J. Energy Chem.* **40** 65–74

[165] Medvedev D, Lyagaeva J, Vdovin G, Beresnev S, Demin A and Tsiakaras P 2016 A tape calendering method as an effective way for the preparation of proton ceramic fuel cells with enhanced performance *Electrochim. Acta* **210** 681–8

[166] Ye X F, Wen Y B, Yang S J, Lu Y, Luo W H, Wen Z Y and Meng J B 2017 Study of $CaZr_{0.9}In_{0.1}O_{3-\delta}$ based reversible solid oxide cells with tubular electrode supported structure *Int. J. Hydrog. Energy* **42** 23189–97

[167] Chen C, Wang Z, Miao X, Sun C, Ye X and Wen Z 2023 Cycling performance and interface stability research of tubular protonic reversible solid oxide cells with air electrodes by different manufacturing processes *Electrochem. Commun.* **151** 107507

[168] Mu S *et al* 2020 A novel laser 3D printing method for the advanced manufacturing of protonic ceramics *Membranes* **10** 98

[169] Zou M *et al* 2023 3D printing enabled highly scalable tubular protonic ceramic fuel cells *ACS Energy Lett.* **8** 3545–51

[170] Vourros A, Kyriakou V, Garagounis I, Vasileiou E and Stoukides M 2017 Chemical reactors with high temperature proton conductors as a main component: progress in the past decade *Solid State Ion* **306** 76–81

[171] Zhao Z, Zou M, Huang H and Tong J 2023 Protonic electrocatalytic membrane reactors *Current Trends and Future Developments on (Bio)membranes* (Elsevier Inc.) pp 21–57

[172] Duan C, Huang J, Sullivan N and O'Hayre R 2020 Proton-conducting oxides for energy conversion and storage *Appl. Phys. Rev.* **7** 011314

[173] Qu L and Papaioannou E I 2024 Development of mixed ionic and electronic conducting materials for gas separation membranes: a critical overview *Chem. Eng. J.* **496** 153791

[174] Zhang Z, Zhou W, Wang T, Gu Z, Zhu Y, Liu Z, Wu Z, Zhang G and Jin W 2023 Ion–conducting ceramic membrane reactors for the conversion of chemicals *Membranes* **13** 621

[175] Zhao J, Pang Y, Su C, Jiang S and Ge L 2023 Toward high performance mixed ionic and electronic conducting perovskite-based oxygen permeable membranes: an overview of strategies and rationales *Energy Fuels* **37** 7042–61

[176] Han N, Shen Z, Zhao X, Chen R and Thakur V K 2022 Perovskite oxides for oxygen transport: chemistry and material horizons *Sci. Total Environ.* **806** 151213

[177] Chen G *et al* 2022 Roadmap for sustainable mixed Ionic-electronic conducting membranes *Adv. Funct. Mater.* **32** 2105702

[178] Liu Y, Tan X and Li K 2006 $SrCe_{0.95}Yb_{0.05}O_{3-\alpha}$ (SCYb) hollow fibre membrane: preparation, characterization and performance *J. Membr. Sci* **283** 380–5

[179] Tan X, Tan X, Yang N, Meng B, Zhang K and Liu S 2014 High performance $BaCe_{0.8}Y_{0.2}O_{3-a}$ (BCY) hollow fibre membranes for hydrogen permeation *Ceram. Int.* **40** 3131–8

[180] Song J, Li L, Tan X and Li K 2013 $BaCe_{0.85}Tb_{0.05}Co_{0.1}O_{3-\delta}$ perovskite hollow fibre membranes for hydrogen/oxygen permeation *Int. J. Hydrog. Energy* **38** 7904–12

[181] Li J, Yoon H and Wachsman E D 2011 Hydrogen permeation through thin supported $SrCe_{0.7}Zr_{0.2}Eu_{0.1}O_{3-\delta}$ membranes; dependence of flux on defect equilibria and operating conditions *J. Membr. Sci* **381** 126–31

[182] Tan X, Song J, Meng X and Meng B 2012 Preparation and characterization of $BaCe_{0.95}Tb_{0.05}O_{3-\alpha}$ hollow fibre membranes for hydrogen permeation *J. Eur. Ceram. Soc.* **32** 2351–7

[183] Cheng H, Wang X, Meng X, Meng B, Sunarso J, Tan X, Liu L and Liu S 2020 Dual-layer $BaCe_{0.8}Y_{0.2}O_{3-\delta}$-$Ce_{0.8}Y_{0.2}O_{2-\delta}$/$BaCe_{0.8}Y_{0.2}O_{3-\delta}$-ni hollow fiber membranes for H2 separation *J. Membr. Sci* **601** 117801

[184] Shang Y, Wei L, Meng X, Meng B, Yang N, Sunarso J and Liu S 2018 CO_2-enhanced hydrogen permeability of dual-layered A-site deficient $Ba_{0.95}Ce_{0.85}Tb_{0.05}Zr_{0.1}O_{3-\delta}$-based hollow fiber membrane *J. Membr. Sci* **546** 82–89

[185] Oh T, Yoon H, Li J and Wachsman E D 2009 Hydrogen permeation through thin supported $SrZr_{0.2}Ce_{0.8-x}Eu_xO_{3-\delta}$ membranes *J. Membr. Sci* **345** 1–4

[186] Tanaka M and Ohshima T 2010 Recovery of hydrogen from gas mixture by an intermediate-temperature type proton conductor *Fusion Eng. Des.* **85** 1038–43

[187] Tanaka M, Katahira K, Asakura Y and Ohshima T 2010 Hydrogen pump using a high-temperature proton conductor for nuclear fusion engineering applications *Solid State Ion* **181** 215–8

[188] Volkov A, Gorbova E, Vylkov A, Medvedev D, Demin A and Tsiakaras P 2017 Design and applications of potentiometric sensors based on proton-conducting ceramic materials. A brief review *Sens. Actuators* B **244** 1004–15

[189] Gorbova E, Tzorbatzoglou F, Molochas C, Chloros D, Demin A and Tsiakaras P 2021 Fundamentals and principles of solid-state electrochemical sensors for high temperature gas detection *Catalysts* **12** 1

[190] Starostin G, Volkov A N, Kalyakin A S and Medvedev D A 2024 High-temperature gas sensors based on proton-conducting ceramic oxides. A brief review *Ceram. Int.* **50** 37449–59

[191] Hassen M A, Clarke A G, Swetnam M A, Kumar R V and Fray D J 2000 High temperature humidity monitoring using doped strontium cerate sensors *Sens. Actuators* B **69** 138–43

[192] Chen J, Wu S, Zhang F, Lü S and Mao Y 2016 Calcination temperature dependence of synthesis process and hydrogen sensing properties of In-doped $CaZrO_3$ *Mater. Chem. Phys.* **172** 87–97

[193] Ohshima T, Kondo M, Tanaka M, Muroga T and Sagara A 2010 Hydrogen transport in molten salt flinak measured by solid electrolyte sensors with pd electrode *Fusion Eng. Des.* **85** 1841–6

[194] Hanifi A R, Sandhu N K, Etsell T H and Sarkar P 2017 Development of a novel proton conducting fuel cell based on a Ni-YSZ support *J. Am. Ceram. Soc.* **100** 4983–7

[195] Sahini M G, Mwankemwa B S and Kanas N 2022 $Ba_xSr_{1-x}Co_yFe_{1-y}O_{3-\delta}$ (BSCF) mixed ionic-electronic conducting (MIEC) materials for oxygen separation membrane and SOFC applications: insights into processing, stability, and functional properties *Ceram. Int.* **48** 2948–64

[196] Klyndyuk A I, Chizhova E A, Kharytonau D S and Medvedev D A 2021 Layered oxygen-deficient double perovskites as promising cathode materials for solid oxide fuel cells *Materials* **15** 141

[197] Tarutina L R *et al* 2024 Why do $BaCo_{0.4}Fe_{0.4}Zr_{0.1}Y_{0.1}O_{3-\delta}$-derived complex oxides become one of the most promising electrodes for protonic ceramic electrochemical cells? an explanatory review *Chem. Eng. J.* **490** 151615

[198] Kim Y D, Kim I H, Meisel C, Herradón C, Rand P W, Yang J, Kim H S, Sullivan N P and O'Hayre R 2024 Improving tubular protonic ceramic fuel cell performance by compensating ba evaporation via a Ba-excess optimized proton conducting electrolyte synthesis strategy *J. Phys. Energy* **6** 035004

[199] Medvedev D 2019 Trends in research and development of protonic ceramic electrolysis cells *Int. J. Hydrog. Energy* **44** 26711–40

[200] Lei L, Zhang J, Yuan Z, Liu J, Ni M and Chen F 2019 Progress report on proton conducting solid oxide electrolysis cells *Adv. Funct. Mater.* **29** 1903805

[201] Fallah Vostakola M, Ozcan H, El-Emam R S and Amini Horri B 2023 Recent advances in high-temperature steam electrolysis with solid oxide electrolysers for green hydrogen production *Energies* **16** 3327

[202] Norman E A, Maestre V M, Ortiz A and Ortiz I 2024 Steam electrolysis for green hydrogen generation. state of the art and research perspective *Renew. Sustain. Energy Rev.* **202** 114725

[203] Qiu P, Li C, Liu B, Yan D, Li J and Jia L 2023 Materials of solid oxide electrolysis cells for H_2O and CO_2 electrolysis: a review *J. Adv. Ceram.* **12** 1463–510

[204] Kang S, Pan Z, Guo J, Zhou Y, Wang J, Fan L, Zheng C, Cha S W and Zhong Z 2024 Scientometric analysis of research trends on solid oxide electrolysis cells for green hydrogen and syngas production *Front. Energy* accepted (https://doi.org/10.1007/s11708-024-0945-5)

[205] Tarasova N, Hanif M B, Janjua N K, Anwar S, Motola M and Medvedev D 2024 Fluorine-insertion in solid oxide materials for improving their ionic transport and stability. A brief review *Int. J. Hydrog. Energy* **50** 104–23

[206] Clark D *et al* 2022 Single-step hydrogen production from NH_3, CH_4, and biogas in stacked proton ceramic reactors *Science* **376** 390–3

[207] Li F, Tong G, Duan G, Li C, Wang Z, Kawi S, Liu S and Tan X 2024 Construction of micro-tubular proton-conducting ceramic electrochemical reactor (MT-PCER) for ammonia production at atmospheric pressure *Int. J. Hydrog. Energy* **68** 1302–11

[208] Chen Y, Liu M, Shi Y and Cai N 2019 Methane production and electricity generation in a proton conducting tubular reversible solid oxide cell *ECS Trans.* **91** 2641–51

[209] Li F, Tong G, Li Y, Wang Z and Tan X 2024 Cathode tailoring of micro-tubular protonic ceramic electrochemical reactors for CO_2 hydrogenation *Sep. Purif. Technol.* **344** 127197

[210] Miao X, Feng J, Dai Z, Zhu X, Wen J, Zhang L, Ye X, Zhou Y and Wen Z 2024 A regenerative coking-resistant CO_2 hydrogenation reactor using a protonic ceramic electrolysis cell with thin and robust fuel electrode *Adv. Energy Mater.* **14** 2402208

[211] Skodra A and Stoukides M 2009 Electrocatalytic synthesis of ammonia from steam and nitrogen at atmospheric pressure *Solid State Ion* **180** 1332–6

[212] Kosaka F, Nakamura T and Otomo J 2017 Electrochemical ammonia synthesis using mixed protonic-electronic conducting cathodes with exsolved Ru-nanoparticles in proton conducting electrolysis Cells *J. Electrochem. Soc.* **164** F1323–30

[213] Guo Y, Liu B, Yang Q, Chen C, Wang W and Ma G 2009 Preparation via microemulsion method and proton conduction at intermediate-temperature of $BaCe_{1-x}Y_xO_{3-\alpha}$ *Electrochem. Commun.* **11** 153–6

[214] Wang W B, Cao X B, Gao W J, Zhang F, Wang H T and Ma G L 2010 Ammonia synthesis at atmospheric pressure using a reactor with thin solid electrolyte $BaCe_{0.85}Y_{0.15}O_{3-\alpha}$ membrane *J. Membr. Sci* **360** 397–403

[215] Chen X *et al* 2024 Synergistic bulk and surface engineering for expeditious and durable reversible protonic ceramic electrochemical cells air electrode *Adv. Mater.* **36** 2403998

[216] Danilov N, Lyagaeva J, Vdovin G and Medvedev D 2019 Multifactor performance analysis of reversible solid oxide cells based on proton-conducting electrolytes *Appl. Energy* **237** 924–34

[217] Pei K *et al* 2022 Surface restructuring of a perovskite-type air electrode for reversible protonic ceramic electrochemical cells *Nat. Commun.* **13** 2207

[218] Liu Z *et al* 2022 High-entropy perovskite oxide: a new opportunity for developing highly active and durable air electrode for reversible protonic ceramic electrochemical cells *Nano-Micro. Lett.* **14** 217

[219] Niu Y *et al* 2022 Highly active and durable air electrodes for reversible protonic ceramic electrochemical cells enabled by an efficient bifunctional catalyst *Adv. Energy Mater.* **12** 2103783

[220] Wang Y *et al* 2024 Self-recoverable symmetric protonic ceramic fuel cell with smart reversible exsolution/dissolution electrode *Adv. Funct. Mater.* accepted (https://doi.org/10.1002/adfm.202404846)

[221] Tarutin A, Lyagaeva J, Farlenkov A, Plaksin S, Vdovin G, Demin A and Medvedev D 2018 A reversible protonic ceramic cell with symmetrically designed $Pr_2NiO_{4+\delta}$-based electrodes: fabrication and electrochemical features *Materials* **12** 118

[222] Tian Y, Abhishek N, Yang C, Yang R, Choi S, Chi B, Pu J, Ling Y, Irvine J T S and Kim G 2022 Progress and potential for symmetrical solid oxide electrolysis cells *Matter* **5** 482–514

[223] Gu J, Zhang X, Zhao Y, Alodhayb A, Sun Y and Bu Y 2023 Advances and challenges in symmetrical solid oxide electrolysis cells: materials development and resource utilization Mater *Chem. Front.* **7** 3904–21

[224] Catalán-Martínez D, Navarrete L, Tarach M, Santos-Blasco J, Vøllestad E, Norby T, Budd M I, Veenstra P and Serra J M 2022 Thermo-fluid dynamics modelling of steam electrolysis in fully-assembled tubular high-temperature proton-conducting cells *Int. J. Hydrog. Energy* **47** 27787–99

[225] Li Z, Guo M, Wang C, Bello I T, Yu N, Chen X, Han M, Yu J and Ni M 2024 Thermo-chemo-mechanical analysis of protonic ceramic electrolysis cell: a statistically-designed numerical study *Int. J. Hydrog. Energy* **61** 173–87

[226] Taghikhani K, Dubois A, Berger J, Ricote S, Zhu H and Kee R 2021 Modeling electro-chemo-mechanical behaviors within the dense $BaZr_{0.8}Y_{0.2}O_{3-\delta}$ protonic-ceramic membrane in a long tubular electrochemical cell *Membranes* **11** 378

[227] Li Z, He Q, Wang C, Xu Q, Guo M, Bello I T and Ni M 2022 Ethylene and power cogeneration from proton ceramic fuel cells (PCFC): a thermo-electrochemical modelling study *J. Power Sources* **536** 231503

[228] Schwabe F, Schwarze L, Partmann C, Lippmann W and Hurtado A 2019 Concept, design, and energy analysis of an integrated power-to-methanol process utilizing a tubular proton-conducting solid oxide electrolysis cell *Int. J. Hydrog. Energy* **44** 12566–75

[229] Fogel S, Unger S and Hampel U 2024 Dynamic system modeling and simulation of a power-to-methanol process based on proton-conducting tubular solid oxide cells *Energy Convers. Manage.* **300** 117970

[230] Loureiro F J A, Nasani N, Reddy G S, Munirathnam N R and Fagg D P 2019 A review on sintering technology of proton conducting $BaCeO_3$-$BaZrO_3$ perovskite oxide materials for protonic ceramic fuel cells *J. Power Sources* **438** 226991

[231] Li J, Wang C, Wang X and Bi L 2020 Sintering aids for proton-conducting oxides—A double-edged sword? A mini review *Electrochem. Commun.* **112** 106672

[232] Medvedev D A, Murashkina A A and Demin A K 2015 Formation of dense electrolytes based on $BaCeO_3$ and $BaZrO_3$ for application in solid oxide fuel cells: the role of solid-state reactive sintering *Rev. J. Chem.* **5** 193–214

[233] Guo H, Li Y, Jiang L, Sha Y, Guo S and Han D 2024 Transport properties of the Ba(Zr,Ce,Y,Yb)$O_{3-\delta}$ proton conductor: the real role of co-substitution of Y and Yb *J. Mater. Chem.* A **12** 5875–84

[234] Li Y, Guo S and Han D 2023 Doping strategies towards acceptor-doped barium zirconate compatible with nickel oxide anode substrate subjected to high temperature co-sintering *Int. J. Hydrog. Energy* **48** 16875–84

[235] Tariq U *et al* 2024 Bridging the gap between fundamentals and efficient devices: advances in proton-conducting oxides for low-temperature solid oxide fuel cells *J. Power Sources* **613** 234910